(12) INTERNATIONAL APPLICATION PUBLISHED UNDER THE PATENT COOPERATION TREATY (PCT)

(19) World Intellectual Property Organization
International Bureau

(43) International Publication Date
02 August 2024 (02.08.2024)

WIPO | PCT

(10) International Publication Number
WO 2024/157001 A1

(51) International Patent Classification:
*A61B 5/31* (2021.01) *A61B 5/00* (2006.01)
*A61B 5/37* (2021.01) *A61N 1/36* (2006.01)
*A61B 5/374* (2021.01)

(21) International Application Number:
PCT/GB2024/050182

(22) International Filing Date:
24 January 2024 (24.01.2024)

(25) Filing Language: English

(26) Publication Language: English

(30) Priority Data:
2301045.7 25 January 2023 (25.01.2023) GB

(71) Applicants: **OXFORD UNIVERSITY INNOVATION LIMITED** [GB/GB]; Buxton Court, 3 West Way, Oxford OX2 0JB (GB). **UNIVERSITÄT BERN** [CH/CH]; Verwaltungsdirektion, Hochschulstr. 6, 3012 Bern (CH).

(72) Inventors: **DUCHET, Benoit**; University of Oxford, MRC Brain Network Dynamics Unit, Mansfield Road, Oxford OX1 3TH (GB). **BOGACZ, Rafal**; University of Oxford, MRC Brain Network Dynamics Unit, Mansfield Road, Oxford OX1 3TH (GB). **TINKHAUSER, Gerd**; Universität Bern, Universitätsklinik für Neurologie, Inselspital, Freiburgstrasse (Rosenbühlgasse 25), 3010 Bern (CH). **AVERNA, Alberto**; Universität Bern, Universitätsklinik für Neurologie, Inselspital, Freiburgstrasse (Rosenbühlgasse 25), 3010 Bern (CH). **NILCHIAN, Parsa**; University of Oxford, MRC Brain Network Dynamics Unit, Mansfield Road, Oxford OX1 3TH (GB).

(74) Agent: **J A KEMP LLP**; 80 Turnmill Street, London Greater London EC1M 5QU (GB).

(81) Designated States *(unless otherwise indicated, for every kind of national protection available)*: AE, AG, AL, AM, AO, AT, AU, AZ, BA, BB, BG, BH, BN, BR, BW, BY, BZ, CA, CH, CL, CN, CO, CR, CU, CV, CZ, DE, DJ, DK, DM, DO, DZ, EC, EE, EG, ES, FI, GB, GD, GE, GH, GM, GT, HN, HR, HU, ID, IL, IN, IQ, IR, IS, IT, JM, JO, JP, KE, KG, KH, KN, KP, KR, KW, KZ, LA, LC, LK, LR, LS, LU, LY, MA, MD, MG, MK, MN, MU, MW, MX, MY, MZ, NA, NG, NI, NO, NZ, OM, PA, PE, PG, PH, PL, PT, QA, RO, RS, RU, RW, SA, SC, SD, SE, SG, SK, SL, ST, SV, SY, TH, TJ, TM, TN, TR, TT, TZ, UA, UG, US, UZ, VC, VN, WS, ZA, ZM, ZW.

(84) Designated States *(unless otherwise indicated, for every kind of regional protection available)*: ARIPO (BW, CV, GH, GM, KE, LR, LS, MW, MZ, NA, RW, SC, SD, SL, ST, SZ, TZ, UG, ZM, ZW), Eurasian (AM, AZ, BY, KG, KZ,

(54) Title: NEURAL SOURCE LOCALISATION FOR OPTIMISATION OF DEEP BRAIN STIMULATION

(57) Abstract: There is provided a method for determining a location of a source of neural activity signals within a brain. The method comprises measuring electrical signals from respective contacts of a plurality of contacts located at known relative positions within the brain, processing the electrical signals to detect neural activity signals in the electrical signals from the respective contacts, determining timings of the detected neural activity signals, and determining the location of the source of neural activity within the brain relative to the plurality of contacts by fitting a source model to the timings relative to each other, wherein the source model models an arrangement of the source of the neural activity signals and models the neural activity signals as travelling waves that propagate through the brain. The location of the source of neural activity can be used to guide optimal delivery of deep brain stimulation.

Fig. 3

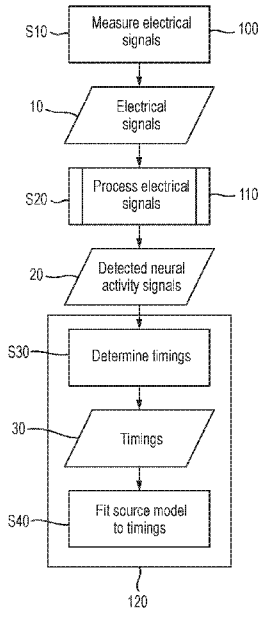


WO 2024/157001 A1

[Continued on next page]

RU, TJ, TM), European (AL, AT, BE, BG, CH, CY, CZ, DE, DK, EE, ES, FI, FR, GB, GR, HR, HU, IE, IS, IT, LT, LU, LV, MC, ME, MK, MT, NL, NO, PL, PT, RO, RS, SE, SI, SK, SM, TR), OAPI (BF, BJ, CF, CG, CI, CM, GA, GN, GQ, GW, KM, ML, MR, NE, SN, TD, TG).

**Published:**

— *with international search report (Art. 21(3))*

# NEURAL SOURCE LOCALISATION FOR OPTIMISATION OF DEEP BRAIN STIMULATION

The invention relates to methods for optimising the efficacy of deep brain stimulation, in particular by localising a source of neural activity within a brain.

Deep brain stimulation (DBS) is a neurosurgical treatment option for various neurological disorders, most commonly for movement disorders such as Parkinson's disease (PD), if symptoms cannot be controlled with oral medication only. For this indication, DBS leads are implanted in both brain hemispheres in the subthalamic nucleus (STN, shown in Fig. 1) or globus pallidus internus (GPI), where the delivery of electrical current can relieve the symptoms. Such DBS leads consists of a minimum of 4 contacts, but nowadays most commonly of 8 contacts (i.e. multi contact DBS lead). Neurophysiological recordings through these DBS electrodes revealed pathologically elevated activity in the beta frequency range (13-35 Hz) in PD. This elevated $\beta$-activity (13-35 Hz) is correlated with the severity of motor symptoms, particularly bradykinesia and rigidity. The exact mechanisms of action of DBS are still debated. However, high-frequency DBS of the STN or GPI is associated with the suppression of elevated $\beta$-oscillations and the degree of suppression correlates with the improvement in motor symptoms. According to this line of argument, abnormal synchronization of $\beta$-activity is suggested to promote the current motor state, hereby locking it in a physical condition that resists changes. Hence, suppressing $\beta$-activity with DBS may "unlock" the effector.

DBS, in its current clinical application requires further optimisation. For every single patient physicians select and tune the stimulation parameters, such as amplitude, frequency, and stimulation contact, on a trial-and-error basis. This screening procedure for the optimal stimulation setting is very time consuming. Moreover, the clinical effect of the stimulation setting may not immediately be optimal, or stimulation-induced side effects such as speech problems, impaired balance, involuntary movements, or neuropsychiatric side effects may occur. Consequently, the manual tuning procedure to determine the optimal stimulation setting often needs to be repeated. Thus automatized or assisting tools are required to optimise DBS programming in clinical practice. Such programming tools could be based on neurophysiological recordings from the regions where the electrode is implanted.

Although the timing and strength of DBS can be optimized, the spatial delivery of

STN stimulation is understudied, and further work is needed to improve spatial delivery of STN stimulation.

According to a first aspect, there is provided a method for determining a location of a source of neural activity signals within a brain, the method comprising: measuring electrical signals from respective contacts of a plurality of contacts located at known relative positions within the brain; processing the electrical signals to detect neural activity signals in the electrical signals from the respective contacts; determining timings of the detected neural activity signals; and determining the location of the source of neural activity within the brain relative to the plurality of contacts by fitting a source model to the timings relative to each other, wherein the source model models an arrangement of the source of the neural activity signals and models the neural activity signals as travelling waves that propagate through the brain.

Travelling waves are spatially propagating oscillations that have been observed in cortical and subcortical areas at different frequencies. The inventors have theorised that neural activity signals (such as beta-oscillations in the STN) propagate as a traveling wave. Using this model, it becomes possible to identify the location of sources of neural activity signals, which can then be used to guide contact selection in DBS. This helps to improve intraoperative DBS targeting and postoperative stimulation contact selection, thereby improving the efficacy of treatment and reducing side effects.

In some embodiments, the processing of the electrical signals comprises, for each of the respective contacts, determining a peak frequency for the contact as the frequency having the highest power within a predetermined frequency range. This can be used to identify the type of neural activity signal that is measured by the contact.

In some embodiments, the peak frequency is determined using a net power spectral density calculated by subtracting a background power spectral density from a power spectral density of the electrical signals from the contact. Optionally, the background power spectral density comprises an estimated power spectral density of aperiodic noise. This ensures that the method takes account of the power due to signals of interest and physiological origin, and not merely noise signals.

In some embodiments, the predetermined frequency range is a range of beta brain wave frequencies, optionally 13-35 Hz. These frequencies are of particular interest for DBS to treat conditions such as PD as discussed above.

In some embodiments, the processing of the electrical signals comprises filtering the electrical signals from the respective contacts to detect the neural activity signals, optionally using a frequency bandpass filter. This ensures that only signals of interest and of the desired physiological origin contribute to determining the location, making the location determination more specific to the source that is producing the neural activity signals of interest.

In some embodiments, the processing of the electrical signals comprises determining a hemisphere peak frequency as an average, optionally a median, of the peak frequencies of contacts within the same hemisphere of the brain, and the frequency bandpass filter is centred on the hemisphere peak frequency. This ensures uniformity between the processing of contacts in the same hemisphere of the brain so that consistency and reliability of the location determination can be improved.

In some embodiments, the hemisphere peak frequency is determined as an average of the peak frequencies of contacts within the same hemisphere of the brain for which a power at the peak frequency of the contact is above a predetermined power threshold. This ensures that only signals from contacts where significant power in the range of interest is received contribute to setting the filtering parameters.

In some embodiments, the frequency bandpass filter is configured to pass frequencies within a predetermined frequency range, optionally wherein the predetermined frequency range is a range of beta brain wave frequencies, further optionally 13-35 Hz. It is possible that no peak having a specific shape or characteristics is present in the electrical signals, even where neural activity signals of interest are nonetheless present. In these situations it may be preferable to pass frequencies in a predetermined range rather than set the range based on identifying a peak frequency.

In some embodiments, the timings are determined for a subset of the detected neural activity signals, the subset comprising neural activity signals detected at contacts for which a power at the peak frequency of the contact is above a predetermined power threshold. This means that the method only fits the location using signals from contacts where significant power in the range of interest is received, improving the accuracy of the location determination.

In some embodiments, the timings are determined for a subset of the detected neural activity signals, the subset comprising neural activity signals detected at contacts for

which an average of a statistical dependency metric between the neural activity signal for the contact and the neural activity signals for each of the other contacts is above a predetermined correlation threshold. This establishes a minimum level of statistical dependence between signals for the signals to be taken into account when determining the location. It also prevents contacts from contributing that were not exposed to the neural activity field due to their position, orientation (e.g. if they are facing away from source), or because other parts of the lead shielded them from the neural activity field. This improves the likelihood that the signals from different contacts that are used to determine location are actually different versions of the same original signal.

In some embodiments, the timing between a first detected neural activity signal from a first contact of the plurality of contacts and a second detected neural activity signal from a second contact of the plurality of contacts is a relative timing that, when applied to the first detected neural activity signal, maximises a statistical dependency metric between the first detected neural activity signal and the second detected neural activity signal. Using a measure of statistical dependency is a convenient way to quantitatively evaluate the similarity of signals and thereby estimate the time delay assuming that the signals originate from the same source. The statistical dependency metric may be a temporal cross-correlation, a coherence, or a mutual information between the neural activity signal first detected neural activity signal and the second detected neural activity signal.

In some embodiments, the determining of the timings comprises calculating, for each of the respective contacts, a burst signal representing timings of periods in which an amplitude of the detected neural activity signal from the contact is above a predetermined amplitude threshold; and the timing between the detected neural signal from the first contact and the detected neural signal from the second contact is a relative timing that, when applied to a first burst signal calculated for the first contact, maximises a statistical dependency metric between the first burst signal and a second burst signal calculated for the second contact. Using burst signals provides a more easily identifiable beginning and end to periods of activity and simplifies the computational complexity of determining the dependency metric.

In some embodiments, the determining of the timings comprises identifying, for each of the respective contacts, one or more burst periods in which an amplitude of the detected neural activity signal from the contact is above a predetermined amplitude

threshold for at least a predetermined duration; the timing between a first detected neural activity signal from a first contact of the plurality of contacts and a second detected neural activity signal from a second contact of the plurality of contacts is the relative timing between a first burst period for the first contact and a second burst period for the second contact, the second burst period being a burst period that begins closest in time to the beginning of the first burst period, optionally wherein the second burst period is a burst period that begins within a predetermined time window around the beginning of the first burst period. This process of more explicitly matching bursts between neural activity signals can be advantageous in situations where calculating the statistical dependency metric between the signals is difficult or unreliable.

In some embodiments, a plurality of burst periods are identified for each of the respective contacts; a plurality of relative timings are determined based on a corresponding plurality of first burst signals and second burst signals; and the timing between the first detected neural activity signal and the second detected neural activity signal is an average of the plurality of relative timings. Averaging the obtained relative timings over many matched bursts leads to more robust results than using a single pair of matched bursts.

In some embodiments, the location of the source is a parameter of the source model, and determining the location of the source by fitting the source model to the timings relative to each other comprises fitting the location. Fitting the location allows it to be optimised using various well-understood and computationally efficient methods to best fit the data.

In some embodiments, the source model models the arrangement of the source as a point source, and determining the location of the source comprises determining a location of the point source. This is a simple model of the nature of the source that may be appropriate for particular types of neural activity signal in certain regions of the brain.

In some embodiments, the location of the point source is a three-dimensional location relative to the plurality of contacts. This allows the localisation of the source relative to the contacts to permit directed stimulation.

In some embodiments, the source model assumes activity signals from the point source are emitted as spherical waves. This is a simple assumption that allows the location of the source to be approximated without requiring complex modelling of brain tissue.

In some embodiments, the source model models the arrangement of the source as a

plurality of point sources, optionally two point sources, and determining the location of the source comprises determining a location of each of the plurality of point sources. This model provides a simple way to account for the more general possibility of the source emitting over an extended area, which may be appropriate in some situations.

In some embodiments, the location of each of the point sources is a three-dimensional location relative to the plurality of contacts. This allows the localisation of the point sources relative to the contacts to permit directed stimulation.

In some embodiments, the source model assumes neural activity signals from each of the plurality of point sources have equal amplitude and/or equal phase and/or equal frequency. In some embodiments, the source model assumes neural activity signals from each of the plurality of point sources are emitted as spherical waves. These assumptions simplify the computational complexity of the fitting.

In some embodiments, the source model models the arrangement of the source as a planar source, and determining the location of the source comprises determining a location of the planar source and an orientation of the planar source. This model provides an alternative way to account for the more general possibility of the source emitting over an extended area, which may be appropriate in some situations.

In some embodiments, the location of the planar source comprises a three-dimensional location relative to the plurality of contacts and the orientation of the planar source comprises a three-dimensional vector normal to the planar source. This allows the localisation of the planar sources relative to the contacts to permit directed stimulation.

In some embodiments, a speed of the travelling waves is a parameter of the source model, and determining the location of the source by fitting the source model to the timings comprises fitting the speed of the travelling waves. This can be used to verify that the speed used by the model is physiologically plausible.

In some embodiments, the electrical signals are time-resolved measurements of local field potentials. These are electrical signals that can be measured by the contacts of typical DBS leads.

In some embodiments, one or more of the plurality of contacts are within the subthalamic (STN) nucleus or the globus pallidus internus (GPI) of the brain. This allows the method to be used to improve the treatment of conditions such as PD where the STN and GPI are common surgical targets.

In some embodiments, the plurality of contacts are located on the same deep-brain stimulation lead. This allows the relative positions of the contacts to be determined accurately based on the design of the lead, thereby improving the accuracy of the determination of the location of the source.

In some embodiments, the plurality of contacts comprises at least four contacts, optionally at least eight contacts. Using a larger number of contacts provides more information about the relative timings to improve the accuracy of the determination of the source location.

In some embodiments, the neural activity signals are beta brain waves. These brain waves are of particular interest for conditions such as PD that can be treated using DBS.

In some embodiments, the neural activity signals have a duration of at least 5 seconds, optionally 10 seconds, optionally at least 30 seconds, optionally at least one minute. Using a larger quantity of data over a longer time period can improve the accuracy of the resulting averages.

In some embodiments, the neural activity signals have a duration of at most 10 seconds, optionally at most 30 seconds, optionally at most one minute, optionally at most 5 minutes. In some implementations, it has been found that shorter duration signals provide more robust results.

According to a second aspect of the invention, there is provided a computer program comprising or a computer-readable medium having stored thereon instructions which, when carried out by a computer, cause the computer to carry out the method of the first aspect.

According to a third aspect of the invention, there is provided a method for selecting contacts of a deep-brain stimulation lead within a brain for use in deep-brain stimulation comprising: determining a location of a source of neural activity signals within the brain according to the method of the first aspect; and selecting one or more contacts of the deep-brain stimulation lead based on the location. This method allows for the optimal contact or combination of contacts to be chosen based on the relative position or orientation of the contacts to the source of neural activity signals. This can improve suppression of symptoms and reduce side effects by ensuring stimulation energy is more effectively targeted.

In some embodiments, the method of the third aspect further comprises determining

a stimulation energy for application at each of the one or more selected contacts based on the location. As well as which contact or combination of contacts to use, it may be advantageous to vary the energy applied to each contact based on its location relative to the source of neural activity.

In some embodiments, the method of the third aspect further comprises repeating the steps of determining the location, selecting one or more contacts, and, if performed, determining the stimulation energy in response to a predetermined condition being met, optionally wherein the predetermined condition is the elapsing of a predetermined length of time. This allows stimulation to be adapted to reflect changes in the position or shape of the source of neural activity signals. These changes could, for example, be driven by plastic changes due to chronic stimulation, disease progression, changes in medication, or lead movement. Patients with PD and DBS devices often require frequent adjustment of the stimulation parameters. This embodiment allows these adjustments to be automated, providing more effective stimulation over time with reduced intervention from medical professionals.

According to a fourth aspect of the invention, there is provided an apparatus for determining a location of a source of neural activity signals within a brain comprising: a measurement unit configured to measure electrical signals from respective contacts of a plurality of contacts located at known relative positions within the brain; a processing unit configured to process the electrical signals to detect neural activity signals in the electrical signals from the respective contacts; and a determining unit configured to: determine timings of the detected neural activity signals; and determine the location of the source of neural activity within the brain relative to the plurality of contacts by fitting a source model to the timings, wherein the source model models an arrangement of the source of the neural activity signals and models the neural activity signals as travelling waves that propagate through the brain.

Embodiments of the present invention will now be described by way of non-limitative example with reference to the accompanying drawings, in which:

Fig. 1 shows the subthalamic nucleus and its regions within the brain;

Fig. 2 shows a multi-contact DBS lead;

Fig. 3 is a flowchart of the present method for determining a location of a source of neural activity signals within a brain;

Fig. 4 shows further detail of the step of processing the electrical signals;

Fig. 5 illustrates peak frequency detection for a DBS contact;

Fig. 6 illustrates filtering of electrical signals and extraction of a burst signal;

Fig. 7 shows cross-correlation matrices used to extract lags between signals from different contacts;

Fig. 8 illustrates different travelling wave models for the source of neural activity signals, and shows the relative timings of signals at the plural contacts expected with a planar source model;

Fig. 9 is a flowchart of a method of selecting deep brain stimulation contacts using the location of the source of neural activity signals;

Fig. 10 shows cross-correlation matrices between different contacts for different hemispheres;

Fig. 11 shows lag matrices between different contacts for different hemispheres;

Fig. 12 shows a fit of a single point source model to observed lag matrices;

Fig. 13 shows lag matrices fitted using the single point source model;

Fig. 14 shows a shuffling analysis for the single point source model used to control for overfitting;

Fig. 15 shows a predicted source position for a representative hemisphere in the single point source model;

Fig. 16 shows predicted source positions for multiple hemispheres of different patients in the single point source model;

Fig. 17 shows reconstruction performance of the single point source model across frequencies;

Fig. 18 shows the distribution of predicted wave speeds in the single point source model;

Fig. 19 shows a fit of a two point source model to observed lag matrices;

Fig. 20 shows lag matrices fitted to the two point source model;

Fig. 21 shows a shuffling analysis for the two point source model used to control for overfitting;

Fig. 22 shows a predicted source position for a representative hemisphere in the two point source model;

Fig. 23 shows variability in the distance between sources in the two-point source

model;

Fig. 24 shows predicted source positions for multiple hemispheres of different patients in the two point source model;

Fig. 25 shows reconstruction performance of the two point source model across frequencies;

Fig. 26 illustrates how the two-point source model requires a minimum speed limit for travelling waves;

Fig. 27 shows the distribution of predicted wave speeds in the two point source model;

Fig. 28 shows a fit of a planar source model to observed lag matrices;

Fig. 29 shows lag matrices fitted to the planar source model; and

Fig. 30 shows predicted source positions in the planar source model.

Fig. 31 shows the distribution of predicted wave speeds in the planar source model;

Fig. 32 shows the cost landscape of source position in the single point source model for two hemispheres;

Fig. 33 shows the average cost landscape of source position in the single point source model;

The development of multi-contact directional DBS leads facilitates site-specific local field potential (LFP) recording and current delivery. Fig. 2 shows an example of the VerciseTM Cartesia Directional Leads (Boston Scientific), which has eight contacts 6 distributed over four levels on a single lead 4. These multi-contact DBS leads enable directional LFP recordings and spatially-targeted stimulation.

Early evidence suggests that understanding the characteristics of LFP recorded with multi-contact leads can help guide DBS programming. Tinkhauser et al. 2018 showed that stimulation by the contact with the highest average $\beta$-power at rest leads to the best clinical outcomes. Likewise, Shah et al. 2022 highlighted that contact-specific spectral LFP features (i.e., $\beta$-power at rest and gamma activity during movement) predict which stimulation site will most efficiently improve PD symptoms. Others have also attempted to use contact-specific LFP signatures to identify patient-specific locations of highest beta synchrony in the STN, thus recommending stimulation toward the center of beta synchronization (Maling et al. 2018; Tamir et al. 2020). However, the empirical post-operative programming of DBS leads still poses a challenge in clinical practice.

While the leads shown in Fig. 2 have eight contacts per DBS lead, new lead design with a higher number of contacts are currently studied.

Since the manual and detailed programming of the systems in use and of those in development is unfeasible, automated algorithms will be needed to tune the stimulation parameters for selecting the sites of stimulation. Even in DBS leads with only a few contacts, algorithmic selection of stimulation sites would also be helpful for clinical routine. Physicians currently tune contact selection parameters manually based on a trial-and-error approach until patient symptoms are suppressed efficiently. This is highly time-consuming and while the selected parameters may be satisfactory, they may not be optimal. Automated contact selection would aid physicians in providing stimulation that maximizes clinical outcomes for patients.

While there has been some investigation of contact selection using LFP features, the spatial dynamics of $\beta$-activity in the STN remain unexplored. Understanding how $\beta$-activity spreads in the STN can enhance DBS treatment along the spatial dimension.

In contrast to location-invariant rhythmic activity, some neural oscillations are traveling waves, propagating through the brain at a constant speed. Traveling neural oscillations have been hypothesized to facilitate information transfer among distinct brain structures. The idea of cortical and subcortical traveling waves has recently gained traction due to the rise of simultaneous multichannel microelectrode arrays that facilitate concurrent LFP recordings over spatially separated brain areas.

Traveling waves have been detected in monkeys, humans, and rodents in cortical and subcortical areas. In the motor cortex, anatomically hardwired circuits carry $\beta$-waves between populations of neurons during motor preparation and execution. Furthermore, in the hippocampus, theta waves travel along the septotemporal axis (Zhang and Jacobs 2015). Moreover, $\beta$-waves in frontal and parietal regions have been recently linked to the maintenance and use of reward memories. Lastly, neural oscillations with distinct frequencies are believed to travel across the cortex in distinct directions at unique timescales, thus providing a mechanism for the processing of separate cognitive functions (Mohan, Zhang, and Jacobs 2022). Interestingly, a variety of wave types have been identified to date, including spherical, planar, and rotating waves (Bhattacharya et al. 2022). This suggests that the brain contains a rich and diverse repertoire of spatially spreading oscillations.

The present invention makes use of multi-contact leads to allow local LFP signals to be used to identify the location of a source of neural activity signals to enable optimisation of stimulation sites. The present inventors have realised that the spatial dynamics of neural activity signals such as $\beta$-oscillations in the STN can be characterised by modelling the neural activity signals as traveling waves originating from a source. For example, STN $\beta$-activity can be modelled as a traveling wave originating from the motor STN. Determining the source and velocity of such oscillations can facilitate their silencing with DBS. Identifying the source of traveling $\beta$-waves can aid physicians in selecting the ideal stimulation site (i.e. stimulation contact or combination of stimulation contacts) in multi-contact DBS systems. By targeting stimulation towards source locations, $\beta$-oscillations may be suppressed more efficiently, thus improving DBS outcomes for patients. In addition to contact selection, the invention allows the quantification of the propagation characteristics (shape, source, and speed) of neural activity signals. Understanding signal characteristics can give insight into the neuropathophysiology of neurological disease. In addition, understanding signal characteristics would help to refine spatial parameters beyond current approaches. For example, the size and shape of electric fields applied during DBS could be modified to reflect the neural activity signal properties. Different stimulation could be designed to suppress different travelling wave types such as a spherical traveling wave or planar waves.

Automating contact selection can also be a preventative measure. Usually, DBS patients undergo regular check-ups (i.e., every three to six months), during which physicians readjust the stimulation parameters. Due to the progressive nature of PD, it is possible that the location of pathological neural activity may change. Sources could expand, shift, or additional new source locations could emerge. Similar source dynamics have already been observed for the starting points of epileptic seizures (Diamond et al. 2021). Automated source localization enables the continuous tuning of stimulation sites (on a timescale of hours or days) between check-up periods. Alternatively, such systems could generate early alerts to inform patients and medical teams when readjustments to the spatial parameters of stimulation are needed.

Fig. 3 shows the steps of a method for determining a location of a source of neural activity signals within a brain.

The method comprises measuring S10 electrical signals 10 from respective contacts

6 of a plurality of contacts located at known relative positions within the brain 2. The known relative positions are positions of the contacts relative to one another, and not necessarily relative to any particular anatomical structure such as the skull, a region of the brain etc. An advantage of the present method is that it can be applied without requiring complex or involved localisation processes such as x-ray or MRI imaging to determine an absolute location of the contacts, used to suggest the optimal stimulation site.

The plurality of contacts are preferably located on the same deep-brain stimulation lead 4. This also makes it easy to ascertain the relative positions of the contacts 6, since they are determined by the design of the lead 4. The plurality of contacts may comprise at least four contacts 6, optionally at least eight contacts 6. A greater number of contacts is preferable to provide greater spatial resolution. The electrical signals 10 are time-resolved measurements of local field potentials.

The position of the contacts 6 within the brain will depend on the condition that is to be treated using the DBS lead. The neural activity signals for which the source is to be determined will also depend on the condition to be treated using the DBS lead 4. For example, when seeking to treat Parkinson's disease, one or more of the plurality of contacts are within the subthalamic nucleus of the brain and the neural activity signals are beta brain waves. Other target structure for other applications of DBS can include the globus pallidus internus or the thalamus. Typically, one DBS lead is implanted in corresponding positions in each hemisphere of the brain.

The method comprises processing S20 the electrical signals to detect neural activity signals 20 in the electrical signals from the respective contacts 6. The detected neural activity signals 20 will not necessarily be an exact match to the neural activity signals originally produced by the source because additional contributions such as noise will be present in the detected neural activity signals 20. Nonetheless, the detected neural activity signals 20 can still be used to determine the source location. Specific sources of noise may be removed with filtering or other suitable techniques. For example, line noise is removed with a notch filter centred around 50 Hz and its harmonics.

The detected neural activity signals 20 may have a duration that is chosen to suit the details of the specific implementation of the method. In some embodiments, the neural activity signals 20 may be as long as allowed by the measured electrical signals. For example, the neural activity signals 20 may have a duration of at least 5 seconds,

optionally 10 seconds, optionally at least 30 seconds, optionally at least one minute. This may be advantageous because using a larger quantity of data over a longer time period can improve the accuracy of the resulting averages.

However, in some embodiments, it can be advantageous to limit the amount of data in each neural activity signal 20 to reduce confusion with other spurious signals or remove periods where no pathological activity occurs. In such embodiments, the neural activity signals 20 may have a duration of at most 10 seconds, optionally at most 30 seconds, optionally at most one minute, optionally at most 5 minutes.

Further detail of the processing S20 of the electrical signals 10 is shown in Fig. 4. The processing S20 of the electrical signals 10 comprises, for each of the respective contacts 6, determining S22 a peak frequency for the contact 6 as the frequency having the highest power within a predetermined frequency range. This frequency is merely a frequency of maximum power and there is no requirement that any "peak" having specific shape or characteristics actually be present in the data or be identified by, e.g. some form of peak-finding algorithm.

The predetermined frequency range will be the range of frequencies of neural activity signals that are of interest, i.e. that are expected to be produced by the source for which the location is to be determined. For example, the predetermined frequency range may be a range of beta brain wave frequencies with commonly used boundaries such as 13-35 Hz.

For each contact, power spectral densities (PSDs) are used to identify the frequency having the highest power within the predetermined frequency range. PSDs can be obtained using any suitable algorithm, for example using Welch's overlapped segment averaging estimator. The peak frequency is determined using a net power spectral density calculated by subtracting a background power spectral density from a power spectral density of the electrical signals from the contact. The background power spectral density may comprise an estimated power spectral density of aperiodic noise. The aperiodic components of the power spectra may be estimated used any suitable technique, for example using the FOOOF toolbox (Donoghue et al. 2020). Other filtering may also be applied to the net power spectral density before determining the peak frequency, for example a Gaussian or other filter.

Fig. 5 shows an example of determining the contact-specific peak frequencies for

the beta frequency range. Peak beta frequencies were obtained by subtracting the aperiodic noise (black line) from the model fit (blue line). A Gaussian filter with a standard deviation of 6 Hz was then applied to the resulting signal. Subsequently the frequency with the highest relative β-power above noise (orange line, right panel) in the $\beta$-range (13-35 Hz) was defined as a contact's peak beta frequency. The "model fit" is a smooth representation of the raw data PSD (orange line, left panel). In Fig. 5A, the PSD in the left panel displays a noticeable peak in the β-range above aperiodic noise levels. In Fig. 5B, no such peak is visible, indicating a lack of beta-frequency neural activity signal detected at this contact.

The processing S20 of the electrical signals 10 comprises filtering S26 the electrical signals 10 from the respective contacts 6 to detect the neural activity signals 10, optionally using a frequency bandpass filter. This ensures that only the relevant components of the electrical signals 10 are used for the further steps of the method.

The processing S20 of the electrical signals 10 comprises determining S24 a hemisphere peak frequency as an average, optionally a median, of the peak frequencies of contacts 6 within the same hemisphere of the brain 2. Since one DBS lead 4 is generally implanted per hemisphere, the contacts 6 within the same hemisphere of the brain will usually be all of the contacts 6 on the relevant single DBS lead 4. The frequency bandpass filter is centred on the hemisphere peak frequency. This introduces a uniform filtering for all the contacts 6 in the same region of the brain 2. The hemisphere peak frequency is determined as an average of the peak frequencies of contacts 6 within the same hemisphere of the brain for which a power at the peak frequency of the contact 6 is above a predetermined power threshold.

As mentioned above, it is not necessary that a recognisable peak having particular shape or characteristic be present in the electrical signals. Therefore, in some embodiments no specific peak frequency or hemisphere peak frequency may be identified. The frequency bandpass filter may be configured to pass frequencies within a predetermined frequency range, rather than being centred on the hemisphere peak frequency. The predetermined frequency range may be a range of neural activity signals that are of interest, for example beta brain wave frequencies (e.g. 13-35 Hz).

The method further comprises determining S30 timings 30 between the detected neural activity signals 20. Not all of the electrical signals 10 from the contacts 6 are used

to determine the timings 30. Two rejection criteria were applied to the contacts 6 according to which the detected neural activity signals 20 derived from those contacts would not be used in further steps of the method.

As shown above in relation to Fig. 5, not all contacts 6 may display any significant signal in the frequency range of interest. Such contacts 6 should not contribute to the location determination because they may reduce the accuracy of the location. Therefore, the timings 30 are determined for a subset of the detected neural activity signals 20, the subset comprising neural activity signals 20 detected at contacts 6 for which a power at the peak frequency of the contact 6 is above a predetermined power threshold. This is referred to as the first rejection criterion.

Where no specific peak frequency is expected or present, the first rejection criterion may instead be set based on a total power within the predetermined frequency range, i.e. the range of neural activity signals that are of interest. In this case, the timings 30 are determined for a subset of the detected neural activity signals 20, the subset comprising neural activity signals 20 detected at contacts 6 for which a total power in a predetermined frequency range is above a predetermined total power threshold. Alternatively where no specific peak frequency is expected or present, the first rejection criterion may be dispensed with and not applied.

The power at the peak frequency or the total power that is compared to the predetermined power threshold is preferably the power in the net power spectral density, i.e. such that the first rejection criterion applies to the power above the background noise, not the absolute power.

For the data shown in Fig. 5, the signals of interest are traveling $\beta$-waves, so contacts without measurable $\beta$-power above aperiodic noise were discarded. The power threshold in Fig. 5 was defined as a relative peak height of 0.3 in the net power spectral density. The power threshold can be determined in any suitable way. For Fig. 5, the power threshold was determined empirically upon visual inspection of a subset of 80 contacts from 10 hemispheres. The contact for which the electrical signal 10 is shown in Fig. 5A passed the rejection criterion 1 and was accepted. The contact for which the electrical signal 10 is shown in Fig. 5B was rejected.

A second rejection criterion is also applied. This aims to discard neural activity signals 20 detected at contacts 6 that were not exposed to the neural activity signals of

interest due to reason such as their position (e.g., outside the relevant region of the brain), orientation (faced away from the source), or because other parts of the leads shielded them. To this end, the timings 30 are determined for a subset of the detected neural activity signals 20, the subset comprising neural activity signals 20 detected at contacts 6 for which an average of a statistical dependency metric between the neural activity signal 20 for the contact 6 and the neural activity signals 20 for each of the other contacts 6 is above a predetermined correlation threshold. This is referred to as rejection criterion 2.

The correlation threshold may be set at any suitable level. The correlation threshold may be set relative to the average statistical dependency metric between all other contacts 6, for example 80% of the statistical dependency metric across all contacts, optionally 90%, optionally 95%. Alternatively, the correlation threshold may be set using a surrogate distribution, for example as the $80^{th}$ percentile of the surrogate distribution, optionally the $90^{th}$ percentile, optionally the $95^{th}$ percentile.

The statistical dependency metric may comprise any suitable measure. For example, the statistical dependency metric may be a temporal cross-correlation, a coherence, or a mutual information between the neural activity signal 20 for the contact 6 with the neural activity signals 20 for each of the other contacts 6. The coherence will be integrated within a predetermined frequency band of interest, for example the frequency range of neural activity signals that are of interest such as the frequency range of beta frequency brain waves, or a band (e.g. a narrow band of ± 5Hz, optionally ± 3Hz, optionally ± 1Hz) around the patient's peak beta frequency. In the examples below, the temporal cross-correlation will be used, but this only exemplary.

In general, the determined timings may be absolute timings or relative timings. However, the source model is fitted to timings relative to one another as discussed further below. Therefore, the timing 30 between a first detected neural activity signal from a first contact of the plurality of contacts and a second detected neural activity signal from a second contact of the plurality of contacts is preferably a relative timing 30 that, when applied to the first detected neural activity signal, maximises a statistical dependency metric between the first detected neural activity signal and the second detected neural activity signal. In other words, the timing 30 between two detected neural activity signals 20 is an estimate of the lag between the arrival of the same original neural activity signals from the source at the corresponding contacts 6. The method comprises determining such

relative timings 30 between each pair of detected neural activity signals 20.

The determining S30 of the timings comprises calculating, for each of the respective contacts, a burst signal representing timings of periods in which an amplitude of the detected neural activity signal 20 from the contact is above a predetermined amplitude threshold. In the context of the examples shown in the figures and discussed below, the frequency range of interest is that of beta frequency brain waves, and so the periods in which the amplitude is above the amplitude threshold are referred to a beta bursts.

The calculation of the burst signals is illustrated in Fig. 6. Firstly in step A, the electrical signals 10 (i.e. the LFPs) were bandpass filtered S26 as discussed above. The filtering used a second-order Butterworth filter centred on the hemisphere peak frequency with a width of ± 3Hz. In step B, the upper envelope of the bandpass filtered electrical signals 10 was compared to the predetermined amplitude threshold to detect the $\beta$-bursts. A contact-specific 75th percentile amplitude threshold was applied to the upper envelope to binarize the signal into the bursts (Tinkhauser, Pogosyan, Tan, et al. 2017). Finally, in step C) the burst signal is produced where periods with amplitudes above the amplitude threshold were defined as beta bursts.

The burst signals were then used for all further analyses. This means that the timing 30 between the detected neural signal from the first contact and the detected neural signal from the second contact is a relative timing 30 that, when applied to a first burst signal calculated for the first contact, maximises a statistical dependency metric between the first burst signal and a second burst signal calculated for the second contact.

In the specific example data discussed below, normalized cross-correlations were used to estimate the data lags (or delays or relative timings) between contacts' burst signals. The cross-correlation of the burst signals J and K from contacts $\boldsymbol{C_j}$ and $\boldsymbol{C_k}$ was computed as

$$\boldsymbol{R_{jk}(\tau) = (J \star K)(\tau) = \int_0^{T-\tau} \overline{J(t)}\, K(t+\tau)dt}, \tag{1}$$

where $\tau$ is the lag (sliding window), $\overline{J(t)}$ is the complex conjugate of J at time t, and T the recording duration. Cross-correlation coefficients were then normalized according to

$$\boldsymbol{\widehat{R}_{jk}(\tau) = \frac{1}{\sqrt{R_{jj}(0)R_{kk}(0)}} R_{jk}(\tau)}, \tag{2}$$

where $\hat{R}_{jk}$ denotes the normalized cross-correlation and $R_{jj}(0)$ and $R_{kk}(0)$ are the autocorrelations of signals from contacts j and k with zero lag. The data lag ($\Delta t_{jk}^{\mathrm{dat}}$) between two contacts $(C_j, C_k)$ was defined as the delay ($\tau$) that resulted in the maximum $\hat{R}_{jk}$ (Müller et al. 2003).

An example set of cross-correlation and lag data are illustrated in Fig. 7. In this example, the DBS lead comprises eight contacts, so the data are summarized in $8 \times 8$ matrices. Each entry in these matrices either described the lag or cross-correlation between two contacts. Fig. 7A shows an example of the maximization of the normalized cross-correlation between the signals of two contacts. The lag between two burst signals was the delay ($\tau$) which maximized the cross-correlation.

Fig. 7B shows the cross-correlation matrices, which are symmetrical across their diagonals, which were filled with ones. The fields with the black frame correspond to the data shown in Fig. 7A. Contacts with cross-correlations below 95% of the cross-correlation across all contacts were discarded according to the second rejection criterion (white rows in Fig. 7C and Fig. 7D). Fig. 7D shows the data lag (relative timing) matrices summarising the delays computed in A for accepted contacts. Lag matrices are antisymmetric across their diagonals, which were filled with zeros. Entries for rejected contacts (as defined by the two rejection criteria above) appear white in Fig. 7C and Fig. 7D. The colour of the black boxes is different in the lag matrix in Fig. 7D due to the sign of the delay depending on which contact is assigned to the lead signal. Freq. = hemisphere's peak beta frequency, $R_{jk}$ = max. normalized cross-correlation.

The periods in which the amplitude of the detected neural activity signal 20 from the contact is above a predetermined amplitude threshold that are identified by the burst signal may be referred to as bursts or burst periods. As an alternative to using a statistical dependency metric between the burst signals as discussed above, the lags between signals may be determined by matching specific bursts to one another between the neural activity signals.

In this case, the determining of the timings comprises identifying, for each of the respective contacts, one or more burst periods in which an amplitude of the detected neural activity signal from the contact is above a predetermined amplitude threshold for at least a predetermined duration. Introducing a minimum duration of the bursts avoids short bursts

that may be driven by noise. The predetermined duration may be, for example, 50ms, optionally 100ms, optionally 200ms. These durations are typical of the bursts that are seen in conditions of interest, such as Parkinson's disease. The burst periods correspond to individual bursts that would appear in the burst signal, as illustrated in Fig. 6.

The timing between a first detected neural activity signal from a first contact of the plurality of contacts and a second detected neural activity signal from a second contact of the plurality of contacts can then be calculated as the relative timing between a first burst period for the first contact and a second burst period for the second contact. The second burst period for the second contact is selected as being a burst period that begins closest in time to the beginning of the first burst period. This assumes that the lag or relative timing between the detection of the same burst at different contacts is likely to be shorter than the interval between subsequent burst onsets. Therefore, bursts detected at similar times on different contacts are likely to correspond to multiple detections of the same underlying original neural activity signal from the source.

The second burst period may be a burst period that begins within a predetermined time window around the beginning of the first burst period. The time window can extend both forwards and backwards in time around the beginning of the first burst period. The time window will place an upper limit on the maximum relative timing that can be detected. However, using the time window prevents spurious matching of burst periods in the first detected neural activity signal and the second detected neural activity signal that are very far apart in time and unlikely to correspond to multiple detections of the same underlying original neural activity signal from the source. The time window may have any suitable size based on typically burst durations and intervals between bursts for the condition to be treated, as well as expected maximum delays. For example, the time window may be at least 100ms, optionally at least 200ms, optionally at least 300ms, optionally at least 500ms. The time window may be centred in time around the beginning of the first burst period.

To improve the accuracy of the timings determined using this method, an average of the relative timings determined for several bursts may be used. In this case, a plurality of burst periods is identified for each of the respective contacts. A plurality of relative timings is then determined based on a corresponding plurality of first burst periods and second burst periods by matching the first and second burst periods as discussed above.

The timing between the first detected neural activity signal and the second detected neural activity signal is then determined as an average of the plurality of relative timings. The average may be calculated using the relative timings from burst periods detected in the first detected neural activity signal and the second detected neural activity signal over at least 5 seconds, optionally 10 seconds, optionally at least 30 seconds, optionally at least one minute. Longer periods may be used, for example at least 30 minutes or at least 1 hour, depending on the duration and quality of signals that are available.

The method further comprises determining S40 the location of the source of neural activity within the brain 2 relative to the plurality of contacts 6 by fitting a source model to the timings 30 relative to each other. That is, although absolute or relative timings may initially be determined from the detected neural activity signals, the model is always fitted to a set of relative timings, for example in the form of the lag matrices shown in Fig. 7D. The location of the source is a parameter of the source model, and determining S40 the location of the source by fitting the source model to the relative timings comprises fitting the location. The fitting may comprise optimising parameters of the source model. The source model may vary depending on the type of waves, the region of the brain, or other such factors.

The source model models an arrangement of the source of the neural activity signals. The coordinates of source location in the source model may identify functional groups of neurons. Three different arrangements are considered below in the context of the spatial propagation of $\beta$-activity in the STN, but other arrangements may also be used depending on factors such as the region of the brain or type of neural activity signals that are of interest. The three arrangements (forms of the source model) are illustrated in Fig. 8. These were a single point source model (Fig. 8A), a planar source model (Fig. 8C), and a plural point source model (Fig. 8D). In this example, the plural point source model assumed only two sources, but in general the number of point sources could be higher.

The source model models the neural activity signals as travelling waves that propagate through the brain. In the point source model, travelling waves are modelled as spherical waves and in the planar source model, travelling waves are modelled as planar waves. The rationale behind the invention is that travelling waves from the source of neural activity will reach contacts 6 closer to the source earlier than contacts 6 further from the source. This will be represented in the relative timings of the detected neural activity

signals from the corresponding contacts.

The plot on the right of Fig. 8B is a schematic representation of the expected lags between the burst signals of contacts 1-8 of the VerciseTM Cartesia Directional Leads (Boston Scientific) shown in Fig. 2 if the source were the plane shown in Fig. 8C. The travelling waves are assumed to have constant velocity. In the two-point source model, the travelling waves can interfere with one another. For simplicity, the centre position of each contact is assumed to be the recording location for the electrical signals 10 (blue circles). For the directional contacts (2-7), the centre positions are the centre of the contact's surface. For the omnidirectional contacts (1 & 8), the centre positions lie inside the lead. The representation on the left displays this approximation.

Each of the three models is constructed with a set of parameters that describe the source and propagation speed of the travelling waves. These are shown in Table 1. Having calculated the relative timings as described, the relative timings are compared to the expected timings derived from the source model. The fitting proceeds by optimising the parameters of the source model to match the expected timings to the calculated timings. Each model and its parameters are discussed further below. In all of the exemplary source models, a speed of the travelling waves is a parameter of the source model, and determining the location of the source by fitting the source model to the relative timings comprises fitting the speed of the travelling waves.

To perform the fitting, a random starting point was chosen for each parameter within predetermined limits. Exemplary limits for the application to beta frequency waves are given in Table 1. A cost function is defined and the parameters optimised to minimise the cost. In the results below, the cost of the model was calculated through the cost function

$$\text{Cost} = \sum_{j=2}^{8} \sum_{\substack{k=1 \\ (j,k)\in A}}^{j-1} \left(\Delta t_{jk}^{\text{mod}} - \Delta t_{jk}^{\text{dat}}\right)^2 \quad (3)$$

where $\Delta t_{jk}^{\text{mod}}$ is the relative timing predicted by the model, $\Delta t_{jk}^{\text{dat}}$ is the relative timing calculated from the detected neural activity signals, and A denotes the set of indices of accepted contact pairs. The outer sum goes to 8 in this equation because the DBS leads used in the data below each have eight contacts, but in general the outer sum should run up to the number of contacts on the DBS lead.

Any suitable optimisation process may be used, for example an interior point optimization as provided by MATLAB's fmincon algorithm (details on the optimization algorithm are provided in Byrd, Schnabel, and Shultz 1988). The parameter values for a given model were chosen that resulted in the lowest cost across N optimizations (e.g. $N = 1000$), where each optimisation began with a new random starting point within the predetermined limits.

| Model | Parameters | Sym. | Bounds |
|---|---|---|---|
| *Single point-source N=1000* | Source position on anterior-posterior plane | $X_S$ | STN A-P: 6.56 to 17.72 mm |
| | Source position on medial-lateral plane | $Y_S$ | STN M-L: -18.06 to -8.28 mm |
| | Source position on dorsal-ventral plane | $Z_S$ | STN D-V: -11.59 to -4.12 mm |
| | Beta wave speed | v | 0 to 10 mm/ms |
| *Two point-source N=10000* | Source position 1 on anterior-posterior plane | $X_{S_1}$ | STN A-P: 6.56 to 17.72 mm |
| | Source position 1 on medial-lateral plane | $Y_{S_1}$ | STN M-L: -18.06 to -8.28 mm |
| | Source position 1 on dorsal-ventral plane | $Z_{S_1}$ | STN D-V: -11.59 to -4.12 mm |
| | Source position 2 on anterior-posterior plane | $X_{S_2}$ | STN A-P: 6.56 to 17.72 mm |
| | Source position 2 on medial-lateral plane | $Y_{S_2}$ | STN M-L: -18.06 to -8.28 mm |
| | Source position 2 on dorsal-ventral plane | $Z_{S_2}$ | STN D-V: -11.59 to -4.12 mm |
| | Beta wave speed | v | 0.3 to 1 mm/ms |
| *Planar source N=1000* | Position of a point on anterior-posterior plane | $X_P$ | STN A-P: 6.56 to 17.72 mm |
| | Position of a point on medial-lateral plane | $Y_P$ | STN M-L: -18.06 to -8.28 mm |
| | Position of a point on dorsal-ventral plane | $Z_P$ | STN D-V: -11.59 to -4.12 mm |
| | Magnitude of normal vector on anterior-posterior plane | $a_1$ | $-1 \leq a \leq 1$ |
| | Magnitude of normal vector on medial-lateral plane | $a_2$ | $-1 \leq b \leq 1$ |
| | Magnitude of normal vector on dorsal-ventral plane | $a_3$ | $-1 \leq c \leq 1$ |
| | Beta wave speed | v | 0 to 10 mm/ms |

N = number of optimizations, Sym. = Symbol, STN A-P = STN anterior-posterior limits in MNI space, STN M-L = STN medial-lateral limits in MNI space, STN D-V = STN dorsal-ventral limits in MNI space.

**Table 1**

In the first model, the source model models the arrangement of the source as a point source, and determining the location of the source comprises determining a location of the point source. The location of the point source is a three-dimensional location relative to the plurality of contacts. In this case, the source of neural activity is assumed to be represented by a single point source. The source model assumes neural activity signals from the point source are emitted as spherical waves with a constant speed.

The single point source model optimizes four parameters describing the source position $\left(\boldsymbol{X}_{\boldsymbol{C}_j}, \boldsymbol{Y}_{\boldsymbol{C}_j}, \boldsymbol{Z}_{\boldsymbol{C}_j}\right)$ and wave speed ($\boldsymbol{v}$) (see Table 1). For a given source position ($\boldsymbol{S}$), the distance between $\boldsymbol{S}$ and a contact $\left(\boldsymbol{C}_j\right)$ is obtained according to

$$\| \mathbf{C_j S} \| = \sqrt{\left(X_{C_j} - X_S\right)^2 + \left(Y_{C_j} - Y_S\right)^2 + \left(Z_{C_j} - Z_S\right)^2}, \quad (4)$$

where $\| \mathbf{C_j S} \|$ describes the distance between $S$ and $C_j$, and $(X_S, Y_S, Z_S)$ the source coordinates. Subsequently, the predicted lag between two contacts $C_j$ and $C_k$ ($\Delta t_{jk}^{\text{mod}}$) is determined through

$$\Delta t_{jk}^{\text{mod}} = \frac{\| \mathbf{C_j S} \| - \| \mathbf{C_k S} \|}{v}, \quad (5)$$

where $v$ denotes the predicted speed of the traveling wave.

In the second model, the source model models the arrangement of the source as a plurality of point sources, in this case two point sources, and determining the location of the source comprises determining a location of each of the plurality of point sources. As for the single point source model, the location of each of the point sources is a three-dimensional location relative to the plurality of contacts. The source model assumes neural activity signals from each of the plurality of point sources have equal amplitude and/or equal phase and/or equal frequency. The source model also assumes neural activity signals from each of the plurality of point sources are emitted as spherical waves, similarly to the single point source model.

In the two-point source model, travelling waves are modelled as the linear combination of two spherical waves originating from two point sources $S_1$ and $S_2$. It was assumed that the frequency, and amplitude of both waves are equal and that the waves travel with the same constant speed. Furthermore, the waves were assumed to be synchronized, displaying no phase difference at their sources. In this approach, the model lags (relative timings) between two contacts $C_j$ and $C_k$ are determined through the phase differences of their recorded signals. The signal $(\Gamma_j)$ experienced by $C_j$ at time t is given by

$$\Gamma_j(t) = A_1\left(t - \frac{\| \mathbf{C_j S_1} \|}{v_1}\right) + A_2\left(t - \frac{\| \mathbf{C_j S_2} \|}{v_2}\right), \quad (6)$$

where $A_1(t)$ is the wave originating from $S_1$, measured at $S_1$ at time $t$, $A_2(t)$ the wave originating from $S_2$, measured at $S_2$ at time $t$, $v_1$ and $v_2$ the wave speeds, and $\| \mathbf{C_j S_1} \|$ and $\| \mathbf{C_j S_2} \|$ the distances between the $C_j$ and $S_1$ and $S_2$. Assuming that $A_1$ and $A_2$ can be approximated by sinusoids, Eq. 6 can be rewritten as

$$\Gamma_j(t) = a_1 \sin\left(2\pi f_1 t - 2\pi f_1 \frac{\| \mathbf{C_j S_1} \|}{v_1} + \varphi_1\right) + a_2 \sin\left(2\pi f_2 t - 2\pi f_2 \frac{\| \mathbf{C_j S_2} \|}{v_2} + \varphi_2\right), \quad (7)$$

where $a_1$ and $a_2$ are the wave amplitudes, $f_1$ and $f_2$ the beta wave frequencies, and $\varphi_1$ and $\varphi_2$ the phase shifts of the signals $A_1$ and $A_2$. By assuming that $a_1 = a_2 = a$, $f_1 = f_2 = f$, $v_1 = v_2 = v$, and $\varphi_1 = \varphi_2 = 0$ (see Table 2 for details), Eq. 7 can be simplified to

$$\boldsymbol{\Gamma_j(t) = a\sin\left(2\pi ft - 2\pi f\frac{\| \mathbf{C_jS_1} \|}{v}\right) + a\sin\left(2\pi ft - 2\pi f\frac{\| \mathbf{C_jS_2} \|}{v}\right).} \quad (8)$$

Using trigonometry, Eq. 8 can be simplified to a single sinusoid as

$$\boldsymbol{\Gamma_j(t) = b\sin\left(2\pi ft + \psi_j\right),} \quad (9)$$

where $\psi_j$ is the phase recorded by contact $C_j$ at time $t$. To calculate $\psi_j$, we define:

$$\boldsymbol{\Lambda_j = \sin\left(-2\pi f\frac{\| \mathbf{C_jS_1} \|}{v}\right) + \sin\left(-2\pi f\frac{\| \mathbf{C_jS_2} \|}{v}\right),} \quad (10)$$

and

$$\boldsymbol{\Pi_j = \cos\left(-2\pi f\frac{\| \mathbf{C_jS_1} \|}{v}\right) + \cos\left(-2\pi f\frac{\| \mathbf{C_jS_2} \|}{v}\right),} \quad (11)$$

Accordingly, the phase recorded by $C_j$ is given by

$$\boldsymbol{\psi_j = \begin{cases} \operatorname{atan}\left[\frac{\Lambda_j}{\Pi_j}\right], & \text{if } \Pi_j > 0, \\ \pi - \operatorname{atan}\left[\frac{\Lambda_j}{\Pi_j}\right], & \text{if } \Lambda_j > 0 \text{ and } \Pi_j \leq 0, , \\ -\pi - \operatorname{atan}\left[\frac{\Lambda_j}{\Pi_j}\right], & \text{otherwise.} \end{cases}} \quad (12)$$

where atan returns angles in the interval $[-\pi/2,\ \pi/2]$. Consequently, the lag between $C_j$ and $C_k$ is given by

$$\boldsymbol{\Delta t_{jk}^{\text{mod}} = \frac{1}{2\pi f}\left(\psi_j - \psi_k\right).} \quad (13)$$

The cost function shown in Eq. 5 was minimized to optimize the coordinates of the two sources $(X_{S_1}, Y_{S_1}, Z_{S_1}), (X_{S_2}, Y_{S_2}, Z_{S_2})$ and the speed of the two traveling waves $(v)$. Since the two point-source model had overall more parameters than the one point-source model (7 vs. 4), the number of optimizations may need to be higher (e.g. $N = 10000$). This value was determined empirically to ensure stable model performance.

In the third model, the source model models the arrangement of the source as a planar source, and determining the location of the source comprises determining a location of the planar source and an orientation of the planar source. The location of the planar source comprises a three-dimensional location relative to the plurality of contacts and the

orientation of the planar source comprises a three-dimensional vector normal to the planar source.

The planar model described travelling waves as originating from a neural sheet. It was assumed that the waves travel at constant speeds normal to the plane in both directions. The plane could take any orientation in space without anatomical constraints. The model had seven parameters. The position and orientation of an infinite plane ($L$) were defined with a point ($P$) on its surface and a normal vector ($\mathbf{n}$) as

$$\boldsymbol{a_1 X_P + a_2 Y_P + a_3 Z_P + a_4 = 0}, \tag{14}$$

where $\mathbf{n} = (a_1, a_2, a_3)$, $(X_P, Y_P, Z_P)$ correspond to the coordinates of $P$, and $a_4$ measures the distance between $L$ and the origin. While $\mathbf{n}$ affected $L's$ orientation in space, $P$ determined its position. The distance between a contact $C_j$ and $L$ $\left(d(C_j, L)\right)$ was determined as

$$\boldsymbol{d(C_j, L) = \frac{\left|a_1\left(X_{C_j} - X_P\right) + a_2\left(Y_{C_j} - Y_P\right) + a_3\left(Z_{C_j} - Z_P\right)\right|}{\sqrt{a_1^2 + a_2^2 + a_3^2}}}, \tag{15}$$

where $\left(X_{C_j}, Y_{C_j}, Z_{C_j}\right)$ denotes the coordinates of $C_j$. The predicted lag between two contacts $C_j$ and $C_k$ was determined according to a modified version of Eq. 4

$$\boldsymbol{\Delta t_{jk}^{\text{mod}} = \frac{d(C_j, L) - d(C_k, L)}{v}}, \tag{16}$$

where the speed of the planar traveling wave is denoted with $v$. The cost function displayed in Eq. 5 was minimized to obtain the best estimates for $(a_1, a_2, a_3)$, $(X_P, Y_P, Z_P)$, and $v$, across $N = 1000$ optimizations.

The assumptions of the three example source models discussed above are summarised in Table 2.

| Model | Assumption | Expression |
|---|---|---|
| *Single point-source* | The wave is spherical originating from a single source. | - |
| | The wave speed stays constant as the wave spreads. | $v = \text{constant}$ |
| *Two point-source* | The wave is a linear combination of two spherical waves from two sources. | - |
| | The wave speed originating from both sources is equal and constant. | $v_1 = v_2 = v$ |
| | The wave amplitude of both waves is equal and constant. | $a_1 = a_2 = a$ |
| | The waves are synchronized and do not have a phase difference at their respective sources. | $\varphi = 0$ |
| | Both waves have the same beta frequency. | $f_1 = f_2 = f$ |
| *Planar source* | The wave is planar originating from a neural sheet. | - |
| | The wave speed stays constant as the wave spreads. | $v = \text{constant}$ |
| | The plane can take any orientation in space without anatomical constraints. | $-1 \leq a_1, a_2, a_3 \leq 1$ |
| | The wave is a planar wave traveling normal to the plane in both directions. | - |

**Table 2**

The invention may be implemented as a computer program comprising or a computer-readable medium having stored thereon instructions which, when carried out by a computer, cause the computer to carry out the method of any of the preceding claims. The invention may also be embodied in an apparatus for determining a location of a source of neural activity signals within a brain. The apparatus comprises a measurement unit 100 configured to measure electrical signals from respective contacts of a plurality of contacts located at known relative positions within the brain, a processing unit 110 configured to process the electrical signals to detect neural activity signals in the electrical signals from the respective contacts, and a determining unit configured to: determine timings of the detected neural activity signals and determine the location of the source of neural activity within the brain relative to the plurality of contacts by fitting a source model to the timings. As discussed above, the source model models an arrangement of the source of the neural activity signals and models the neural activity signals as travelling waves that propagate through the brain.

Also provided are methods that make use of the location of the source of neural activity signals determined using the methods above in determining various aspects of how to perform deep-brain stimulation.

Fig. 9 shows a method for selecting contacts 6 of a deep-brain stimulation lead 4 within a brain for application of deep-brain stimulation signals. The method comprises determining S50 a location of a source of neural activity signals within the brain 2 according to the method described above.

The method further comprises selecting S60 one or more contacts 6 of the deep-

brain stimulation lead 4 based on the location. The selecting S60 may comprise selecting one or more contacts 6 to which a deep brain stimulation signal is to be applied. The contacts most suited for application of the stimulation signals are likely to be the contacts that detect the strongest electrical signals at the location of the source of neural activity signals. Alternatively or additionally, the selecting S60 may comprise selecting which contacts are to be used for sensing local field potentials in a closed-loop DBS application. This may be advantageous because, depending on the location of the contacts 6 relative to the source, different contacts 6 may provide a more accurate or lower-noise indication of the relevant neural activity signals used in the closed-loop DBS scheme.

In the embodiment shown in Fig. 9, the selecting S60 is for contacts to which a stimulation signal is to be applied, and the method further comprises determining S70 a stimulation energy for application at each of the one or more selected contacts based on the location. The appropriate energy to apply at each selected contact 6 may vary depending on factors such as their proximity and orientation relative to the source. Varying the stimulation energy can therefore improve reduction of symptoms while reducing side effects by ensuring stimulation energy is most effectively directed.

The method in Fig. 9 further comprises repeating the steps of determining S50 the location, selecting S60 one or more contacts, and determining S70 the stimulation energy in response to a predetermined condition S80 being met. This allows the stimulation schemes to be adjusted if the location of the source relative to the contacts 6 changes. This could occur due to factors such as lead movement or disease progression. The predetermined condition could be manual triggering by the subject or an attending clinician, or may be another condition such as the elapsing of a predetermined length of time.

**Results**

Multi-contact LFP recordings from 27 hemispheres of 17 PD patients (11 male, 6 female) were used to validate the application of the method to beta-activity ($\beta$-oscillations) in the parkinsonian STN. The data were originally used for a study by Shah and colleagues (Shah et al. 2022).

The lags (relative timings) between the detected neural activity signals of different contacts were determined with cross-correlations. These lags were compared to predicted delays obtained from three source models using the three example arrangements of the

source of neural activity discussed above, i.e. a spherical single point-source model (1), a spherical two point-source model (2), and a planar neural sheet source model (3), optimized to fit the observed lags.

Exemplary neurophysiological recordings from 27 hemispheres (labelled H1 to H27) of 17 PD patients implanted with DBS electrodes served to exemplify the source localisation algorithm (Cohort, Bern University Hospital). Subjects were implanted in the STN with a multi-contact DBS lead. This DBS lead has a hybrid contact geometry consisting of eight contacts (C). The bottom (C1, bullet tip) and top contacts (C8, ring) only allow for omnidirectional recording (see Fig. 2). Contact levels two (C2-4) and three (C5-7) are segmented, enabling directional recording along three directions angled at 120° from each other.

As described by recent studies (e.g. Horn et al. 2019), DBS lead localisation was reconstructed using the Lead-DBS toolbox (version 2.3.2) along with MATLAB 2019b (The MathWorks, Inc., Natick, MA). Using the Statistical Parametric Mapping 12 (SPM12) software and Advanced Normalization Tools (Avants et al. 2014), preoperative MRI images and postoperative CT images were co-registered and normalized into the Montreal Neurological Institute (MNI) space (MNI 152 NLIN 2009b). To account for error-introducing movements of the brain during lead implantation, coarse and fine masks were used to perform a brainshift correction (Schönecker et al. 2009; Horn et al. 2019). Co-registrations and normalizations were checked manually prior to further processing. Electrode positions and trajectories were reconstructed with semi-automatic PaCER processing and manual corrections (Husch et al. 2018). The DiODe algorithm (Hellerbach et al. 2018) was used to determine lead orientations, which were further checked with post-operative X-ray images. After performing all the above steps, contact locations were described with cartesian XYZ-coordinates in the MNI space, which were then aligned with the anatomical STN from the Distal atlas (Ewert et al. 2018). All analyses were performed in MNI space. Coordinates of contacts implanted into the left STN were converted to right STN analogues with the Lead-DBS toolbox, thus facilitating group analyses.

LFPs were recorded during DBS surgery from all eight contacts simultaneously with the patient awake and at rest. The mean recording duration across hemispheres was 90.7 ± 29.7 s. The recording was conducted with a common average referencing and using a TMSi-Porti amplifier (Twente Medical Systems International, Netherlands) at a sampling

frequency of 2048 Hz.

The electrical signals in the form of the LFPs were processed to detect neural activity signals according to the steps outlined above. PSDs were manually inspected and corrections made in rare cases when the FOOOF algorithm failed to model the data.

To prevent overfitting, a third rejection criterion was applied in addition to the two rejection criteria discussed above. Namely, hemispheres with fewer than four contacts accepted according to the first two rejection criteria were excluded from the study. Four was chosen because this represented half of the contacts available using the DBS lead with which the electrical signals were measured. Seven hemispheres were excluded because they did not have a minimum of four contacts with $\beta$-activity above aperiodic noise levels. Details on contact and hemisphere rejections are shown in Table 3.

| H | Rejection criteria 1 | Rejection criteria 2 | Rejection criteria 3 | Median beta frequency (Hz) |
|---|---|---|---|---|
| | Contacts with beta power | Contacts with high correlation | More than 4 h-c. contacts | |
| 1 | 6 (2) | 5 (1) | P | 15.20 |
| 2 | 0 (8) | | | |
| 3 | 8 (0) | 6 (2) | P | 24.75 |
| 4 | 8 (0) | 6 (2) | P | 23.40 |
| 5 | 7 (1) | 5 (1) | P | 27.75 |
| 6 | 8 (0) | 5 (1) | P | 16.75 |
| 7 | 8 (0) | 5 (3) | P | 22.40 |
| 8 | 8 (0) | 6 (2) | P | 22.35 |
| 9 | 8 (0) | 7 (1) | P | 23.30 |
| 10 | 7 (1) | 5 (2) | P | 16.20 |
| 11 | 8 (0) | 5 (3) | P | 13.10 |
| 12 | 8 (0) | 5 (3) | P | 25.25 |
| 13 | 8 (0) | 5 (3) | P | 15.95 |
| 14 | 8 (0) | 6 (2) | P | 15.15 |
| 15 | 8 (0) | 5 (3) | P | 30.20 |
| 16 | 8 (0) | 6 (2) | P | 29.40 |
| 17 | 7 (1) | 5 (2) | P | 25.20 |
| 18 | 8 (0) | 6 (2) | P | 13.10 |
| 19 | 0 (8) | | | |
| 20 | 6 (2) | 4 (2) | P | 22.95 |
| 21 | 8 (0) | 4 (4) | P | 15.30 |
| 22 | 6 (2) | 4 (2) | P | 13.10 |
| 23 | 8 (0) | | | |
| 24 | 0 (8) | | | |
| 25 | 0 (8) | | | |
| 26 | 0 (8) | | | |
| 27 | 0 (8) | | | |
| **M ± STD** | 7.55 ± 0.76 | 5.25 ± 0.79 | - | 20.54 ± 5.71 |

H = hemisphere, h-c = highly correlated, P = pass, (N) = number of rejected contacts
M = mean, std = standard deviation

**Table 3**

As in the example of Fig. 7, data lags were summarized in 8 × 8 matrices, with each entry describing the lag between the neural activity signals detected at two contacts calculated based on the burst signals. Cross-correlation matrices were symmetrical across their diagonals, which were filled with ones, as shown in Fig. 10. In Fig. 10, H = hemisphere. $R_{jk}$ = normalized cross-correlation coefficient. Entries for rejected contacts

appear white in the figures. Lag matrices were antisymmetrical across their diagonals, which were filled with zeros, as shown in Fig. 11. In Fig. 11, H = hemisphere, $\beta - freq.$ = hemisphere's peak beta frequency.

To provide an intuitive metric for model performance, models were evaluated with correlation coefficients instead of relying on the model cost as an estimate. Agreement between data and model lags was assessed with non-parametric statistics, using Spearman's Rank-Order Correlation Coefficients (SRCC, $\rho$). Importantly, higher SRCCs correspond to more accurate models with a lower cost. Since the data and model lag matrices contained redundant information and were antisymmetric across the diagonal, only the lower triangle below the diagonals was used for calculating SRCC. For a given hemisphere, a model was classified as successful if it significantly fitted the data lags well ($\rho > 0.5$ and $p < 0.05$). Additionally, the model's $\rho$ had to be greater than the $95^{th}$ percentile $\rho$ of a surrogate distribution obtained from fitting randomly shuffled burst signals as described below.

A surrogate distribution of correlation coefficients obtained from shuffled burst signals was used to control for overfitting. For each hemisphere, the burst signals of all accepted contacts were separated into multiple segments. The segment length was set at 5% of the total recording time to maintain the integrity of individual bursts as much as possible. For example, a 100s recording would, according to this procedure, be separated into 20 segments of 5s each. Segments were then randomly allocated across the hemisphere's accepted contacts to generate spatiotemporally dissociated burst data for each contact. Data lags were calculated as outlined in Eq. 4. Model lags were obtained by performing the optimizations described above. The model performance on the shuffled signals was estimated with SRCCs. This shuffling analysis was performed 5120 times for each accepted hemisphere to construct a distribution of $\rho$ values for predictions on the shuffled data sets.

The magnitude of the optimized wave speeds (v) was monitored across all three models to determine if the predicted speeds were within the physiological range. The ranges of cortical $\beta$- and hippocampal $\theta$-waves were displayed alongside the distribution of predicted wave speeds.

The model performance was also calculated using LFPs bandpass filtered around different centre frequencies. Understanding the model performance at different oscillatory

frequencies is insightful for two reasons. First, reconstructing the single point-source model for signals obtained from various oscillatory frequencies could establish whether STN traveling waves are present at different frequencies. Second, this analysis can provide an additional control for overfitting. A consistently good reconstruction at various oscillatory frequencies other than the physiologically expected range would indicate that our model can fit any signal.

It was expected that the reconstruction of sources would be most accurate with LFPs bandpass-filtered in the $\beta$-range. The source reconstruction was performed with LFPs filtered around different centre frequencies (CFs, filter-width ± 3Hz), ranging from 5 Hz to 86 Hz with a step size of 1.27 Hz. The model performance ($\rho$) was plotted against the CF of the bandpass filter. Subsequently, a group-level analysis was performed by plotting the mean $\rho$ across hemispheres for each CF. A paired two-sample t-test was performed to test if the model performance for CFs within the $\beta$-range (13 Hz $<$ CF $<$ 35 Hz) was better than outside (CF $<$ 13 Hz or 35 Hz $<$ CF). Therefore, for each hemisphere, $\rho$-values for CFs within and outside the $\beta$-range were averaged. This provided a single $\rho$ estimate for each hemisphere within and outside the $\beta$-range. The t-test was validated by confirming that the average $\rho$-distributions were normally distributed (Anderson-Darling test) and had equal variances (two-sample F-test).

The results for the single point-source model for a representative hemisphere with good reconstruction are shown in Fig. 12A-C. Fig. 12A shows an example of a data lag matrix showing the delays between the burst signals of contact pairs in hemisphere three. The white rows indicate rejected contacts. Fig. 12B shows the optimized lag predictions for the same hemisphere with the single point-source model.

Fig. 12C shows that the optimized single point-source model approximated the data lags well, as indicated by the high SRCC ($\rho = 0.569$) between the data and model lags shown in Fig. 12A and Fig. 12B. The correlation between data and model lags was significant ($p^* = 0.027$). In this context, high SRCCs indicate good models with low cost. Fig. 13 shows the full set of fitted lag matrices in the single point-source model. White rows correspond to rejected contacts. H = hemisphere, v = wave speed. Across all hemispheres with high correlation coefficients greater than the threshold of 0.50, the performance of the single point-source model was unlikely to be caused by chance ($p <$

0.05, see also Table 4).

In all nine hemispheres in which the single point-source model fitted the data lags well ($\boldsymbol{\rho > 0.5}$, p<0.05), the model performance was better than the 95$^{th}$ percentile of the surrogate distribution obtained from shuffled burst signals (Table 4). A representative case is displayed in Fig. 12D, in which the correlation coefficient of the data was larger than the $95^{th}$ percentile of a $\rho$ distribution obtained through random spatio-temporal shuffling of beta bursts. This indicates that the single point-source model performs worse on random beta burst signals. In Fig. 12D, H = hemisphere, n = number of shuffles, 95th = $\rho$ corresponding to the $95^{th}$ percentile of the distribution, data = $\rho$ of actual data. Fig. 14 shows a similar shuffling analysis for the single point-source model across all hemispheres. In Fig. 14, H = hemisphere, n = number of shuffles, 95th = $\rho$ corresponding to the $95^{th}$ percentile of the distribution, data = $\rho$ of actual data.

Fig. 15 shows the predicted source position for the same representative hemisphere as shown in Fig. 12. The source was relatively close to the contacts. The STN is a generic left STN in MNI space taken from the DISTAL Atlas (Ewert et al. 2018). H = hemisphere, Rej. Contacts = rejected contacts. Fig. 16 shows the full set of predicted source positions in the single point-source model. The STN is again a generic STN in MNI space. It can be seen that the predicted source locations were often within or close to the generic STN.

Fig. 17 shows the reconstruction performance of the single point-source model at different oscillatory frequencies (i.e. different bandpass filter centre frequencies). Since elevated $\beta$-oscillations in the STN are indicative of PD, it was expected that model performance would peak with frequencies in the $\beta$-band.

Fig. 17A shows model performance of hemisphere three. Fig. 17B shows the average model performance across all accepted hemispheres. Reconstruction peaked in the $\beta$-range. The model performance in the alpha and gamma range was worse compared to the $\beta$-band. This indicates that the single point-source model cannot fit LFPs at any frequency and so overfitting was unlikely. This also suggests a lack of evidence for other types of traveling waves beyond $\beta$-oscillation being present in the electrical signals. However, using the model in different frequency ranges may still be useful in other brain regions depending on what condition is of interest.

Fig. 17C shows a comparison of the model performance with signals extracted

within and outside the $\beta$-range. “Within" refers to CFs in the $\beta$-range (blue areas in panels A and B), and “outside" to all other CFs. Each blue and orange dot is the average $\rho$ of a hemisphere. Overall, the model performance was statistically better using $\beta$-oscillations (Paired two-sample t-test: Student’s t = 4.04, $p^{***} = 2.52 \times 10^{-4}$, n = 20 hemispheres). This confirmed the statistical significance of better reconstructions with signals extracted from the $\beta$-band. In Fig. 17, H = hemisphere, Freq $\rho$ = model performance at different CFs of the bandpass filter, Data FR = $\beta$-frequency used for this hemisphere, Mean $\rho$ = average model performance at different CFs, Mean FR = average $\beta$-frequency across all hemispheres, SEM = standard error of the mean.

Fig. 18 shows the distribution of wave speeds in the single point-source model. The median wave speed was 0.233 mm/ms. Most of the predicted speeds were physiologically plausible and are in accordance with previously reported traveling wave speeds. The range for traveling cortical $\beta$-waves was drawn from Mohan, Zhang, and Jacobs 2022, and sub-cortical theta-wave speeds from Zhang and Jacobs 2015.

Results for the two-point source model for a representative hemisphere are shown in Fig. 19A-C. Fig. 19A shows the data lag matrix showing the delays between the beta burst signals of contact pairs. The white rows indicate rejected contacts. Fig. 19B shows optimized lag predictions for the same hemisphere as Fig. 19A with the two point-source model.

Fig. 19C demonstrates that the optimized model approximated the data lags well, as indicated by the high SRCC ($\rho$ = 0.816) between the data and model lags shown in Fig. 19A and Fig. 19B. The correlation between data and model lags was unlikely to be a random effect ($p^{***} = 2.0 \times 10^{-4}$). Fig. 20 shows the full set of fitted lag matrices in the two point-source model. White rows correspond to rejected contacts. H = hemisphere, v = wave speed. The two-point source model fitted the data lags well in 14 out of 20 hemispheres. In the other six hemisphere, the two point-source model could not account for the data lags.

Fig. 19D shows that the correlation coefficient of the data was larger than the $95^{th}$ percentile of a $\rho$ distribution obtained through random spatio-temporal shuffling of beta bursts. In Fig. 19, H = hemisphere, C = contact, $\beta$-freq. = hemisphere’s peak beta frequency, v = optimized wave speed, SRCC = Spearman’s rank-order correlation

coefficient ($\rho$). Fig. 21 shows the full set of shuffling analysis results for the two point-source model across all hemispheres. The distribution was obtained through spatio-temporal shuffling of beta-bursts. H = hemisphere, n = number of shuffles, 95th = $\rho$ corresponding to the $95^{th}$ percentile of the distribution, data = $\rho$ of actual data. The two-source model performs much worse on random beta burst signals, indicating overfitting is unlikely.

Fig. 22 shows the predicted point source positions for the same representative hemisphere corresponding to the data shown in Fig. 19. The two point source positions were close to each other and near the centre of the STN. The STN is a generic left STN in MNI space taken from the DISTAL Atlas (Ewert et al. 2018). H = hemisphere, Rej. Contacts = rejected contacts.

Fig. 23 illustrates the variability in the distance between the two point sources in the two point-source model. In hemisphere 22, the “sources" were relatively close, whereas in hemisphere 3 the distance between the estimated positions was comparably larger. These hemispheres are representative of similar cases across the population. Fig. 24 shows the full set of predicted source positions for all hemispheres in the two point-source model. The STN is again a generic STN in MNI space. The two point sources were relatively close to each other in some of the other hemispheres (H = 3, 9, 11, 12, 13, 17, 21, 22).

Using the same approach as for the single point-source model, the relationship between oscillatory frequency and model performance in the two point-source model was investigated. Fig. 25 shows reconstruction performance of the two point-source model at different oscillatory frequencies. Fig. 25A shows model performance of hemisphere 16. Fig. 25B shows average model performance across all accepted hemispheres. The reconstruction was statistically higher and peaked in the $\beta$-range. This illustrated that overfitting was unlikely.

Fig 13C shows a comparison of the two point-source model performance with signals extracted within and outside the $\beta$-range. “Within” refers to CFs in the blue segment of panels A and B, and ”outside" to all other CFs. Each blue and orange dot is the average $\rho$ of a hemisphere. Overall, the model performance was statistically better using LFPs extracted from the $\beta$-band (Paired two-sample t-test: Student’s t = 5.66, $p^{***} = 1.67 \times 10^{-6}$, n = 20 hemispheres). H = hemisphere, Freq $\rho$ = model performance at

different CFs of the bandpass filter, Data FR = $\beta$-frequency used for this hemisphere, Mean $\rho$ = average model performance at different CFs, Mean FR = average $\beta$-frequency across all hemispheres. SEM = standard error of the mean.

At low travelling wave speeds, the model parameters of the two point-source model are non-identifiable (i.e. several source positions result in similar costs). For LFPs extracted from the beta range (f = 13-35 Hz), the parameters of Eq. 10-12 become non-identifiable in the STN when v is lower than approximately 0.3 mm/ms. This is illustrated in Fig. 26. Fig. 26A shows that at a constant beta-frequency (f), for speeds below 300 mm/s (0.3 mm/ms), multiple distance combinations ($S_1C_i$ and $S_2C_i$) between the sources ($S_1$ and $S_2$) and a given contact ($C_i$) could lead to the same signal phase at $C_i$ ($\psi_i$). Distance combinations resulting in the same $\psi_i$ are color-coded. Raising the wave speed above 300 mm/s as shown in Fig. 26B resolves the indeterminacy described in Fig. 26A, such that for each recorded signal phase $\psi_i$, there is only one pair of $S_1C_i$ and $S_2C_i$. The vertical surfaces in Fig. 26B represent discontinuities and should be ignored. f = hemisphere's peak beta frequency, v = wave speed.

For this reason, the minimum speed was limited to 0.3 mm/ms in the two point-source model. Wave speed predictions in the two point-source model therefore represented an upper limit of the possible speed observed in a hemisphere. In more general applications of the method, recording with leads that have more contacts would overcome this limitation, as more recording sites will increase the spatial power of the method by refining the cost landscape.

Fig. 27 shows the distribution of maximum wave speeds in the two point-source model. Across hemispheres, the upper limits of wave speeds were within the physiological range. The range for traveling cortical $\beta$-waves was drawn from Mohan, Zhang, and Jacobs 2022, and sub-cortical theta-wave speeds came from Zhang and Jacobs 2015.

The planar source model illustrates that the method could be used to account for the presence of other possible traveling wave shapes. Results for a representative fit for the planar source model are shown in Fig. 28. In Fig. 28, H = hemisphere, C = contact, $\beta$-freq. = hemisphere's peak beta frequency, v = optimized wave speed, SRCC = Spearman's Rank-order correlation coefficient ($\rho$). Fig. 28A shows an example of a data lag matrix showing the delays between the beta burst signals of contact pairs in hemisphere 14. Fig. 28B shows optimized lag predictions for the same hemisphere with the planar model. The

white rows indicate rejected contacts.

Fig. 28C shows that the optimized planar model failed to approximate the data lags well ($\rho = 0.356$). This indicates that planar waves are unlikely to be present in the parkinsonian STN. Fig. 29 shows the full set of fitted lag matrices in the planar neural sheet source model. White rows correspond to rejected contacts. H = hemisphere, v = wave speed. The fit to contacts' lags with the planar source model was only plausible in a single hemisphere (H = 3). In a second hemisphere (H = 20), the p-value of the SRCC between model and data lags was significant. However, the coefficient was strongly negative, likely indicating that the optimizer failed to identify a plausible source position.

Fig. 28D shows the position and orientation of the planar source corresponding to the same hemisphere as in Fig. 19A-C. Fig. 30 shows the full set of predicted source positions in the planar source model for all hemispheres. The STN is a generic STN in MNI space.

Fig. 31 shows planar wave speeds predicted for the planar source model. In contrast to both spherical wave models, predicted speeds for the planar waves were slower than previously reported traveling brain waves and are outside the physiological range. The range for traveling cortical $\beta$-waves was drawn from Mohan, Zhang, and Jacobs 2022, and sub-cortical theta-wave speeds came from Zhang and Jacobs 2015.

The results establish that the single point-source and two point-source models both approximate the data lags well, as shown in Table 4. Spherical beta-waves emerging from a single point-source were consistent with data from 9 out of 20 hemispheres. Spherical waves emerging from two point-sources were consistent with data from 14 hemispheres. Predicted wave speeds for both point-source models agreed with previously reported speeds in other structures. Probabilistic maps calculated for source positions demonstrated that sources are most likely located in the anterior portion of the motor STN. Although the planar source model as not effective in the application to detecting beta frequency signals in the parkinsonian STN, it may nonetheless be applicable to other neural activity signals or other parts of the brain.

Table 4 provides an overview of model performance for all three models. A "pass" was assigned to models which were statistically significant $\rho>0.5$ and $p<0.05$). "Successful" hemispheres, highlighted in blue, additionally survived the shuffling control. No shuffling analysis was performed for the planar model given its performance.

| Model | | One point-source | | | Two point-source | | | Planar | |
|---|---|---|---|---|---|---|---|---|---|
| H | PQ | ρ | p | $S_{95}\rho$ | ρ | p | $S_{95}\rho$ | ρ | p |
| 1 | Yes | 0.22 | 0.54 | 0.59 | 0.85 | $1.8 \times 10^{-3}$ | 0.60 | -0.22 | 0.54 |
| 2 | No | | | | | | | | |
| 3 | Yes | 0.57 | 0.027 | 0.51 | 0.67 | $6.7 \times 10^{-3}$ | 0.51 | 0.56 | 0.029 |
| 4 | Yes | 0.16 | 0.58 | 0.52 | 0.58 | 0.023 | 0.51 | -0.14 | 0.60 |
| 5 | Yes | 0.16 | 0.66 | 0.61 | 0.60 | 0.073 | 0.61 | -0.28 | 0.43 |
| 6 | Yes | 0.72 | 0.024 | 0.59 | 0.81 | 0.010 | 0.60 | 0.56 | 0.096 |
| 7 | Yes | 0.66 | 0.040 | 0.59 | 0.51 | 0.13 | 0.60 | -0.34 | 0.34 |
| 8 | Yes | 0.60 | 0.018 | 0.53 | 0.77 | $7.3 \times 10^{-4}$ | 0.53 | 0.50 | 0.055 |
| 9 | Yes | 0.31 | 0.17 | 0.43 | 0.75 | $8.8 \times 10^{-5}$ | 0.43 | -0.11 | 0.65 |
| 10 | Yes | 0.24 | 0.51 | 0.64 | 0.57 | 0.083 | 0.61 | 0.45 | 0.18 |
| 11 | Yes | 0.10 | 0.78 | 0.60 | 0.76 | 0.010 | 0.59 | -0.092 | 0.80 |
| 12 | Yes | 0.83 | $2.8 \times 10^{-3}$ | 0.61 | 0.83 | $2.8 \times 10^{-3}$ | 0.61 | 0.48 | 0.16 |
| 13 | Yes | 0.49 | 0.15 | 0.60 | 0.82 | $6.8 \times 10^{-3}$ | 0.59 | 0.10 | 0.78 |
| 14 | Yes | 0.64 | 0.010 | 0.52 | 0.72 | $2.5 \times 10^{-3}$ | 0.51 | 0.36 | 0.19 |
| 15 | Yes | 0.66 | 0.040 | 0.61 | 0.89 | $1.4 \times 10^{-3}$ | 0.61 | 0.55 | 0.10 |
| 16 | Yes | 0.03 | 0.91 | 0.48 | 0.82 | $2.0 \times 10^{-4}$ | 0.49 | -0.054 | 0.84 |
| 17 | Yes | -0.32 | 0.36 | 0.59 | 0.579 | 0.079 | 0.576 | -0.59 | 0.072 |
| 18 | Yes | 0.33 | 0.23 | 0.51 | 0.39 | 0.15 | 0.51 | 0.36 | 0.18 |
| 19 | No | | | | | | | | |
| 20 | Yes | 0.31 | 0.56 | 0.77 | 0.89 | 0.033 | 0.77 | -0.88 | 0.033 |
| 21 | Yes | 0.94 | 0.017 | 0.77 | 0.83 | 0.058 | 0.77 | -0.09 | 0.92 |
| 22 | Yes | 0.94 | 0.017 | 0.77 | 0.89 | 0.033 | 0.77 | 0.14 | 0.80 |
| 23 | No | | | | | | | | |
| 24 | No | | | | | | | | |
| 25 | No | | | | | | | | |
| 26 | No | | | | | | | | |
| 27 | No | | | | | | | | |
| Total | | 9/20 successful | | | 14/20 successful | | | 1/20 pass | |
| N | | 1000 | | | 10000 | | | 1000 | |

H = hemisphere, PQ = passed quality control (rejection criteria 1-3), N = number of starting points, ρ = Spearman's rank-order correlation coefficient between data and model lags, p = p-value corresponding to ρ, $S_{95}\rho$ = ρ corresponding to the 95th percentile of the shuffling distribution.

Hemispheres that did not pass the rejection criteria.

Hemispheres in which the model was not significant, or the shuffling failed.

Hemispheres in which the model was significant, and the shuffling succeeded.

**Table 4**

For most hemispheres that were successful in both the single point source model and the two point-source model, the two point-source model fitted the data lags better than the single point-source model. This is demonstrated in the hemisphere-specific $\rho$-values in Table 4. However, some variability was observed in model performance across hemispheres. For three hemispheres (H = 7, 21, 22), the single point-source model

outperformed the two point-source model. For seven hemispheres (H = 1, 4, 9, 11, 13, 16, 20) for which the single point-source model did not work well, the two point-source model approximated the data lags well. The lags of four hemispheres (H = 5, 10, 17, 18) could not be fitted well with either point-source model. This indicates variability in hemisphere source characteristics which may require different choices of model for different hemispheres. This variability may be indicative of various factors such as the size and spatial consistency of the source of neural activity signals.

For both the single point-source model and the two point-source model, the predicted wave speed estimates agree with the conduction speeds of mono-synaptic unmyelinated connections (0.1-0.6 mm/ms) (González-Burgos, Barrionuevo, and Lewis 2000; Girard, Hupé, and Bullier 2001).

Understanding the likelihood of source locations across the STN can be useful for DBS. For example, if STN locations with a high source probability are known, physicians can target the implantation of leads towards these regions. Anatomically, the stimulation sweet spot for PD is localized in the dorso-lateral region of the STN. A modified version of the single point-source model was implemented to identify areas of low and high cost in the STN, which illustrate the likelihood of source positions across the STN for individual hemispheres. The STN was placed at the center of a $15 \times 15 \times 15$ $3D$ grid, with $15^3$ grid points. For each hemisphere, the wave speed was optimized at each individual grid position $(G_i)$ according to Eqs. 3-5, where source coordinates $(X_S, Y_S, Z_S)$ were replaced with grid coordinates $(X_{G_i}, Y_{G_i}, Z_{G_i})$. Iso-potential surfaces were then drawn with MATLAB's isosurface function. The cost for the points on the surface of the STN was interpolated with the cost of the closest grid point. Therefore, for each point $(P)$ on the surface of the STN, the distance to all points on the grid was calculated. The cost at $P$ was estimated as the cost of the closest grid point. A spatially smooth representation was then created through linear interpolation with MATLAB's interp3 function.

The cost landscapes for two representative hemispheres are shown in Fig. 32. Fig. 32A shows isocost-surfaces (i.e. surfaces of equal cost) for a tight region around the generic STN. The orange dot is the predicted source position of the single point-source model for the hemisphere. Areas of low cost correspond with source positions where data lags can be modelled more accurately. Sources are more likely to be located in such areas.

Fig. 32B shows the interpolated cost landscape for the surface of the STN. Fig. 32C shows isocost-surfaces of another hemisphere. Fig. 32D shows the interpolated cost landscape for the surface for the hemisphere shown in Fig. 32C. Notice the variability in absolute cost (range of the colour scale) and overall landscape between the two hemispheres.

Although hemisphere-specific cost landscapes can be helpful in optimizing DBS, they can only be revealed after implantation. After surgery, the leads might be positioned away from the source so that efficient silencing of $\beta$-activity might not be possible. Therefore, having a rough idea of potential source positions prior to implantation can be beneficial, guiding the selection of implantation sites. To identify areas of high source probability across hemispheres, a population-level analysis was performed to identify overall areas of low cost. Because the absolute cost range was variable across hemispheres, the cost landscape of each hemisphere was scaled to its maximum cost. The average cost landscape was computed as the mean cost landscape across all hemispheres, and is shown in Fig. 33. In line with previous studies, sources were found to be more likely to be in the motor STN. Two regions of low cost (high source probability) were identified in the anterior portion of the motor region and are indicated with arrows in Fig. 33. Compared to the area of highest cost (dark red), the cost was approximately 7% lower in the low-cost regions.

While the motor STN seems a reasonable implantation site for leads, it is likely that exact source locations are variable across hemispheres. Even after implantation, the present hemisphere-specific source-probability landscapes would allow individualized tuning along the dorso-ventral axis by identifying the position of the source along this direction and stimulating at the level of the source.

The above traveling wave models were designed with the smallest number of parameters required to describe the data. This makes the models easily interpretable and prevents overfitting the data lags. The amplitude of beta oscillations is likely partially driven by noise. An advantage of the present methodology is that it is not affected by stochastic amplitude variations. By computing beta-bursts with contact-specific amplitude thresholds, the effect of the interaction between LFP amplitude and distance from the source is avoided.

Computational considerations are an important factor in designing neurophysiology-guided DBS systems. In addition to being easily interpretable, the

present source identification algorithms have relatively low computation times. The main analyses (including data pre-procession and excluding the shuffling and frequency analyses) were conducted on a personal computer. The most computationally-expensive model was the two point-source model, with a run-time of approximately 4.5h for 20 hemispheres. This suggests that the reconstruction for a single hemisphere can be accomplished in roughly 12 minutes, which is a practical time frame in clinical settings to update source positions on a slow time scale. The single-point source approach was considerably faster at approximately 2 minutes per hemisphere. It is expected that these run-times can be significantly improved with optimisation. Furthermore, the mean recording duration across hemispheres was 90.7 ± 29.7s in the data set used above, which demonstrates that the method can be implemented with a reasonable amount of data.

**References**

Anderson, Daria Nesterovich, Braxton Osting, Johannes Vorwerk, Alan D Dorval, and Christopher R Butson. 2018. "Optimized Programming Algorithm for Cylindrical and Directional Deep Brain Stimulation Electrodes." Journal of Neural Engineering 15 (2): 026005.

Avants, Brian B, Nicholas J Tustison, Michael Stauffer, Gang Song, Baohua Wu, and James C Gee. 2014. "The Insight ToolKit Image Registration Framework." Frontiers in Neuroinformatics 8: 44.

Bhattacharya, Sayak, Scott L Brincat, Mikael Lundqvist, and Earl K Miller. 2022. "Traveling Waves in the Prefrontal Cortex During Working Memory." PLOS Computational Biology 18 (1): e1009827.

Brown, Peter, Antonio Oliviero, Paolo Mazzone, Angelo Insola, Pietro Tonali, and Vincenzo Di Lazzaro. 2001. "Dopamine Dependency of Oscillations Between Subthalamic Nucleus and Pallidum in Parkinson's Disease." Journal of Neuroscience 21 (3): 1033–38.

Buhlmann, Julia, Lorenz Hofmann, Peter Alexander Tass, and Christian Hauptmann. 2011. "Modeling of a Segmented Electrode for Desynchronizing Deep Brain Stimulation." Frontiers in Neuroengineering 4: 15.

Byrd, Richard H, Robert B Schnabel, and Gerald A Shultz. 1988. "Approximate Solution of the Trust Region Problem by Minimization over Two-Dimensional Subspaces." Mathematical Programming 40 (1): 247–63.

Chen, Chiung Chu, Alek Pogosyan, Ludvic U Zrinzo, Stephen Tisch, Patricia Limousin, Keyoumars Ashkan, Tarek Yousry, Marwan I Hariz, and Peter Brown. 2006. "Intra-Operative Recordings of Local Field Potentials Can Help Localize the Subthalamic Nucleus in Parkinson's Disease Surgery." Experimental Neurology 198 (1): 214–21.

Diamond, Joshua M, Benjamin E Diamond, Michael S Trotta, Kate Dembny, Sara K Inati, and Kareem A Zaghloul. 2021. "Travelling Waves Reveal a Dynamic Seizure Source in Human Focal Epilepsy." Brain 144 (6): 1751–63.

Donoghue, Thomas, Matar Haller, Erik J Peterson, Paroma Varma, Priyadarshini Sebastian, Richard Gao, Torben Noto, et al. 2020. "Parameterizing Neural Power Spectra into Periodic and Aperiodic Components." Nature Neuroscience 23 (12): 1655–65.

Ewert, Siobhan, Philip Plettig, Ningfei Li, M Mallar Chakravarty, D Louis Collins, Todd M Herrington, Andrea A Kühn, and Andreas Horn. 2018. "Toward Defining Deep Brain Stimulation Targets in MNI Space: A Subcortical Atlas Based on Multimodal MRI, Histology and Structural Connectivity." Neuroimage 170: 271–82.

Girard, P, JM Hupé, and J Bullier. 2001. "Feedforward and Feedback Connections Between Areas V1 and V2 of the Monkey Have Similar Rapid Conduction Velocities." Journal of Neurophysiology 85 (3): 1328–31.

González-Burgos, Guillermo, German Barrionuevo, and David A Lewis. 2000. "Horizontal Synaptic Connections in Monkey Prefrontal Cortex: An in Vitro Electrophysiological Study." Cerebral Cortex 10 (1): 82–92.

Hellerbach, Alexandra, Till A Dembek, Mauritius Hoevels, Jasmin A Holz, Andreas Gierich, Klaus Luyken, Michael T Barbe, Jochen Wirths, Veerle Visser-Vandewalle, and Harald Treuer. 2018. "DiODe: Directional Orientation Detection of Segmented Deep Brain Stimulation Leads: A Sequential Algorithm Based on CT Imaging." Stereotactic and Functional Neurosurgery 96 (5): 335–41.

Hilker, Rüdiger, Jürgen Voges, T Weber, Lutz W Kracht, J Roggendorf, S Baudrexel, Moritz Hoevels, Volker Sturm, and Wolf-Dieter Heiss. 2008. "STN-DBS Activates the Target Area in Parkinson Disease: An FDG-PET Study." Neurology 71 (10): 708–13.

Horn, Andreas, Ningfei Li, Till A Dembek, Ari Kappel, Chadwick Boulay, Siobhan Ewert, Anna Tietze, et al. 2019. "Lead-DBS V2: Towards a Comprehensive Pipeline for Deep Brain Stimulation Imaging." Neuroimage 184: 293–316.

Husch, Andreas, Mikkel V Petersen, Peter Gemmar, Jorge Goncalves, and Frank Hertel. 2018. "PaCER-a Fully Automated Method for Electrode Trajectory and Contact Reconstruction in Deep Brain Stimulation." NeuroImage: Clinical 17: 80–89.

Maling, Nicholas, Scott F Lempka, Zack Blumenfeld, Helen Bronte-Stewart, and Cameron C McIntyre. 2018. "Biophysical Basis of Subthalamic Local Field Potentials Recorded from Deep Brain Stimulation Electrodes." Journal of Neurophysiology 120 (4): 1932–44.

Mohan, Uma Rani, Honghui Zhang, and Joshua Jacobs. 2022. "The Direction and Timing of Theta and Alpha Traveling Waves Modulate Human Memory Processing."

Müller, Thomas, Michael Lauk, Matthias Reinhard, Andreas Hetzel, Carl H Lücking, and Jens Timmer. 2003. "Estimation of Delay Times in Biological Systems." Annals of Biomedical Engineering 31 (11): 1423–39.

Schönecker, Thomas, A Kupsch, AA Kühn, G-H Schneider, and K-T Hoffmann. 2009. "Automated Optimization of Subcortical Cerebral MR Imaging- Atlas Coregistration for Improved Postoperative Electrode Localization in Deep Brain Stimulation." American Journal of Neuroradiology 30 (10): 1914–21.

Shah, Ashesh, Thuy-Anh Khoa Nguyen, Katrin Peterman, Saed Khawaldeh, Ines Debove, Syed Ahmar Shah, Flavie Torrecillos, et al. 2022. "Combining Multimodal Biomarkers to Guide Deep Brain Stimulation Programming in Parkinson Disease." Neuromodulation: Technology at the Neural Interface.

Tamir, Idit, Doris Wang, Witney Chen, Jill L Ostrem, Philip A Starr, and Coralie de Hemptinne. 2020. "Eight Cylindrical Contact Lead Recordings in the Subthalamic Region Localize Beta Oscillations Source to the Dorsal STN." Neurobiology of Disease 146: 105090.

Tinkhauser, Gerd, Alek Pogosyan, Ines Debove, Andreas Nowacki, Syed Ahmar Shah, Kathleen Seidel, Huiling Tan, et al. 2018. "Directional Local Field Potentials: A Tool to Optimize Deep Brain Stimulation." Movement Disorders 33 (1): 159–64.

Tinkhauser, Gerd, Alek Pogosyan, Huiling Tan, Damian M Herz, Andrea A Kühn, and Peter Brown. 2017. "Beta Burst Dynamics in Parkinson's Disease OFF and ON Dopaminergic Medication." Brain 140 (11): 2968–81.

Willsie, Andrew C, and Alan D Dorval. 2015. "Computational Field Shaping for Deep Brain Stimulation with Thousands of Contacts in a Novel Electrode Geometry."

Neuromodulation: Technology at the Neural Interface 18 (7): 542–51.

Zhang, Honghui, and Joshua Jacobs. 2015. “Traveling Theta Waves in the Human Hippocampus.” Journal of Neuroscience 35 (36): 12477–87.

# CLAIMS

1. A method for determining a location of a source of neural activity signals within a brain, the method comprising:

measuring electrical signals from respective contacts of a plurality of contacts located at known relative positions within the brain;

processing the electrical signals to detect neural activity signals in the electrical signals from the respective contacts;

determining timings of the detected neural activity signals; and

determining the location of the source of neural activity within the brain relative to the plurality of contacts by fitting a source model to the timings relative to each other, wherein the source model models an arrangement of the source of the neural activity signals and models the neural activity signals as travelling waves that propagate through the brain.

2. A method according to claim 1, wherein the processing of the electrical signals comprises, for each of the respective contacts, determining a peak frequency for the contact as the frequency having the highest power within a predetermined frequency range.

3. A method according to claim 2, wherein the peak frequency is determined using a net power spectral density calculated by subtracting a background power spectral density from a power spectral density of the electrical signals from the contact,

optionally wherein the background power spectral density comprises an estimated power spectral density of aperiodic noise.

4. A method according to any one of claims 2 to 3, wherein the predetermined frequency range is a range of beta brain wave frequencies, optionally 13-35 Hz.

5. A method according to any one of the preceding claims, wherein the processing of the electrical signals comprises filtering the electrical signals from the respective contacts to detect the neural activity signals, optionally using a frequency bandpass filter.

6. A method according to claim 5 when dependent on any one of claims 2 to 4, wherein the processing of the electrical signals comprises determining a hemisphere peak frequency as an average, optionally a median, of the peak frequencies of contacts within the same hemisphere of the brain, and the frequency bandpass filter is centred on the hemisphere peak frequency,

optionally wherein the hemisphere peak frequency is determined as an average of the peak frequencies of contacts within the same hemisphere of the brain for which a power at the peak frequency of the contact is above a predetermined power threshold.

7. A method according to claim 5, wherein the frequency bandpass filter is configured to pass frequencies within a predetermined frequency range, optionally wherein the predetermined frequency range is a range of beta brain wave frequencies, further optionally 13-35 Hz.

8. A method according to any one of claims 2 to 7, wherein the timings are determined for a subset of the detected neural activity signals, the subset comprising neural activity signals detected at contacts for which a power at the peak frequency of the contact is above a predetermined power threshold.

9. A method according to any one of claims 2 to 8, wherein the timings are determined for a subset of the detected neural activity signals, the subset comprising neural activity signals detected at contacts for which an average of a statistical dependency metric between the neural activity signal for the contact and the neural activity signals for each of the other contacts is above a predetermined correlation threshold.

10. A method according to any one of the preceding claims, wherein the timing between a first detected neural activity signal from a first contact of the plurality of contacts and a second detected neural activity signal from a second contact of the plurality of contacts is a relative timing that, when applied to the first detected neural activity signal, maximises a statistical dependency metric between the first detected neural activity signal and the second detected neural activity signal.

11. A method according to claim 10, wherein the statistical dependency metric is a temporal cross-correlation, a coherence, or a mutual information between the neural activity signal first detected neural activity signal and the second detected neural activity signal.

12. A method according to claim 10 or 11, wherein:

the determining of the timings comprises calculating, for each of the respective contacts, a burst signal representing timings of periods in which an amplitude of the detected neural activity signal from the contact is above a predetermined amplitude threshold; and

the timing between the detected neural signal from the first contact and the detected neural signal from the second contact is a relative timing that, when applied to a first burst signal calculated for the first contact, maximises a statistical dependency metric between the first burst signal and a second burst signal calculated for the second contact.

13. A method according to any one of the preceding claims, wherein:

the determining of the timings comprises identifying, for each of the respective contacts, one or more burst periods in which an amplitude of the detected neural activity signal from the contact is above a predetermined amplitude threshold for at least a predetermined duration;

the timing between a first detected neural activity signal from a first contact of the plurality of contacts and a second detected neural activity signal from a second contact of the plurality of contacts is the relative timing between a first burst period for the first contact and a second burst period for the second contact, the second burst period being a burst period that begins closest in time to the beginning of the first burst period,

optionally wherein the second burst period is a burst period that begins within a predetermined time window around the beginning of the first burst period.

14. A method according to claim 13, wherein:

a plurality of burst periods are identified for each of the respective contacts;

a plurality of relative timings are determined based on a corresponding plurality of first burst periods and second burst periods; and

the timing between the first detected neural activity signal and the second detected neural activity signal is an average of the plurality of relative timings.

15. A method according to any one of the preceding claims, wherein the location of the source is a parameter of the source model, and determining the location of the source by fitting the source model to the timings relative to each other comprises fitting the location.

16. A method according to claim 15, wherein the source model models the arrangement of the source as a point source, and determining the location of the source comprises determining a location of the point source,

optionally wherein the location of the point source is a three-dimensional location relative to the plurality of contacts.

17. A method according to claim 16, wherein the source model assumes activity signals from the point source are emitted as spherical waves.

18. A method according to claim 15, wherein the source model models the arrangement of the source as a plurality of point sources, optionally two point sources, and determining the location of the source comprises determining a location of each of the plurality of point sources,

optionally wherein the location of each of the point sources is a three-dimensional location relative to the plurality of contacts.

19. A method according to claim 18, wherein the source model assumes:

neural activity signals from each of the plurality of point sources have equal amplitude and/or equal phase and/or equal frequency; and/or

neural activity signals from each of the plurality of point sources are emitted as spherical waves.

20. A method according to claim 15, wherein the source model models the arrangement of the source as a planar source, and determining the location of the source comprises determining a location of the planar source and an orientation of the planar source,

optionally wherein the location of the planar source comprises a three-dimensional location relative to the plurality of contacts and the orientation of the planar source comprises a three-dimensional vector normal to the planar source.

21. A method according to any one of the preceding claims, wherein a speed of the travelling waves is a parameter of the source model, and determining the location of the source by fitting the source model to the timings comprises fitting the speed of the travelling waves.

22. A method according to any one of the preceding claims, wherein the electrical signals are time-resolved measurements of local field potentials.

23. A method according to any one of the preceding claims, wherein one or more of the plurality of contacts are within the subthalamic nucleus or the globus pallidus internus of the brain.

24. A method according to any one of the preceding claims, wherein the plurality of contacts are located on the same deep-brain stimulation lead, and/or the plurality of contacts comprises at least four contacts, optionally at least eight contacts.

25. A method according to any one of the preceding claims, wherein the neural activity signals are beta brain waves.

26. A method according to any one of the preceding claims, wherein the neural activity signals have a duration of at least 5 seconds, optionally 10 seconds, optionally at least 30 seconds, optionally at least one minute.

27. A method according to any one of the preceding claims, wherein the neural activity signals have a duration of at most 10 seconds, optionally at most 30 seconds, optionally at most one minute, optionally at most 5 minutes.

28. A computer program comprising, or a computer-readable medium having stored

thereon, instructions which, when carried out by a computer, cause the computer to carry out the method of any of the preceding claims.

29. A method for selecting contacts of a deep-brain stimulation lead within a brain for use in deep-brain stimulation comprising:

determining a location of a source of neural activity signals within the brain according to the method of any of claims 1-27; and

selecting one or more contacts of the deep-brain stimulation lead based on the location.

30. A method according to claim 29, further comprising determining a stimulation energy for application at each of the one or more selected contacts based on the location.

31. A method according to claim 29 or 30, further comprising repeating the steps of determining the location, selecting one or more contacts, and, if performed, determining the stimulation energy in response to a predetermined condition being met, optionally wherein the predetermined condition is the elapsing of a predetermined length of time.

32. An apparatus for determining a location of a source of neural activity signals within a brain comprising:

a measurement unit configured to measure electrical signals from respective contacts of a plurality of contacts located at known relative positions within the brain;

a processing unit configured to process the electrical signals to detect neural activity signals in the electrical signals from the respective contacts; and

a determining unit configured to:

determine timings of the detected neural activity signals; and

determine the location of the source of neural activity within the brain relative to the plurality of contacts by fitting a source model to the timings relative to each other, wherein the source model models an arrangement of the source of the neural activity signals and models the neural activity signals as travelling waves that propagate through the brain.

Fig. 1

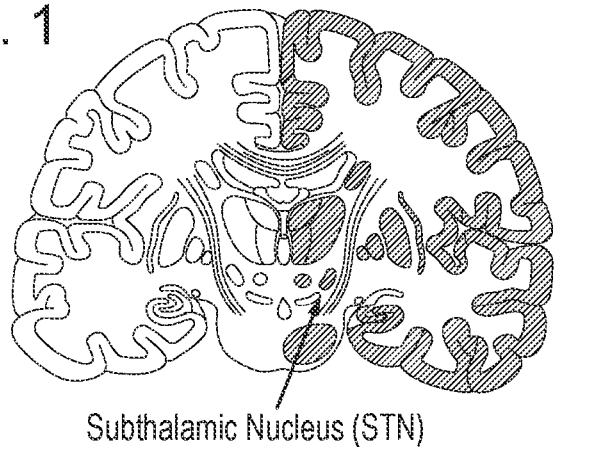
Subthalamic Nucleus (STN)
ventral-dorsal (mm)
-4
-6
-8
-10
-12
-10
-15
-20
anterior-posterior (mm)
6
8
10
12
14
16
medial-lateral (mm)

Fig. 2

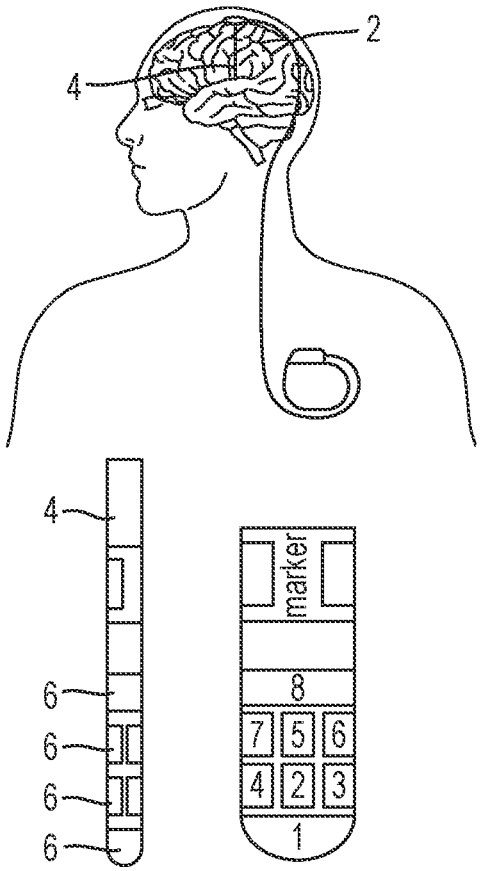
2
4
4
6
6
6
6
marker
8
7
5
6
4
2
3
1

Fig. 3

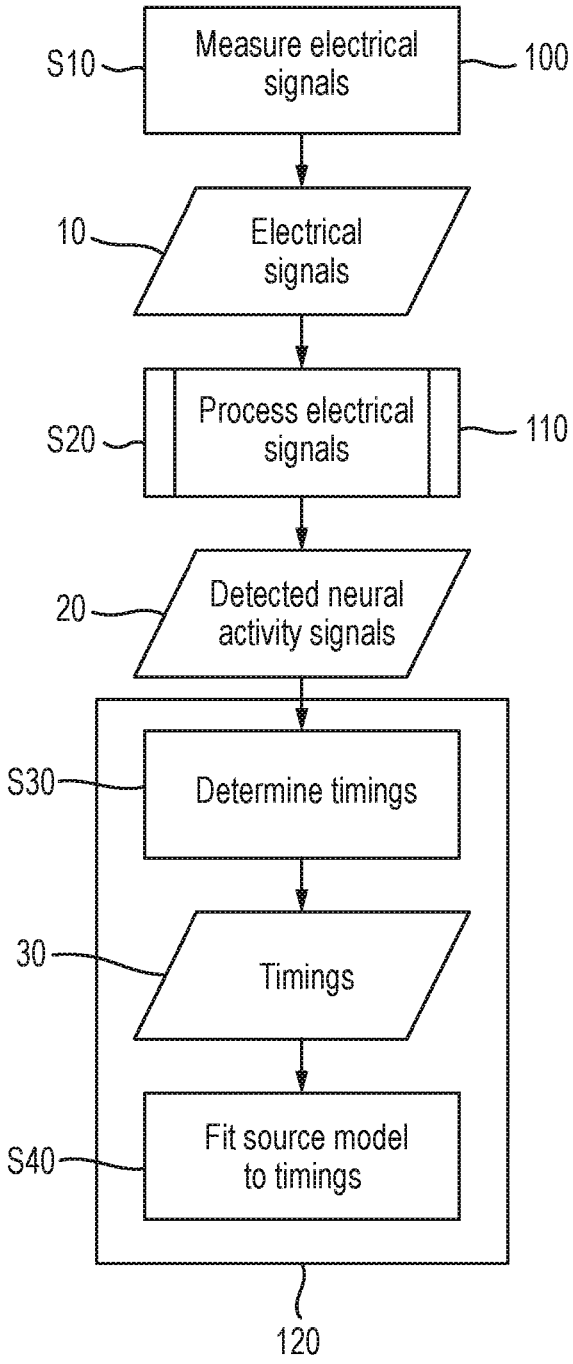
S10
Measure electrical signals
100
10
Electrical signals
S20
Process electrical signals
110
20
Detected neural activity signals
S30
Determine timings
30
Timings
S40
Fit source model to timings
120

Fig. 4

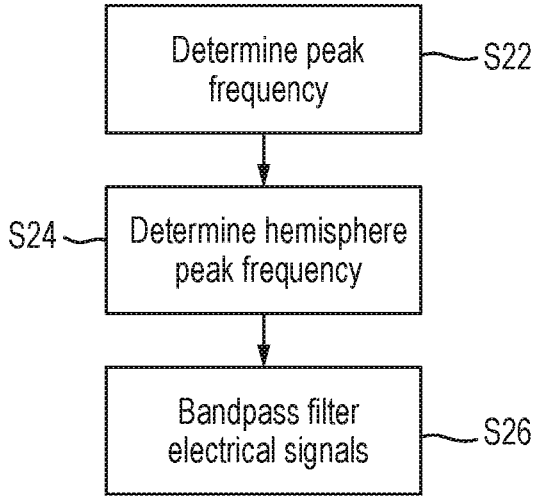
Determine peak frequency
S22
S24
Determine hemisphere peak frequency
Bandpass filter electrical signals
S26

Fig. 5A

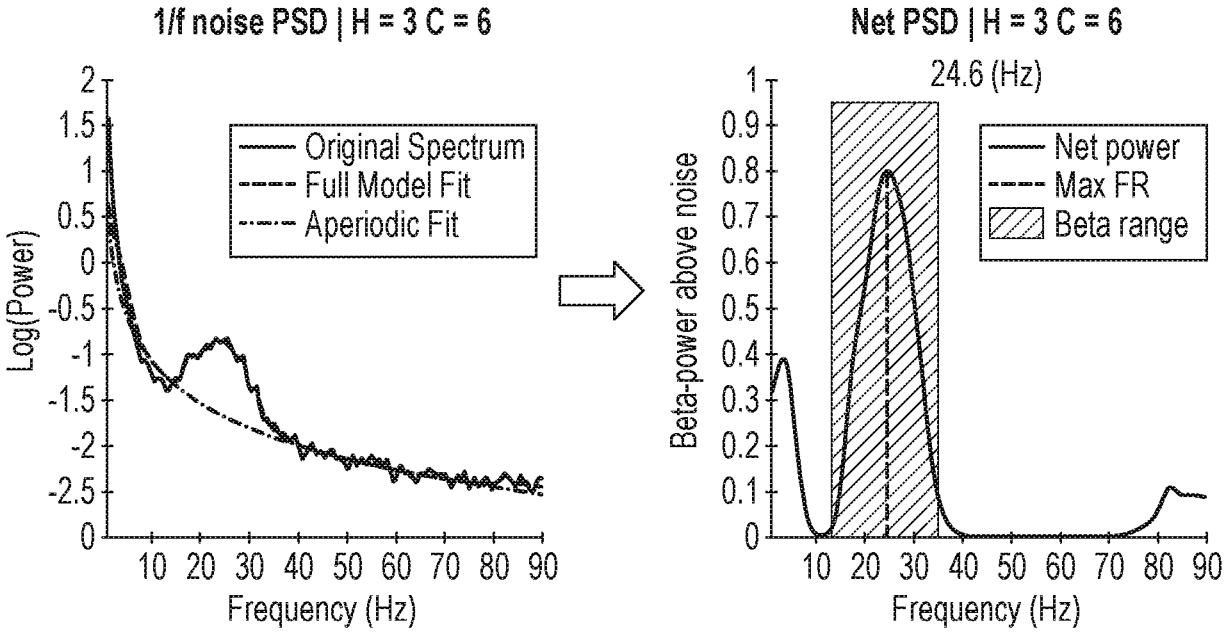
1/f noise PSD | H = 3 C = 6
Original Spectrum
Full Model Fit
Aperiodic Fit
Log(Power)
Frequency (Hz)
Net PSD | H = 3 C = 6
24.6 (Hz)
Net power
Max FR
Beta range
Beta-power above noise
Frequency (Hz)

Fig. 5B

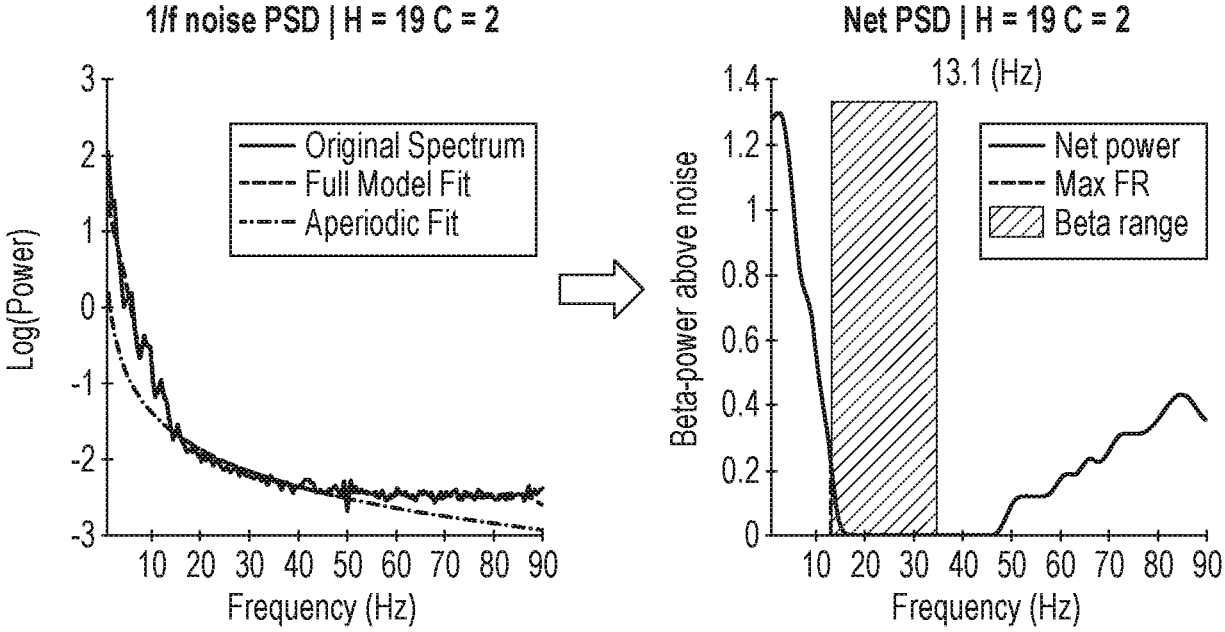
1/f noise PSD | H = 19 C = 2
Original Spectrum
Full Model Fit
Aperiodic Fit
Log(Power)
Frequency (Hz)
Net PSD | H = 19 C = 2
13.1 (Hz)
Net power
Max FR
Beta range
Beta-power above noise
Frequency (Hz)

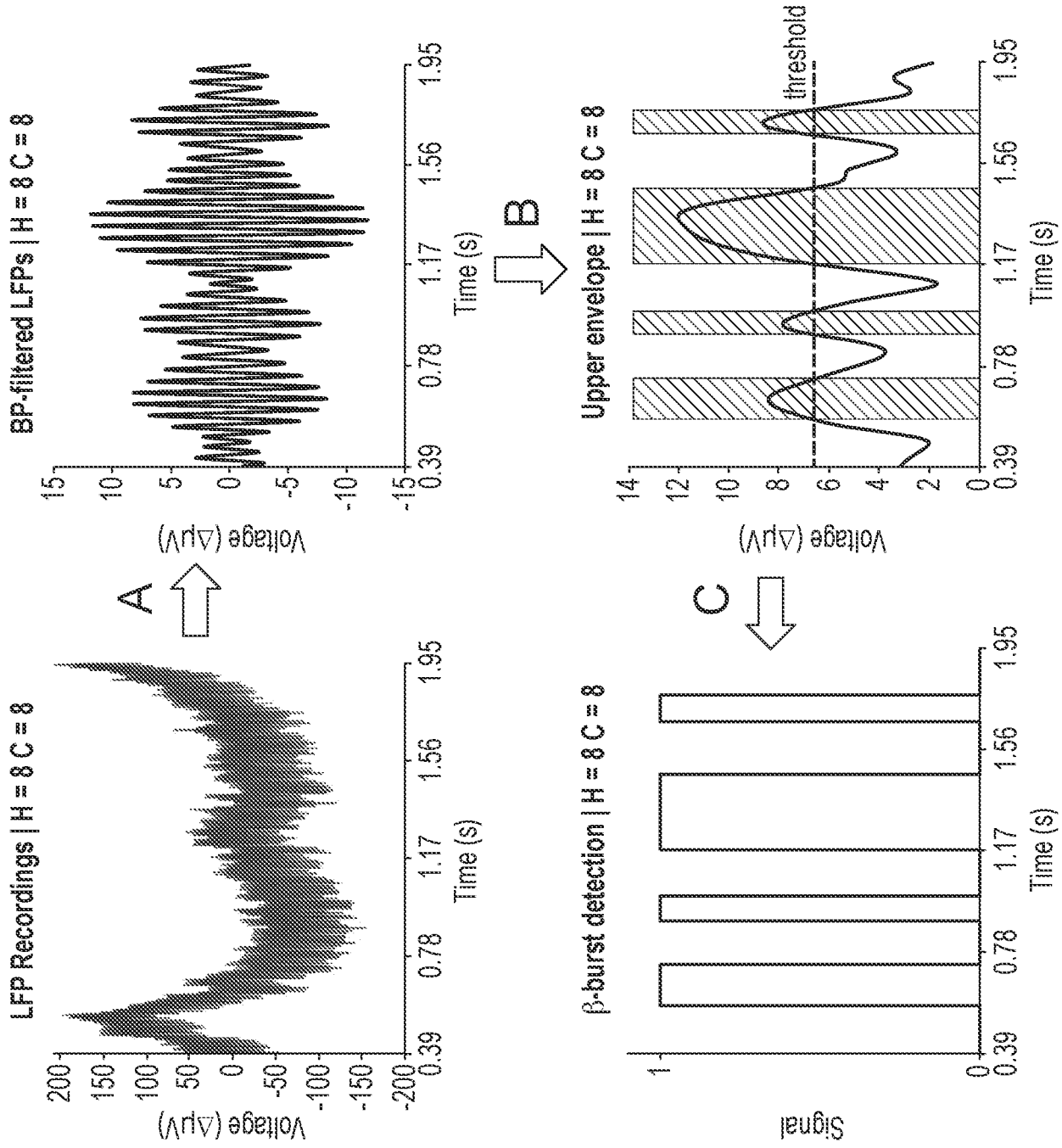
LFP Recordings | H = 8 C = 8
Voltage (△μV)
Time (s)
A
BP-filtered LFPs | H = 8 C = 8
Voltage (△μV)
Time (s)
B
Upper envelope | H = 8 C = 8
threshold
Voltage (△μV)
Time (s)
C
β-burst detection | H = 8 C = 8
Signal
Time (s)

Fig. 6

Fig. 7A

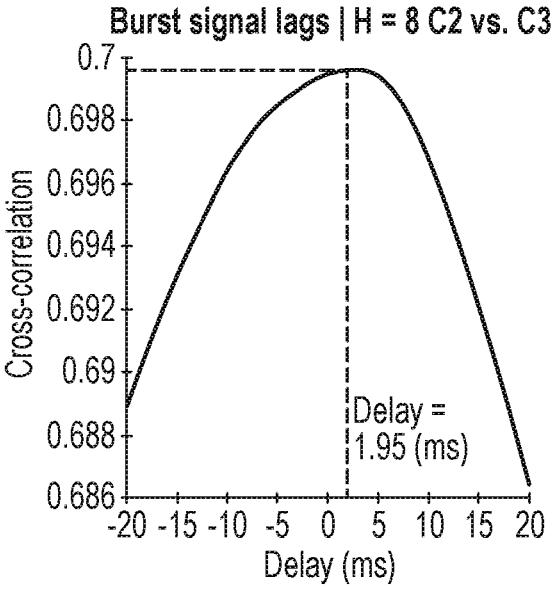


Fig. 7D

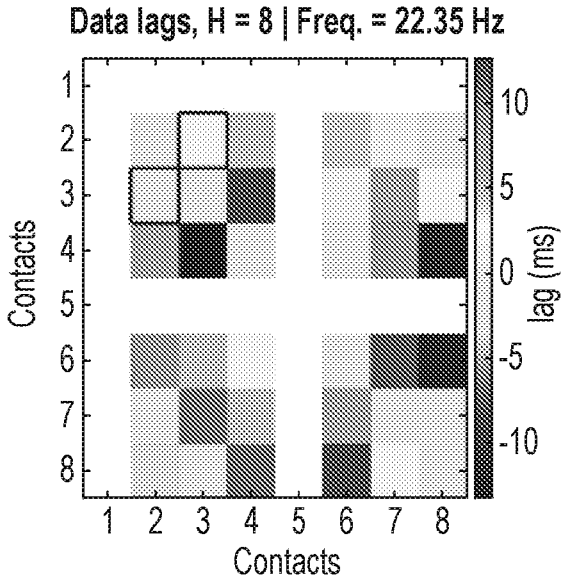


Fig. 7B

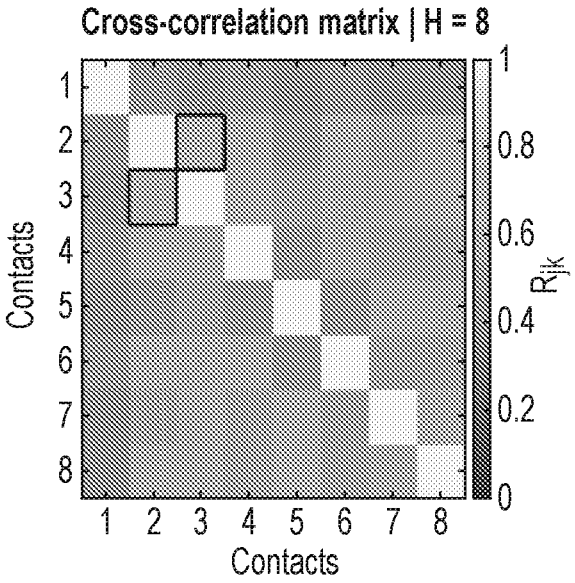


Fig. 7C

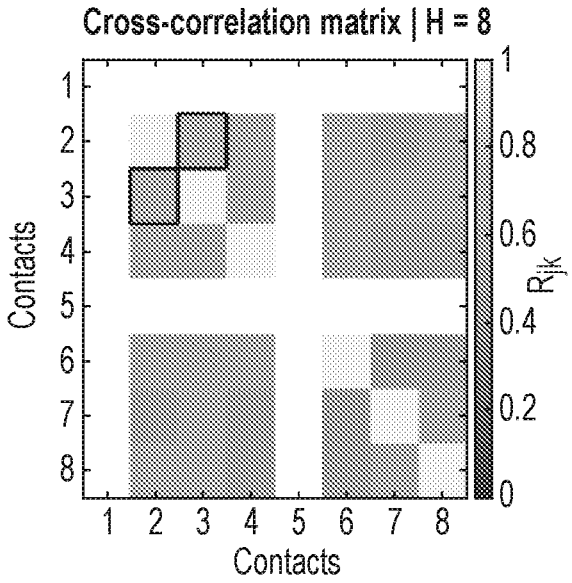

Fig. 8A

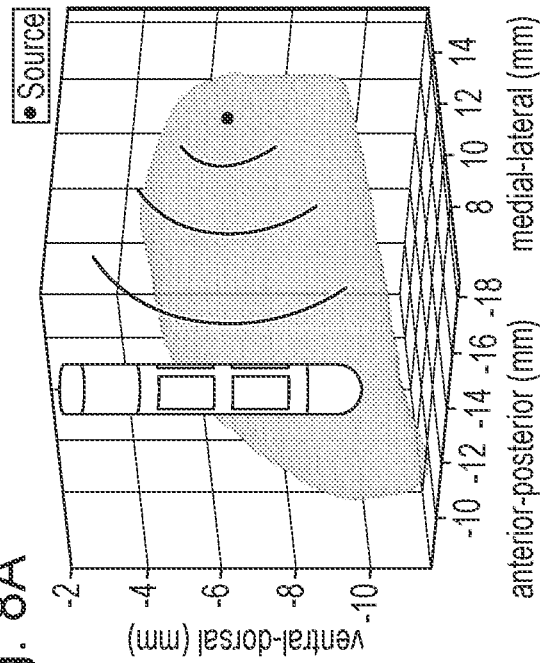


Fig. 8B

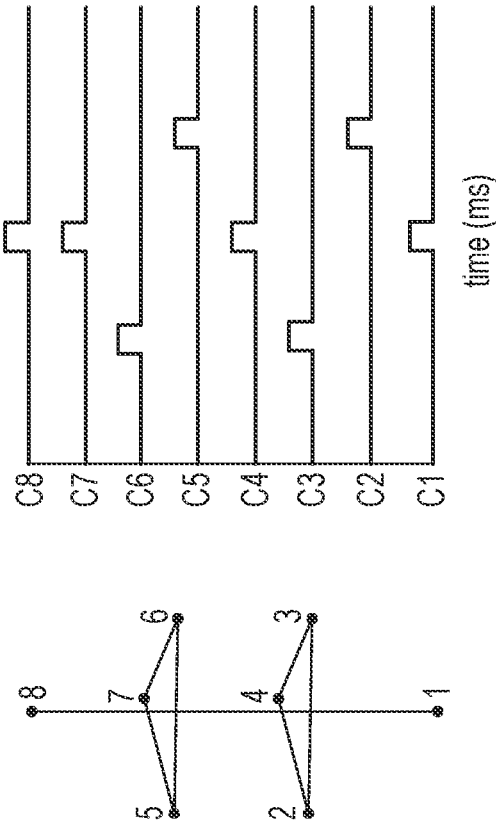


Fig. 8C

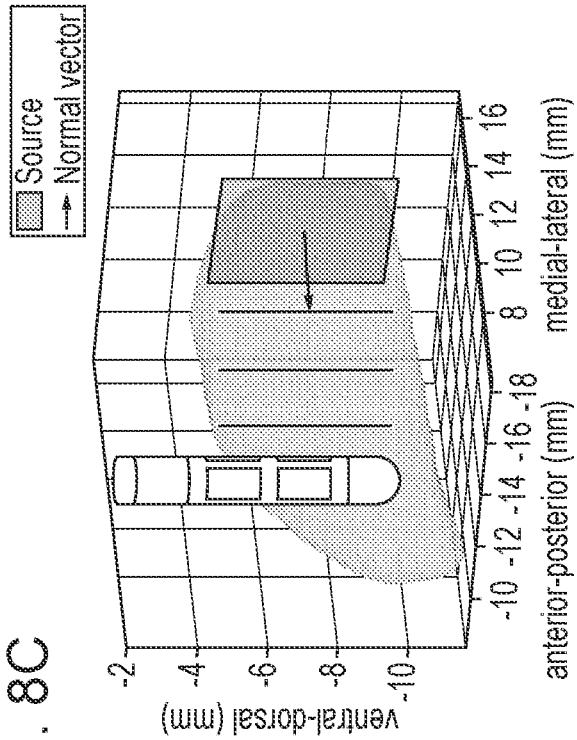


Fig. 8D

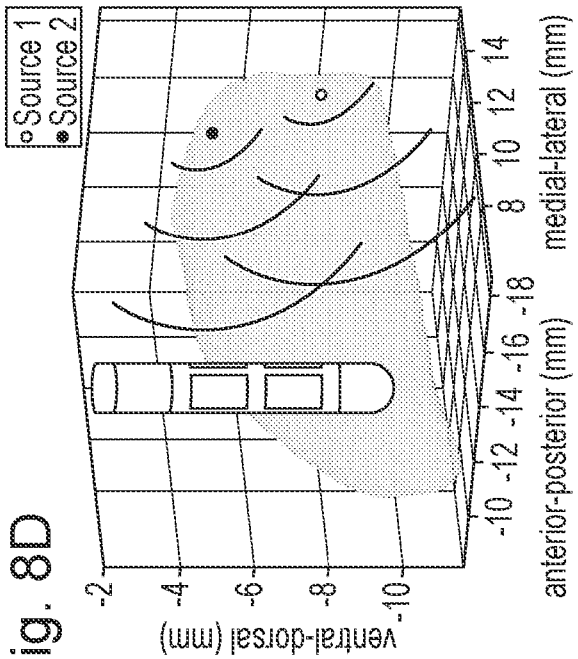

Fig. 9

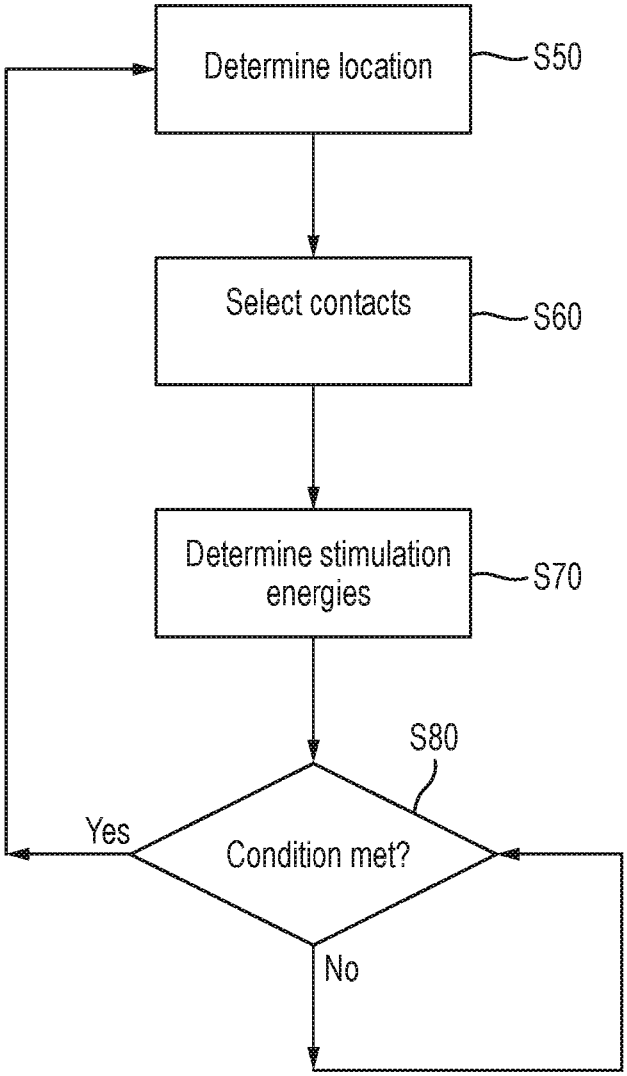
Determine location
S50
Select contacts
S60
Determine stimulation energies
S70
S80
Condition met?
Yes
No

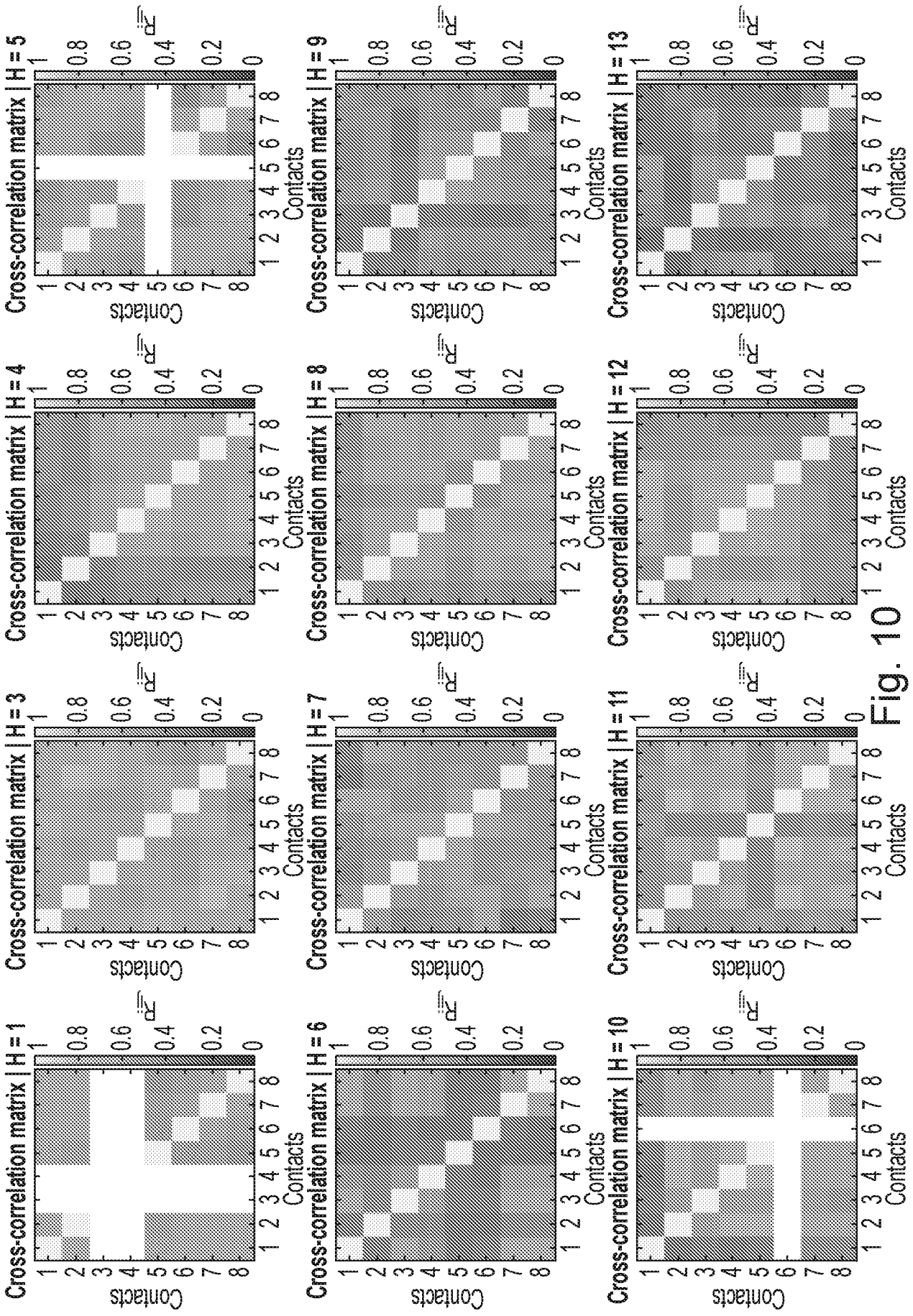
Cross-correlation matrix | H = 1
Cross-correlation matrix | H = 2
Cross-correlation matrix | H = 3
Cross-correlation matrix | H = 4
Cross-correlation matrix | H = 5
Cross-correlation matrix | H = 6
Cross-correlation matrix | H = 7
Cross-correlation matrix | H = 8
Cross-correlation matrix | H = 9
Cross-correlation matrix | H = 10
Cross-correlation matrix | H = 11
Cross-correlation matrix | H = 12
Cross-correlation matrix | H = 13
Contacts
1 2 3 4 5 6 7 8
1 0.8 0.6 0.4 0.2 0
CR

Fig. 10

Fig. 10 (Cont.)

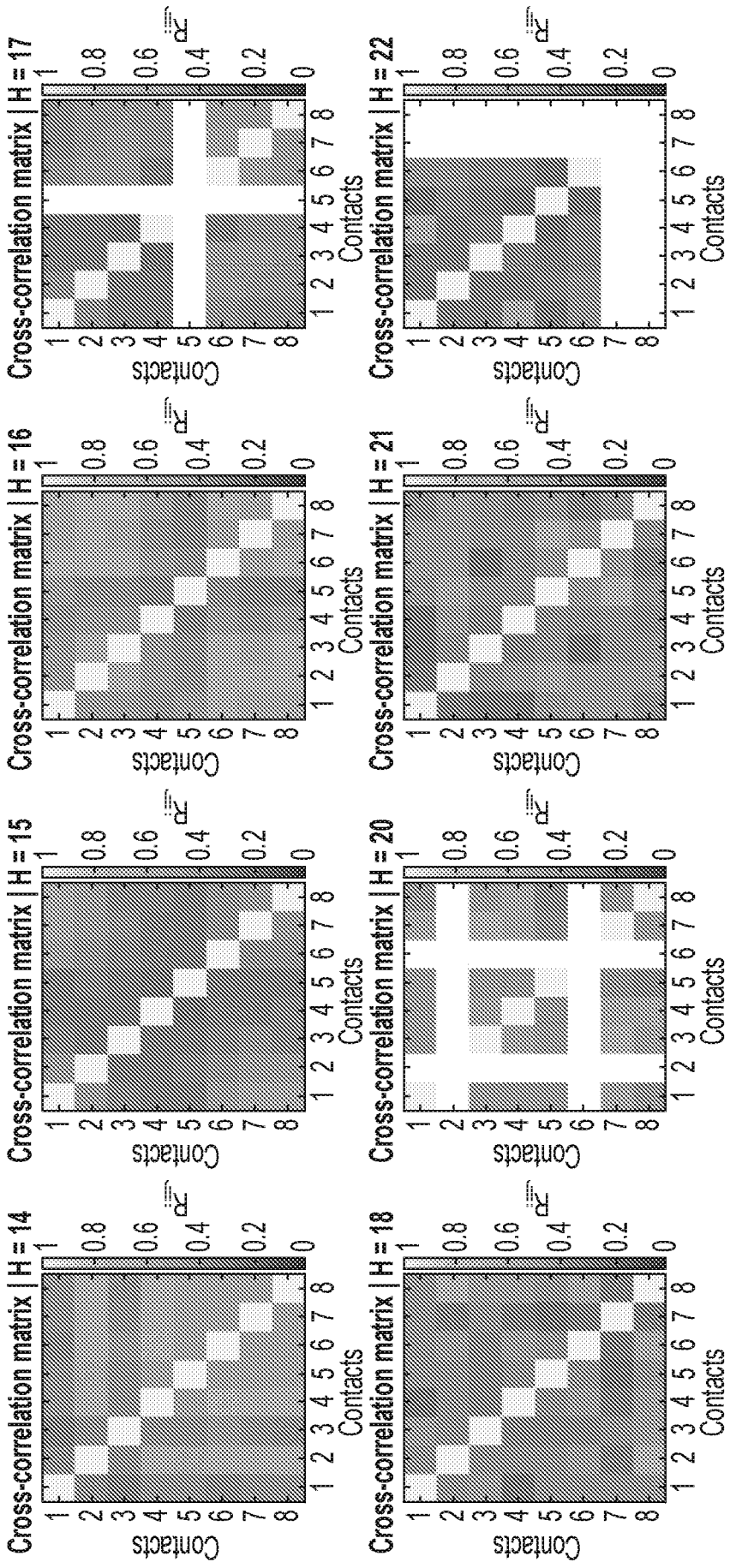
Cross-correlation matrix | H = 14
Cross-correlation matrix | H = 15
Cross-correlation matrix | H = 16
Cross-correlation matrix | H = 17
Cross-correlation matrix | H = 18
Cross-correlation matrix | H = 20
Cross-correlation matrix | H = 21
Cross-correlation matrix | H = 22
Contacts
Contacts
R

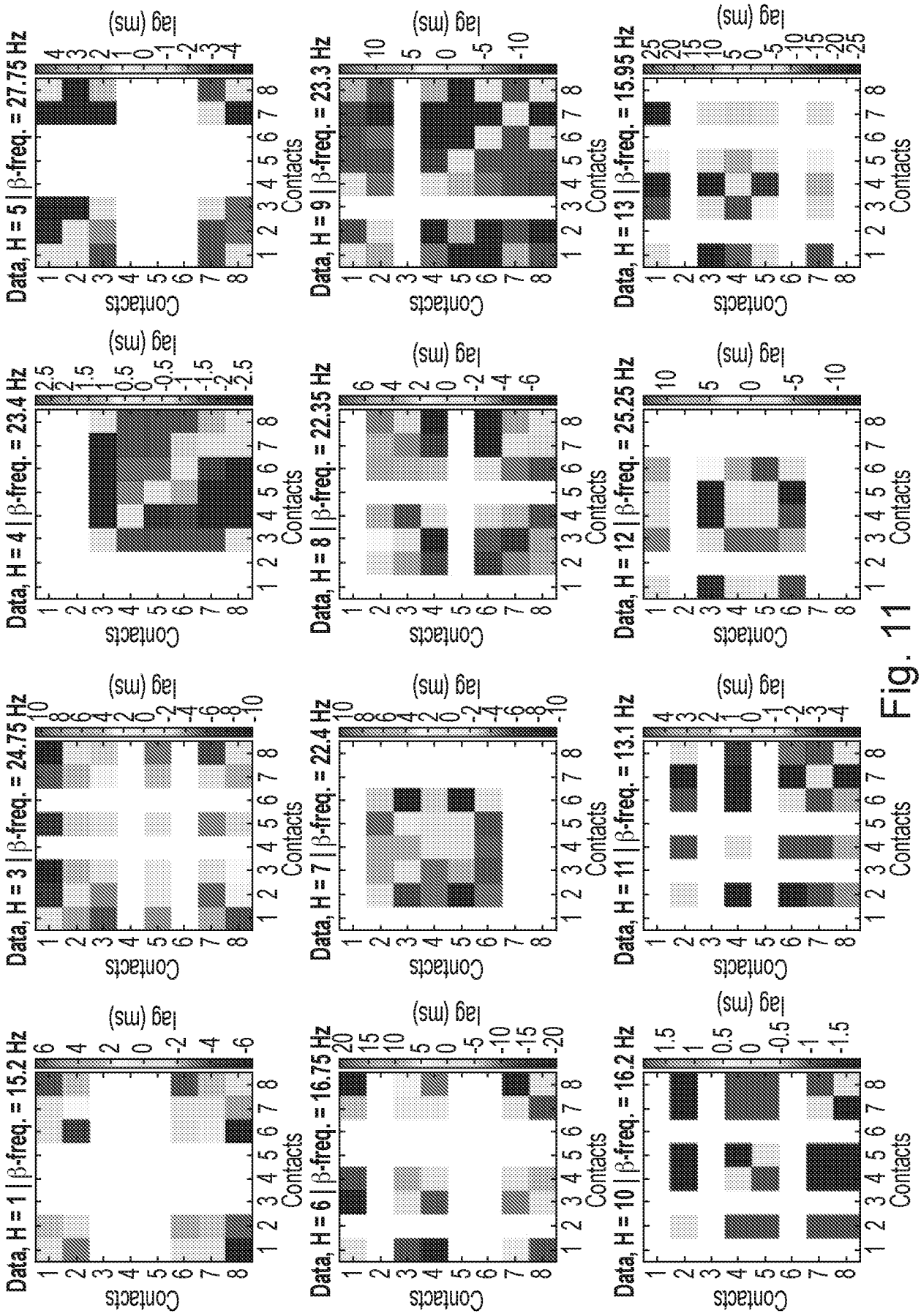
Data, H = 1 | β-freq. = 15.2 Hz
Data, H = 2 | β-freq. = 15.95 Hz
Data, H = 3 | β-freq. = 24.75 Hz
Data, H = 4 | β-freq. = 23.4 Hz
Data, H = 5 | β-freq. = 27.75 Hz
Data, H = 6 | β-freq. = 16.75 Hz
Data, H = 7 | β-freq. = 22.4 Hz
Data, H = 8 | β-freq. = 22.35 Hz
Data, H = 9 | β-freq. = 23.3 Hz
Data, H = 10 | β-freq. = 16.2 Hz
Data, H = 11 | β-freq. = 13.1 Hz
Data, H = 12 | β-freq. = 25.25 Hz
Data, H = 13 | β-freq. = 15.95 Hz
Contacts
Contacts
lag (ms)

Fig. 11

Fig. 11 (Cont.)

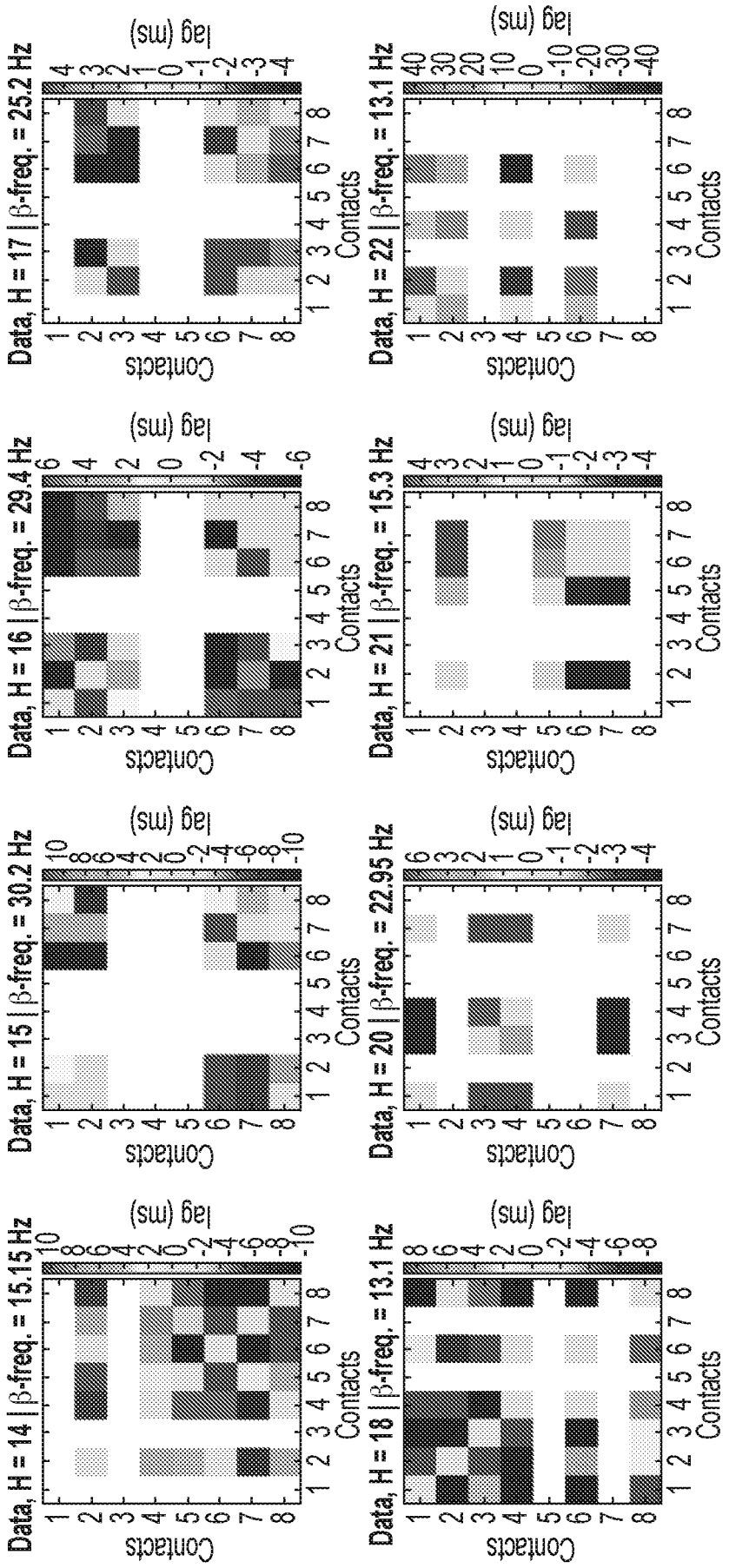
Data, H = 17 | β-freq. = 25.2 Hz
Data, H = 22 | β-freq. = 13.1 Hz
Data, H = 16 | β-freq. = 29.4 Hz
Data, H = 21 | β-freq. = 15.3 Hz
Data, H = 15 | β-freq. = 30.2 Hz
Data, H = 20 | β-freq. = 22.95 Hz
Data, H = 14 | β-freq. = 15.15 Hz
Data, H = 18 | β-freq. = 13.1 Hz
Contacts
lag (ms)

Fig. 12A

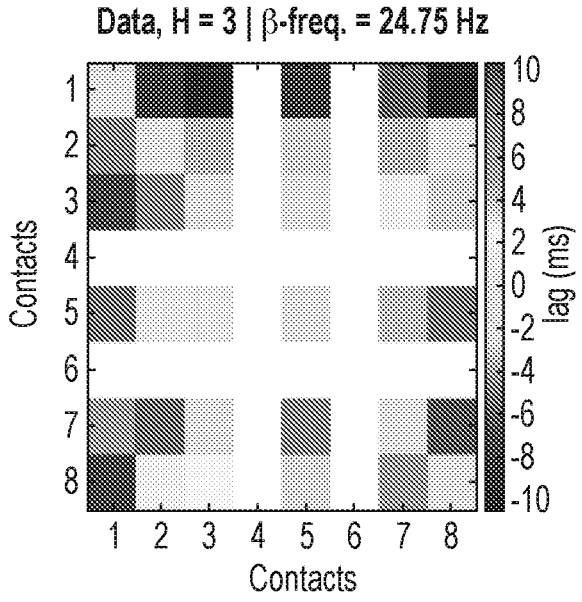


Fig. 12B

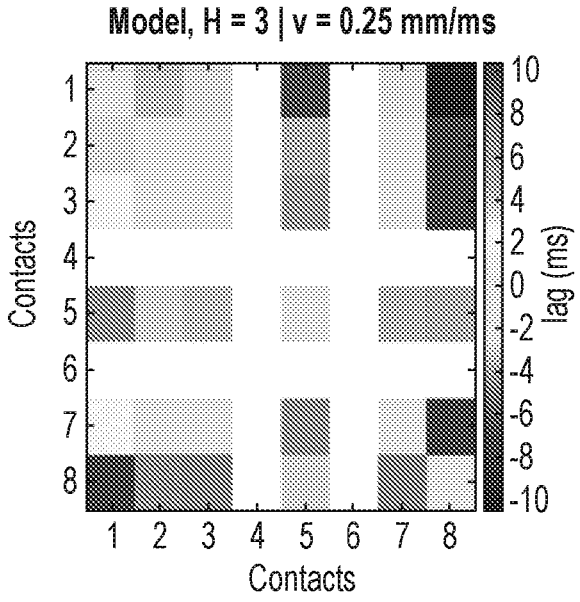


Fig. 12C

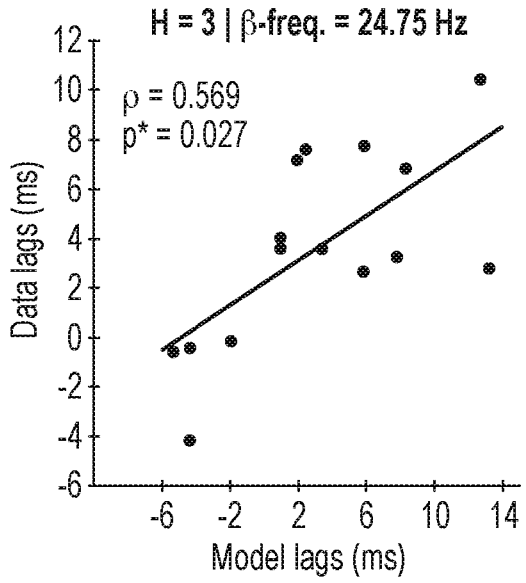


Fig. 12D

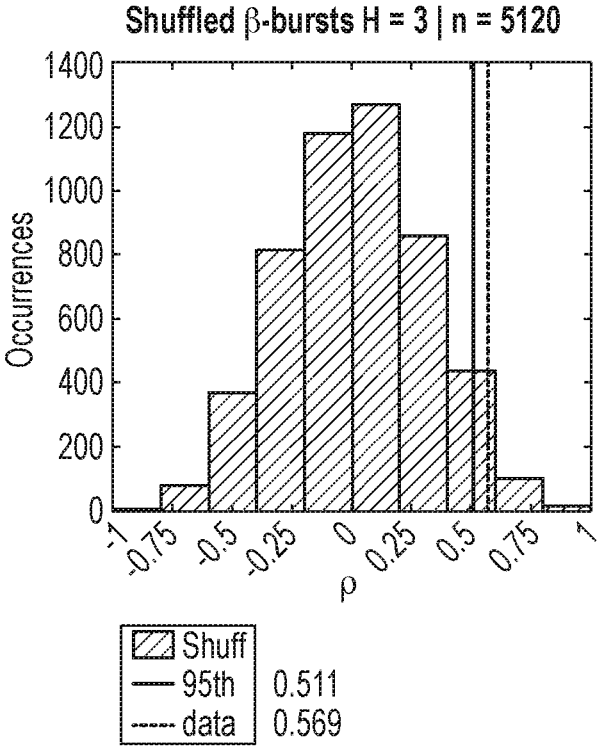

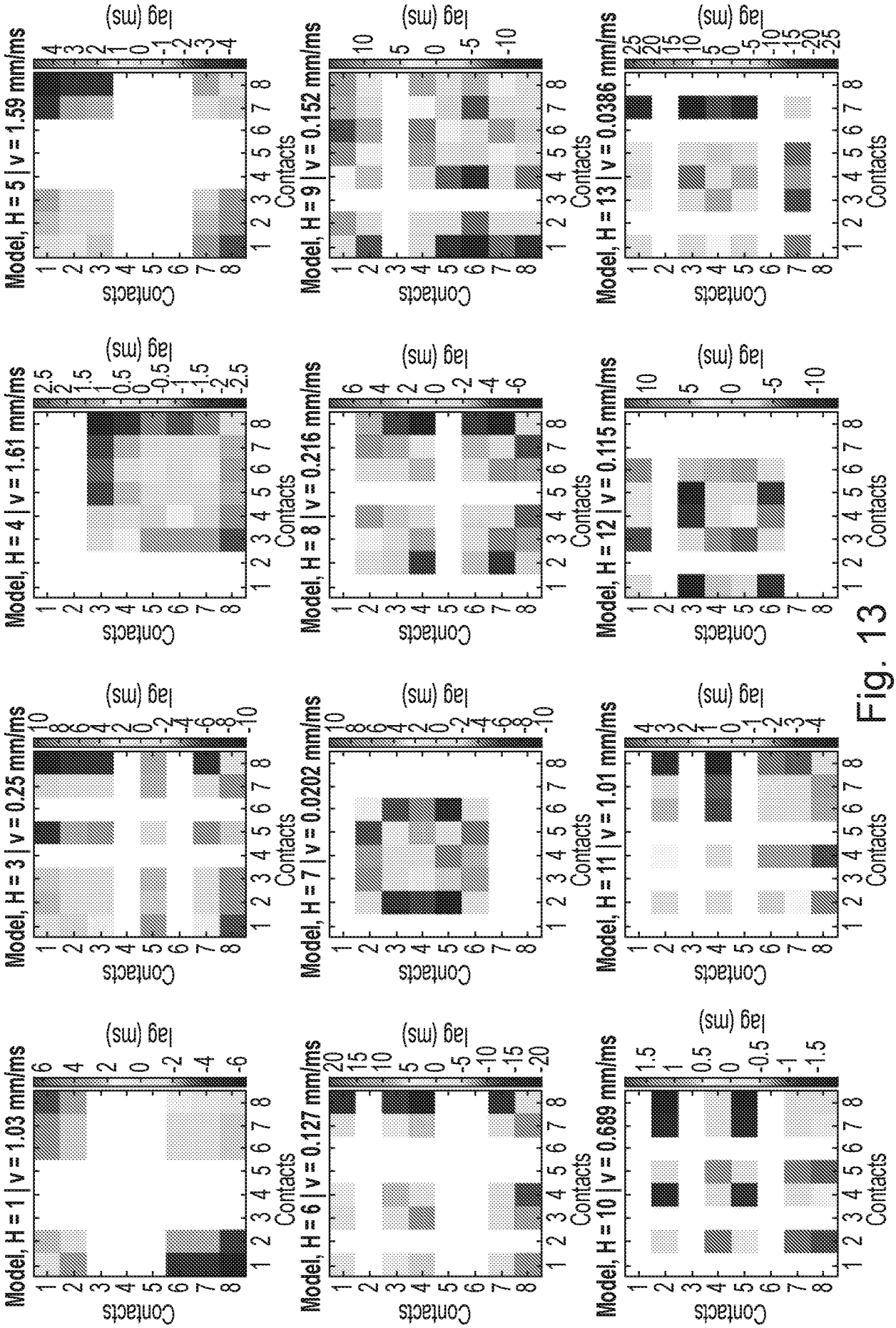
Model, H = 1 | v = 1.03 mm/ms
Model, H = 2 | v = 1.59 mm/ms
Model, H = 3 | v = 0.25 mm/ms
Model, H = 4 | v = 1.61 mm/ms
Model, H = 5 | v = 1.59 mm/ms
Model, H = 6 | v = 0.127 mm/ms
Model, H = 7 | v = 0.0202 mm/ms
Model, H = 8 | v = 0.216 mm/ms
Model, H = 9 | v = 0.152 mm/ms
Model, H = 10 | v = 0.689 mm/ms
Model, H = 11 | v = 1.01 mm/ms
Model, H = 12 | v = 0.115 mm/ms
Model, H = 13 | v = 0.0386 mm/ms
Contacts
Contacts
lag (ms)

Fig. 13

Fig. 13 (Cont.)

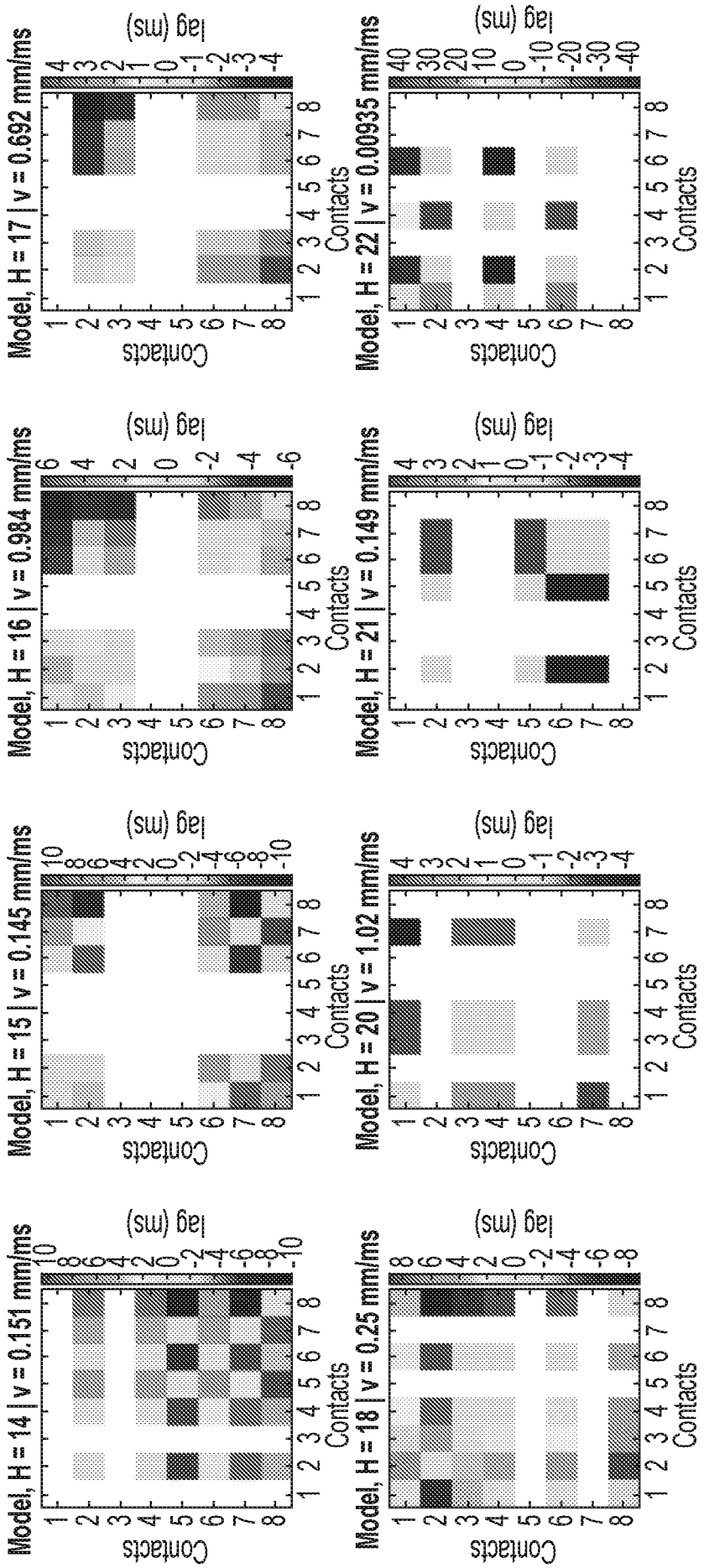
Model, H = 14 | v = 0.151 mm/ms
Model, H = 15 | v = 0.145 mm/ms
Model, H = 16 | v = 0.984 mm/ms
Model, H = 17 | v = 0.692 mm/ms
Model, H = 18 | v = 0.25 mm/ms
Model, H = 20 | v = 1.02 mm/ms
Model, H = 21 | v = 0.149 mm/ms
Model, H = 22 | v = 0.00935 mm/ms
Contacts
lag (ms)

Fig. 14

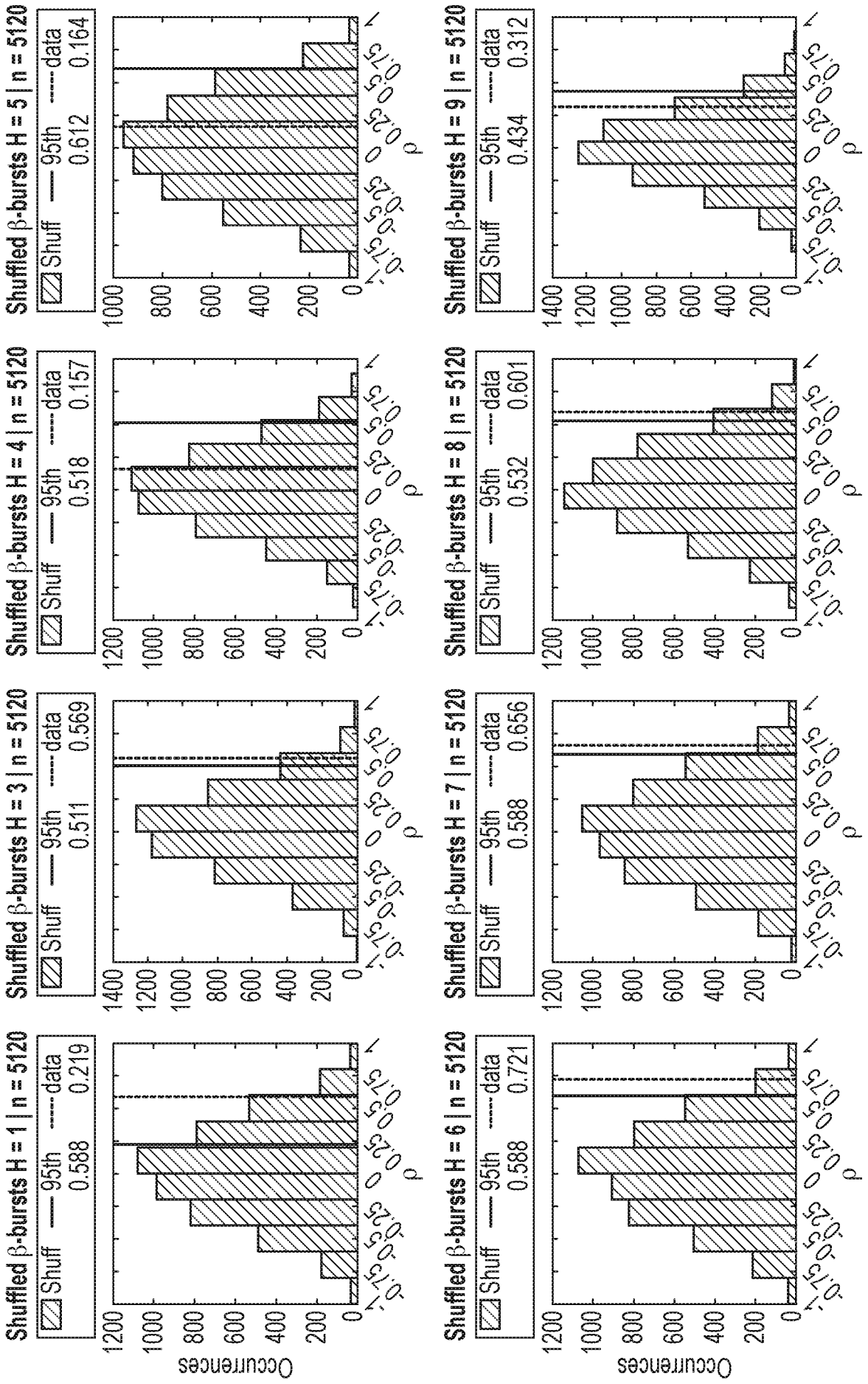
Shuffled β-bursts H = 1 | n = 5120
Shuffled β-bursts H = 3 | n = 5120
Shuffled β-bursts H = 4 | n = 5120
Shuffled β-bursts H = 5 | n = 5120
Shuffled β-bursts H = 6 | n = 5120
Shuffled β-bursts H = 7 | n = 5120
Shuffled β-bursts H = 8 | n = 5120
Shuffled β-bursts H = 9 | n = 5120
Shuff
95th
data
0.588
0.219
0.511
0.569
0.518
0.157
0.612
0.164
0.588
0.721
0.588
0.656
0.532
0.601
0.434
0.312
Occurrences
ρ

Fig. 14 (Cont. I)

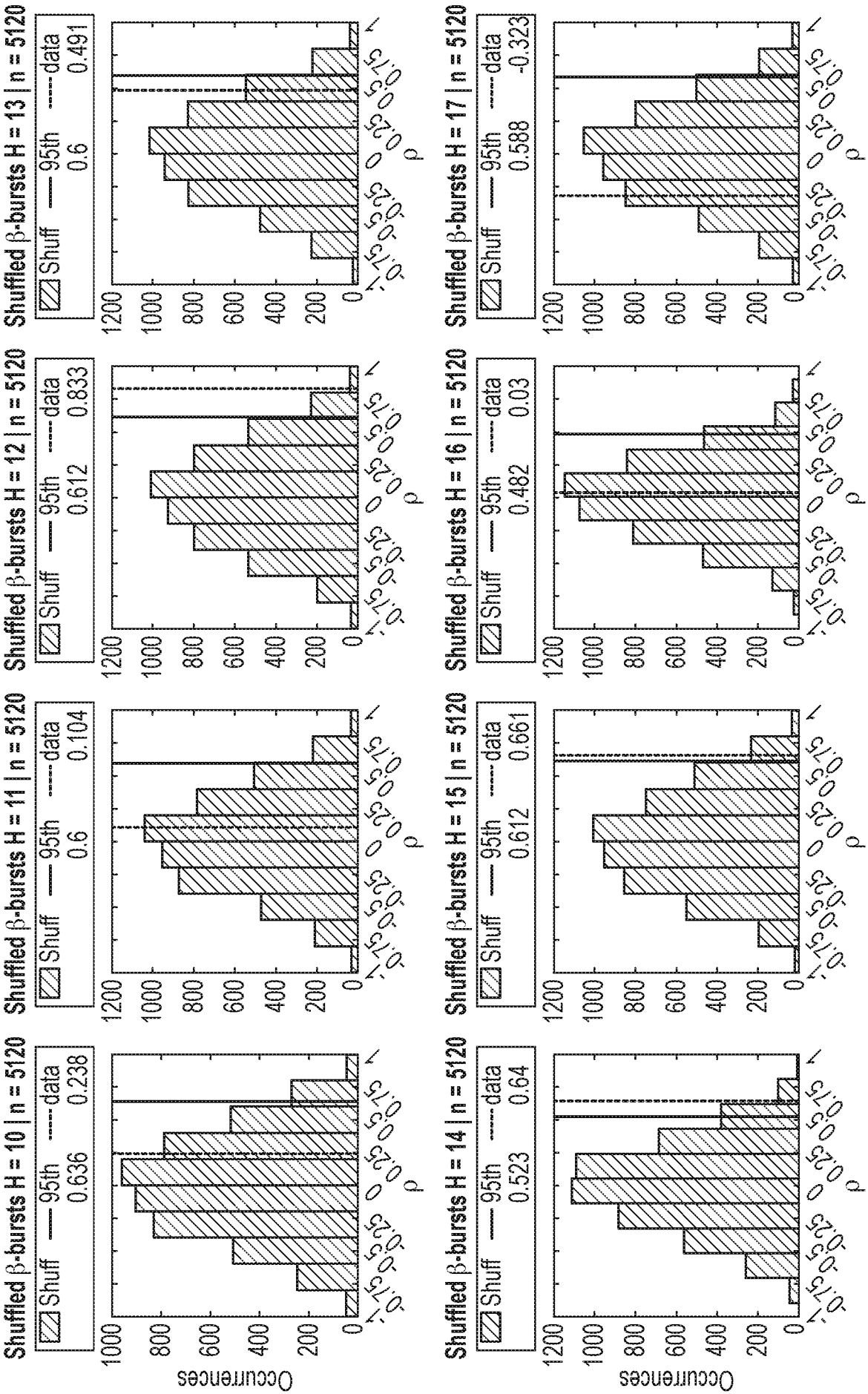
Shuffled β-bursts H = 10 | n = 5120
Shuffled β-bursts H = 11 | n = 5120
Shuffled β-bursts H = 12 | n = 5120
Shuffled β-bursts H = 13 | n = 5120
Shuffled β-bursts H = 14 | n = 5120
Shuffled β-bursts H = 15 | n = 5120
Shuffled β-bursts H = 16 | n = 5120
Shuffled β-bursts H = 17 | n = 5120
Shuff
95th
data
0.636
0.238
0.6
0.104
0.612
0.833
0.6
0.491
0.523
0.64
0.612
0.661
0.482
0.03
0.588
-0.323
Occurrences
ρ

Fig. 14 (Cont. II)

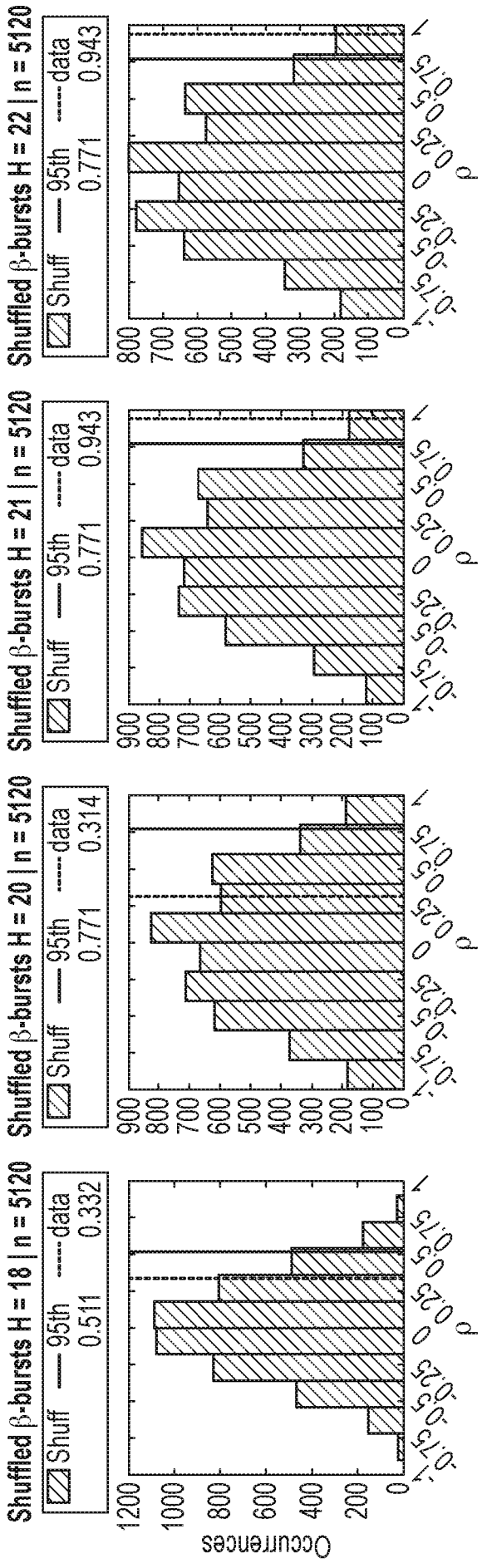

Fig. 15

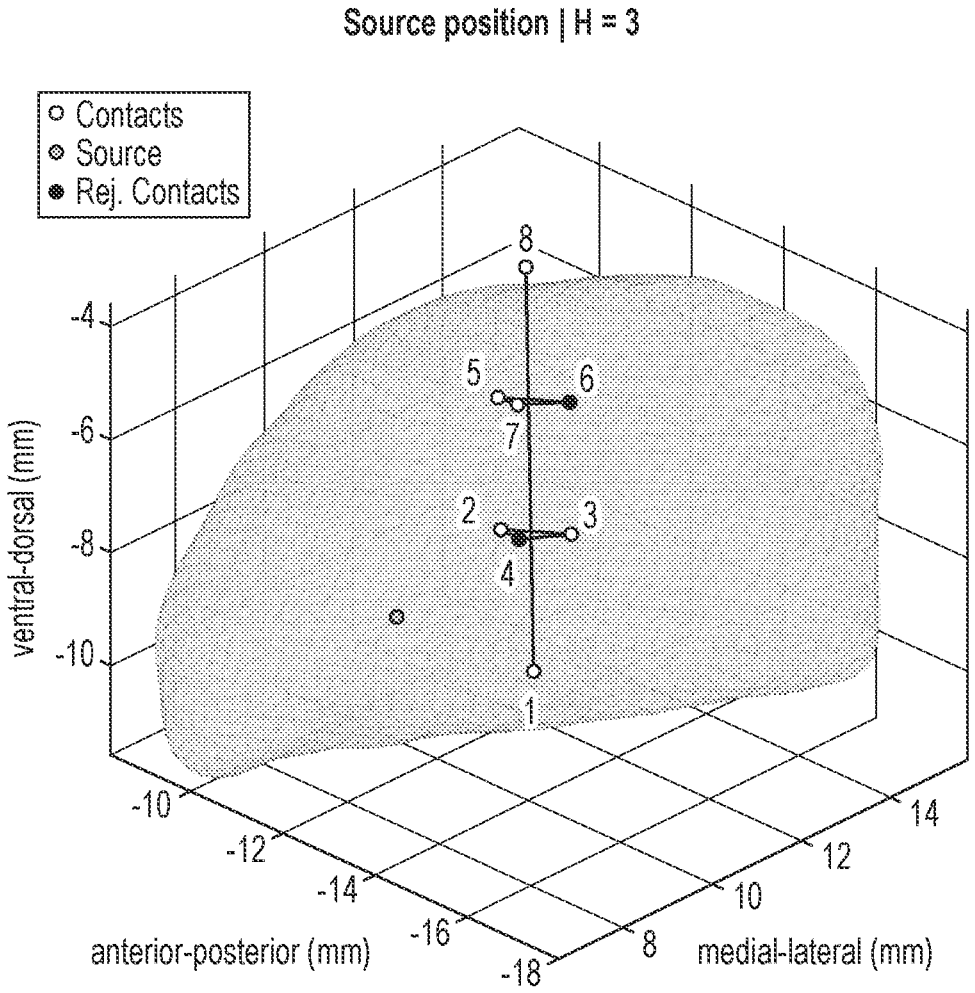
Source position | H = 3
Contacts
Source
Rej. Contacts
8
5
6
7
2
3
4
1
-4
-6
-8
-10
ventral-dorsal (mm)
-10
-12
-14
-16
-18
anterior-posterior (mm)
8
10
12
14
medial-lateral (mm)

Fig. 16

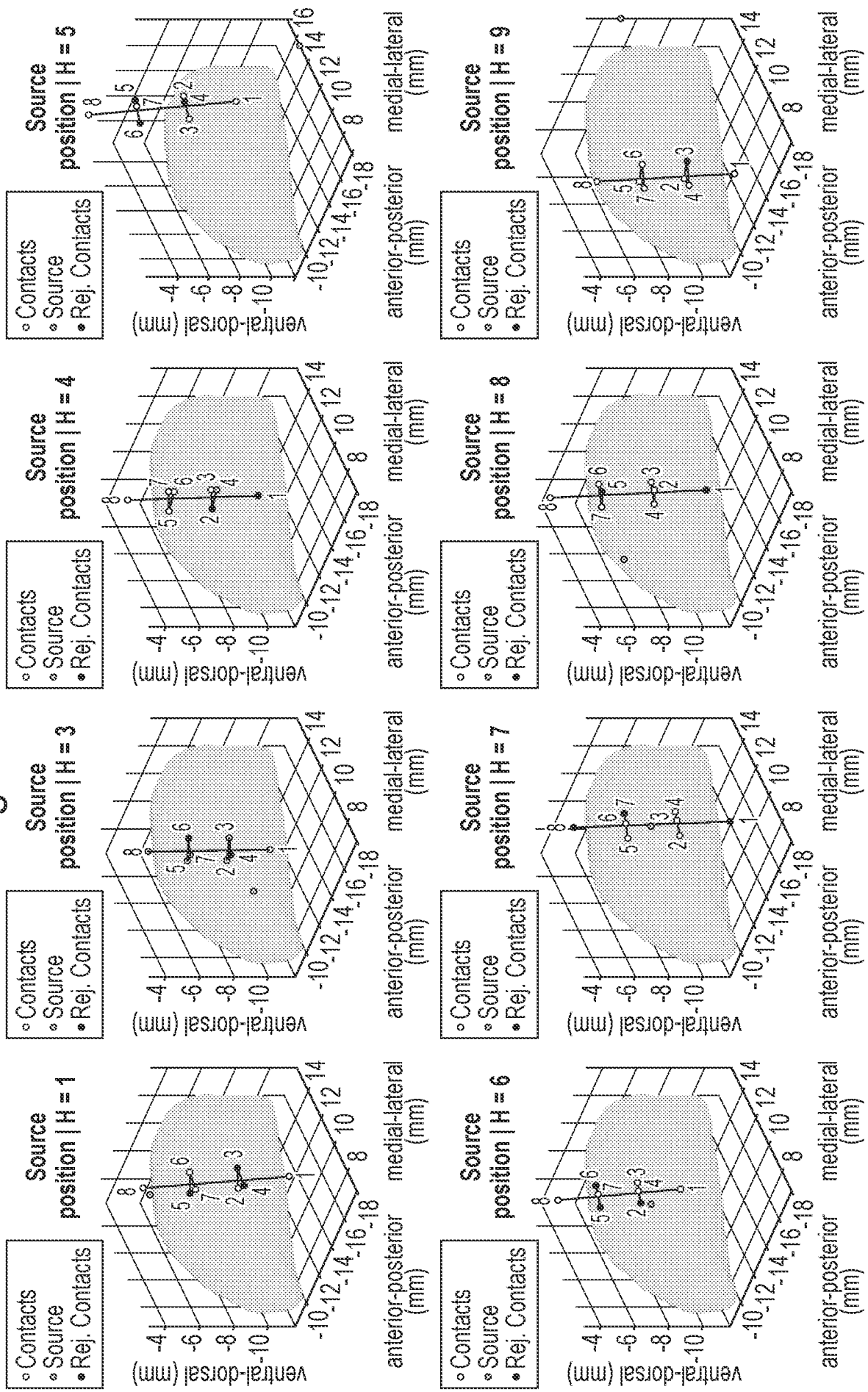
Source position | H = 1
Source position | H = 2
Source position | H = 3
Source position | H = 4
Source position | H = 5
Source position | H = 6
Source position | H = 7
Source position | H = 8
Source position | H = 9
Contacts
Source
Rej. Contacts
ventral-dorsal (mm)
anterior-posterior (mm)
medial-lateral (mm)

Fig. 16 (Cont. I)

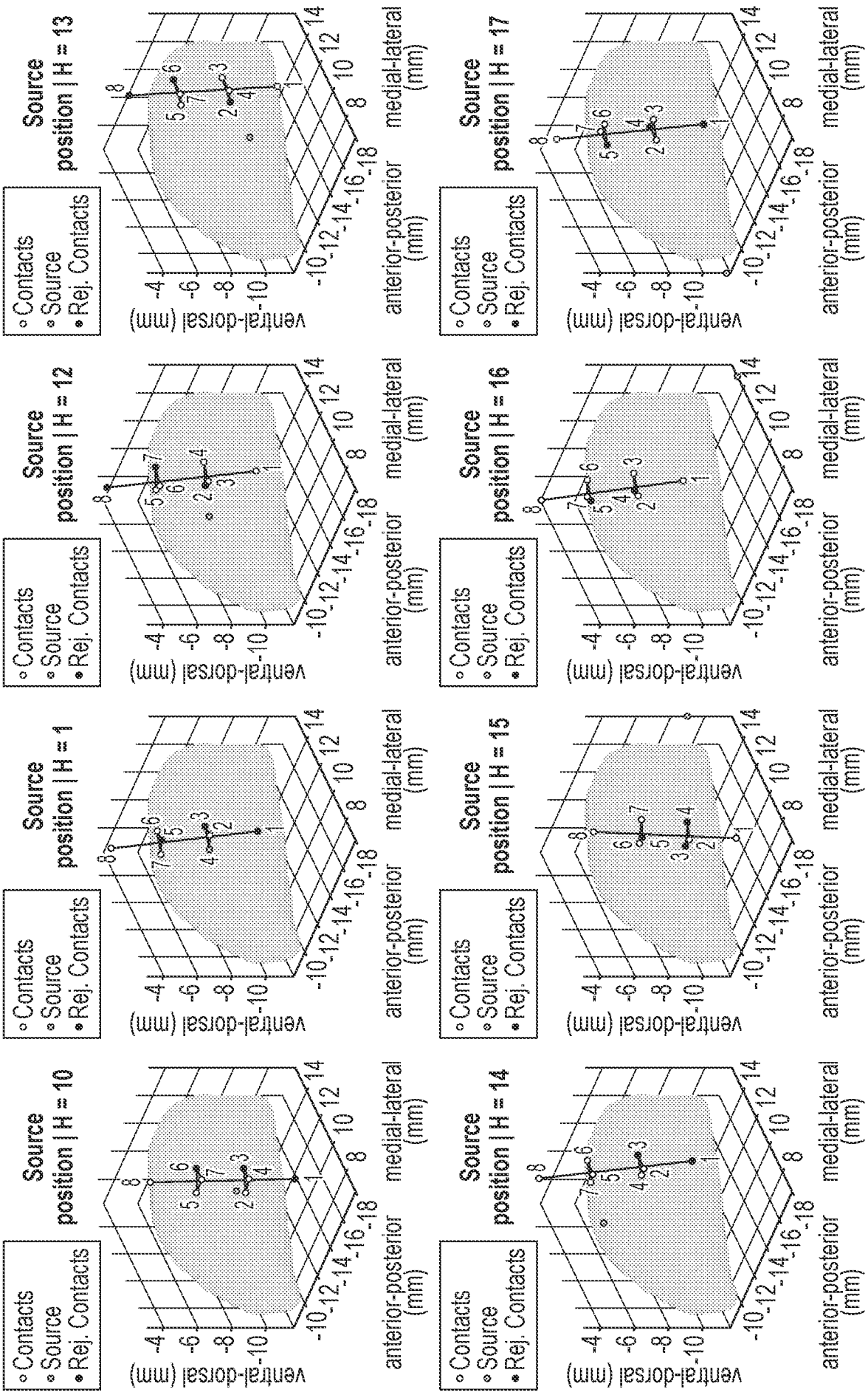
Contacts
Source
Rej. Contacts
Source position | H = 10
Source position | H = 1
Source position | H = 12
Source position | H = 13
Source position | H = 14
Source position | H = 15
Source position | H = 16
Source position | H = 17
ventral-dorsal (mm)
anterior-posterior (mm)
medial-lateral (mm)

Fig. 16 (Cont. II)

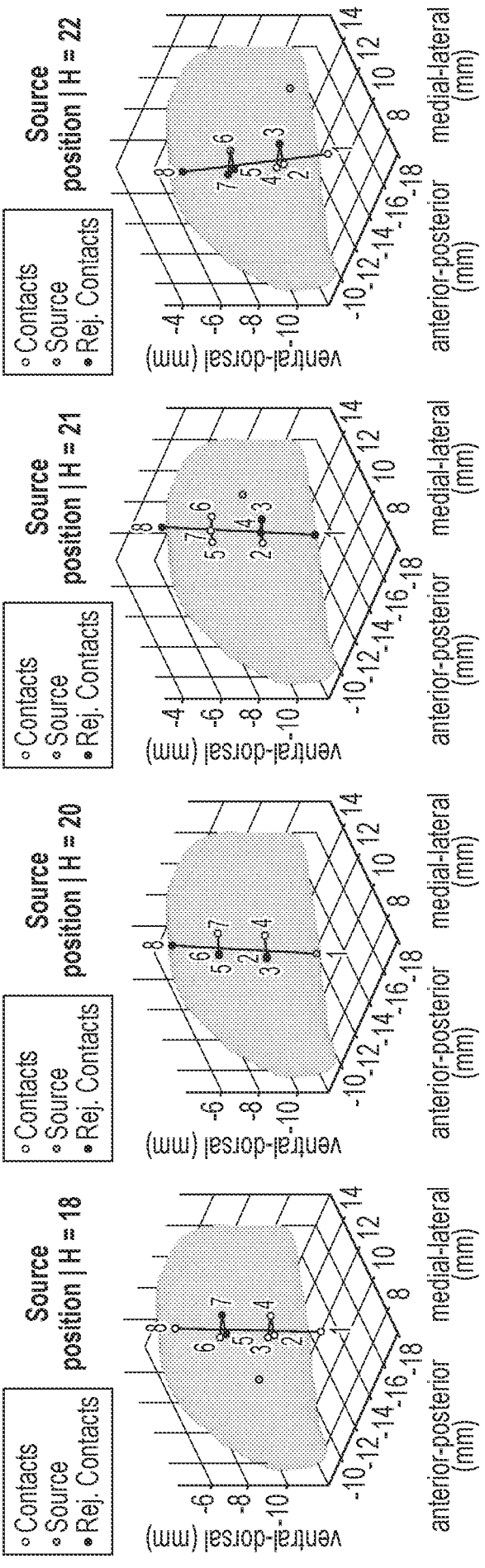

Fig. 17A

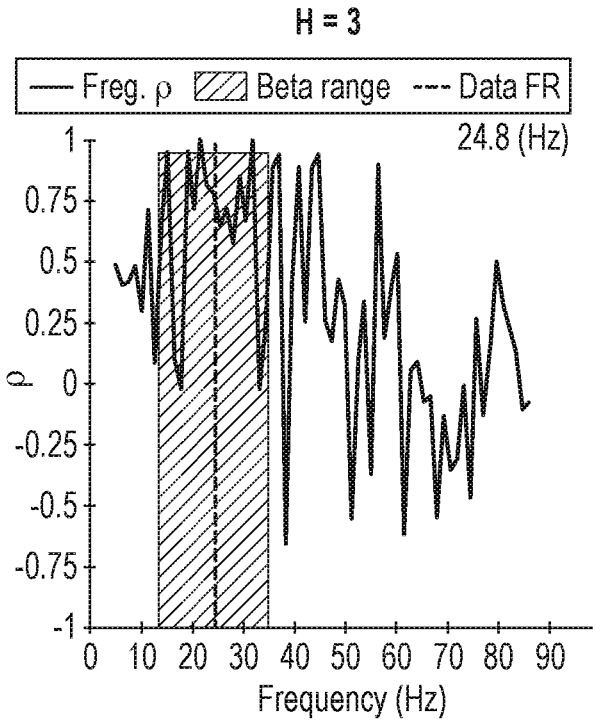


Fig. 17B

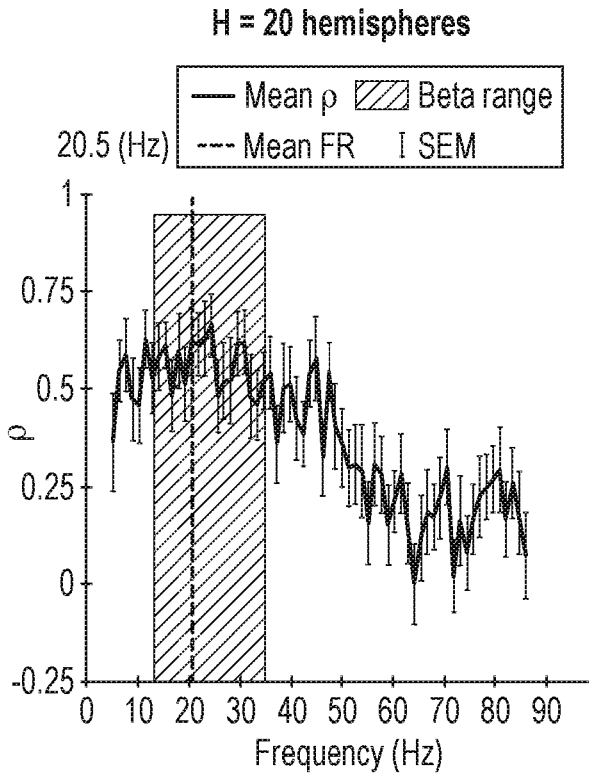


Fig. 17C

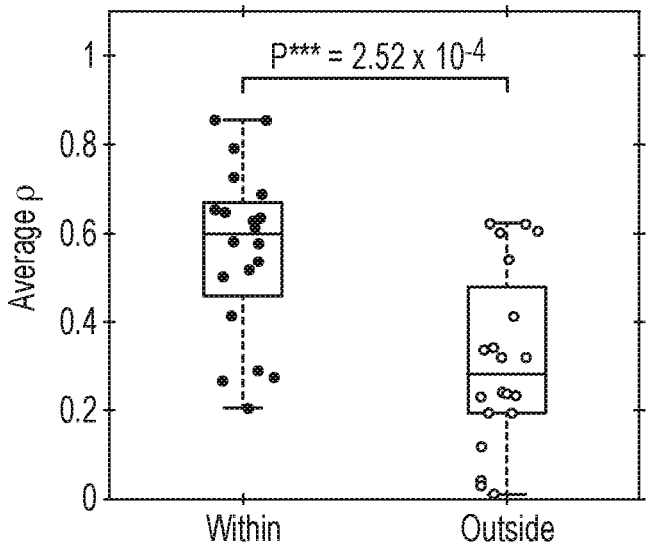

Fig. 18

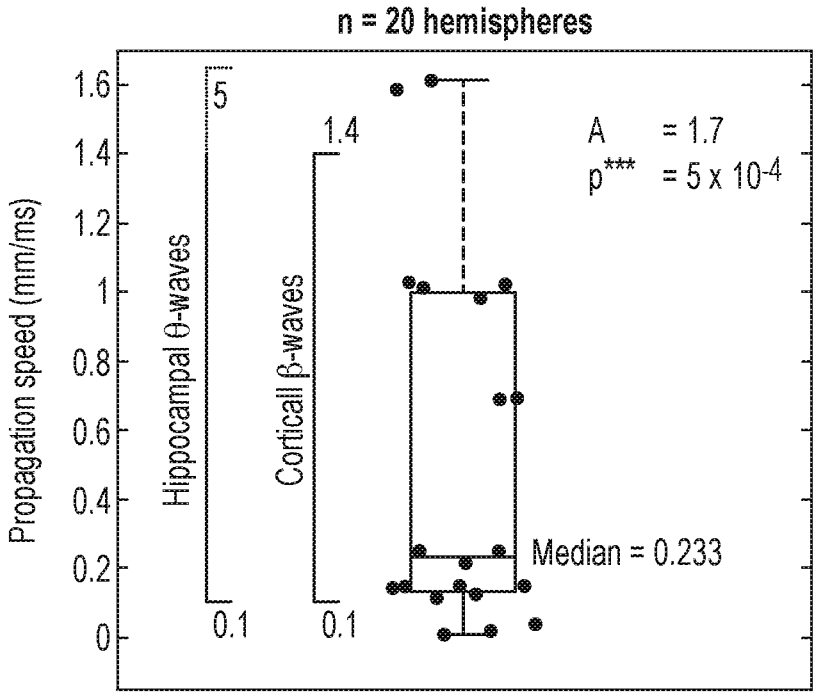
n = 20 hemispheres
Propagation speed (mm/ms)
1.6
1.4
1.2
1
0.8
0.6
0.4
0.2
0
Hippocampal θ-waves
5
0.1
Cortical β-waves
1.4
0.1
A = 1.7
p*** = 5 x 10-4
Median = 0.233

Fig. 19A

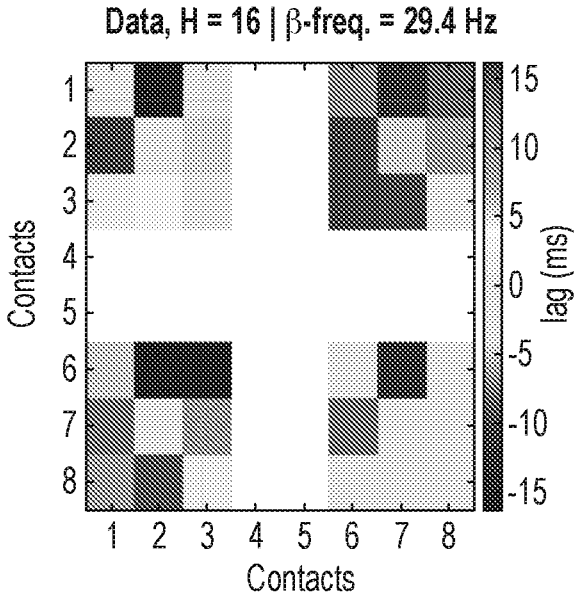


Fig. 19B

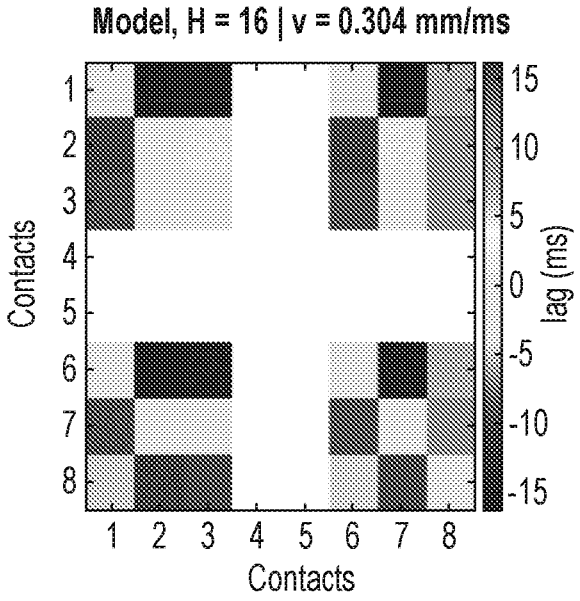


Fig. 19C

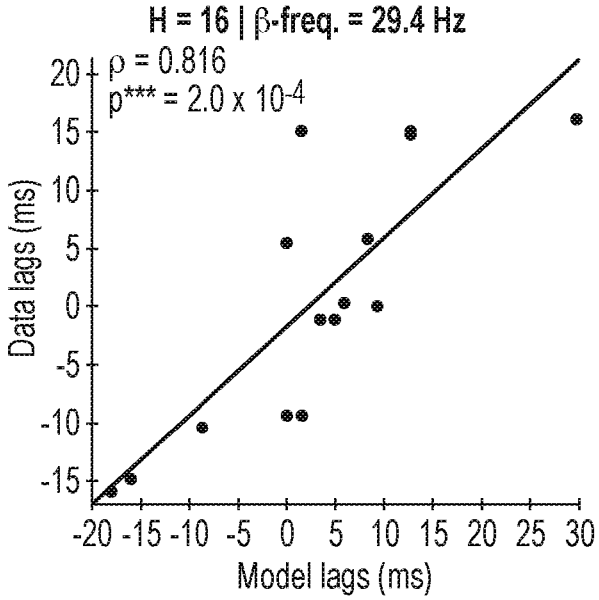


Fig. 19D

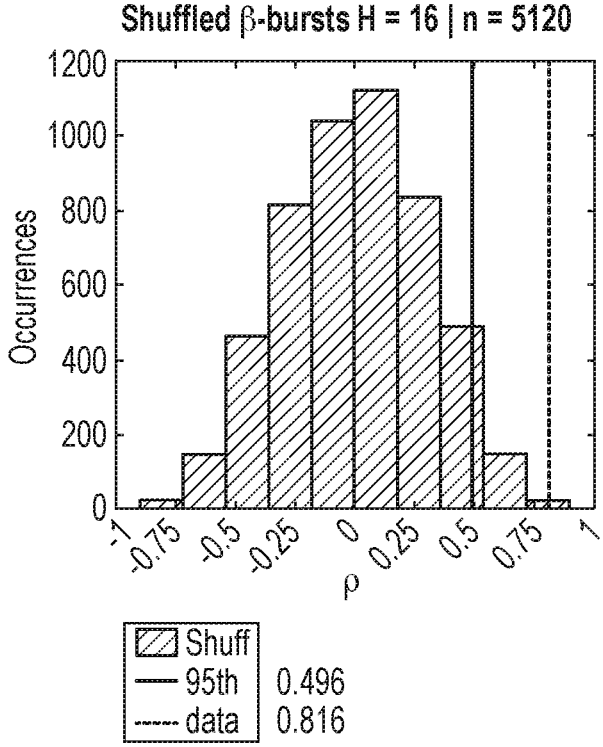

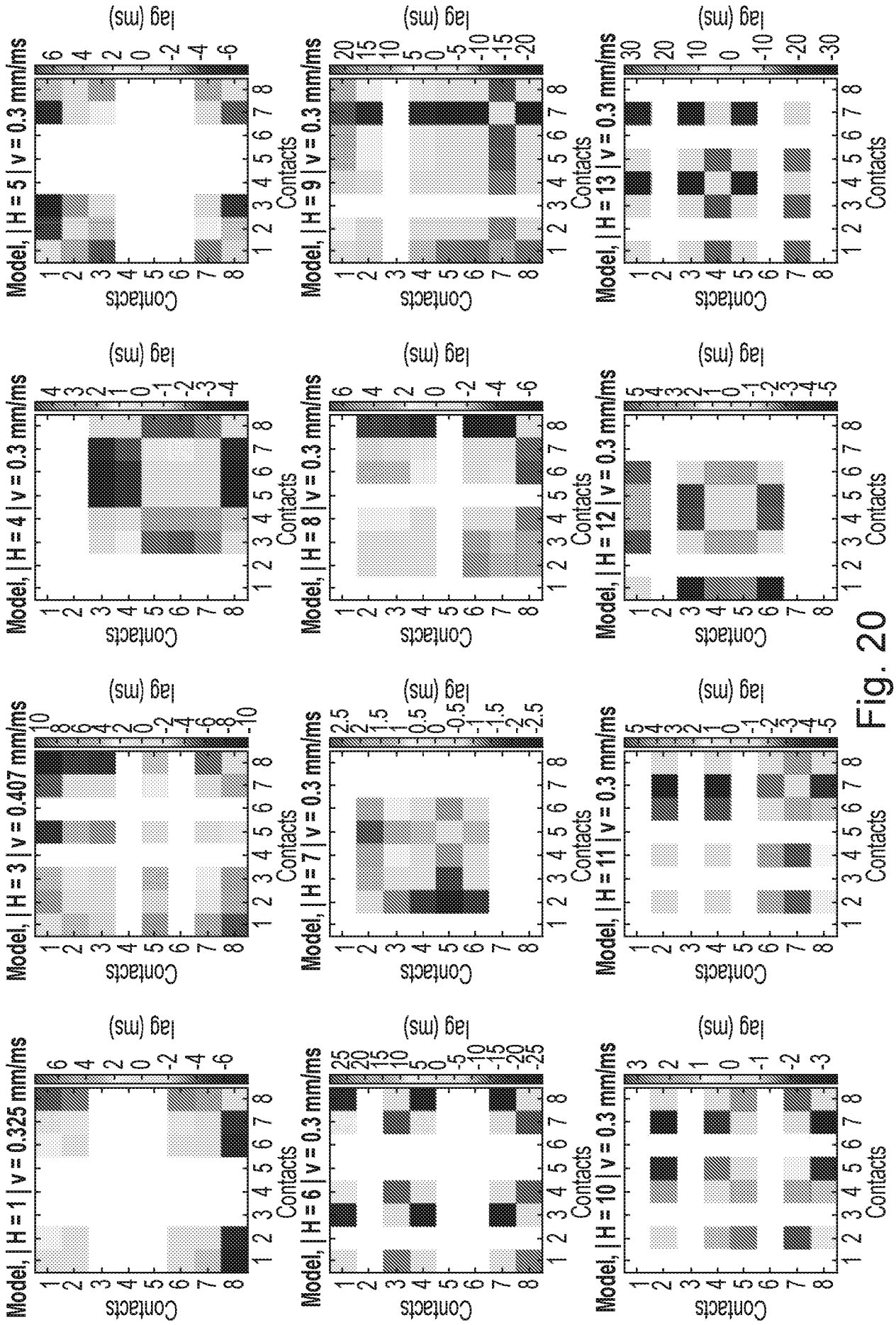
Model, | H = 1 | v = 0.325 mm/ms
Model, | H = 2 | v = 0.3 mm/ms
Model, | H = 3 | v = 0.407 mm/ms
Model, | H = 4 | v = 0.3 mm/ms
Model, | H = 5 | v = 0.3 mm/ms
Model, | H = 6 | v = 0.3 mm/ms
Model, | H = 7 | v = 0.3 mm/ms
Model, | H = 8 | v = 0.3 mm/ms
Model, | H = 9 | v = 0.3 mm/ms
Model, | H = 10 | v = 0.3 mm/ms
Model, | H = 11 | v = 0.3 mm/ms
Model, | H = 12 | v = 0.3 mm/ms
Model, | H = 13 | v = 0.3 mm/ms
Contacts
lag (ms)

Fig. 20

Fig. 20 (Cont.)

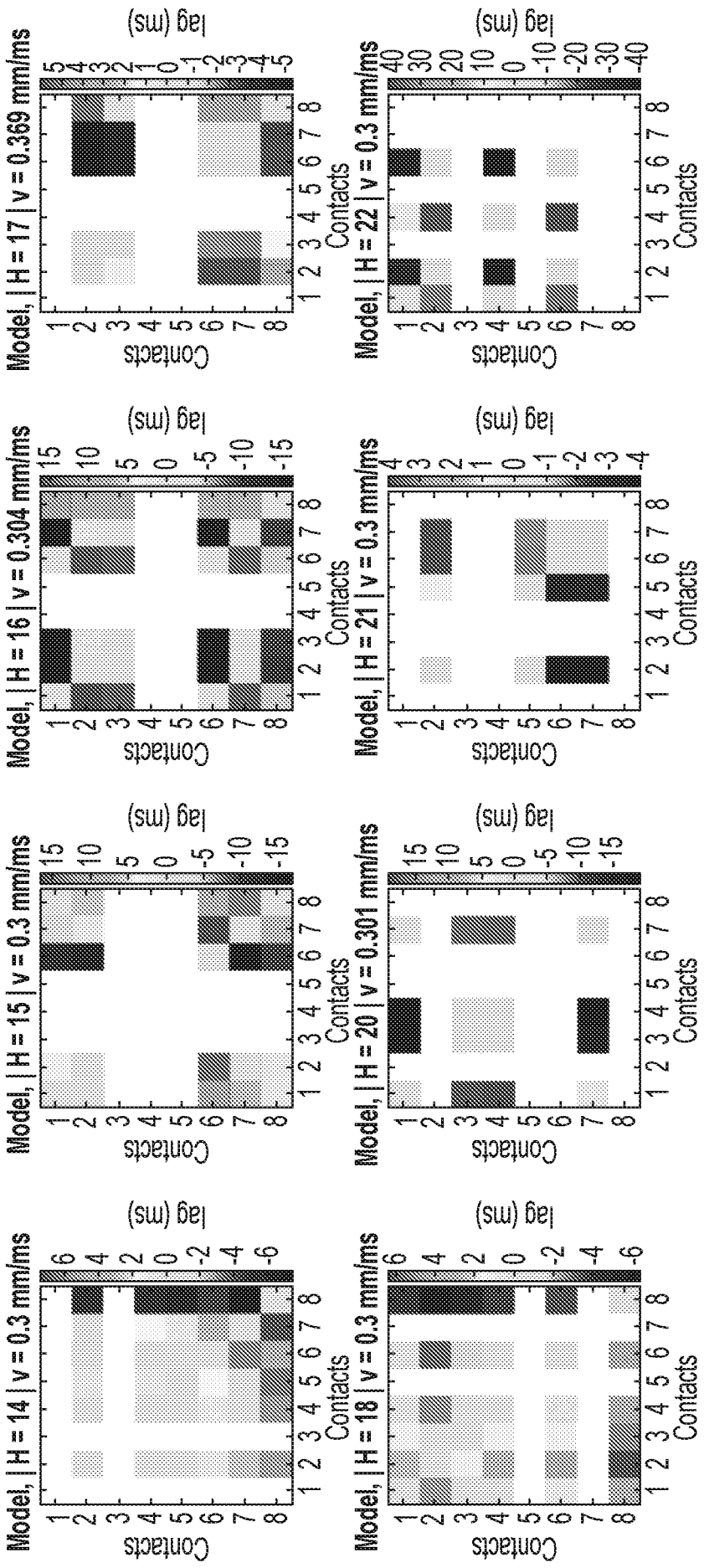
Model, | H = 14 | v = 0.3 mm/ms
Model, | H = 15 | v = 0.3 mm/ms
Model, | H = 16 | v = 0.304 mm/ms
Model, | H = 17 | v = 0.369 mm/ms
Model, | H = 18 | v = 0.3 mm/ms
Model, | H = 20 | v = 0.301 mm/ms
Model, | H = 21 | v = 0.3 mm/ms
Model, | H = 22 | v = 0.3 mm/ms
Contacts
Lag (ms)

Fig. 21

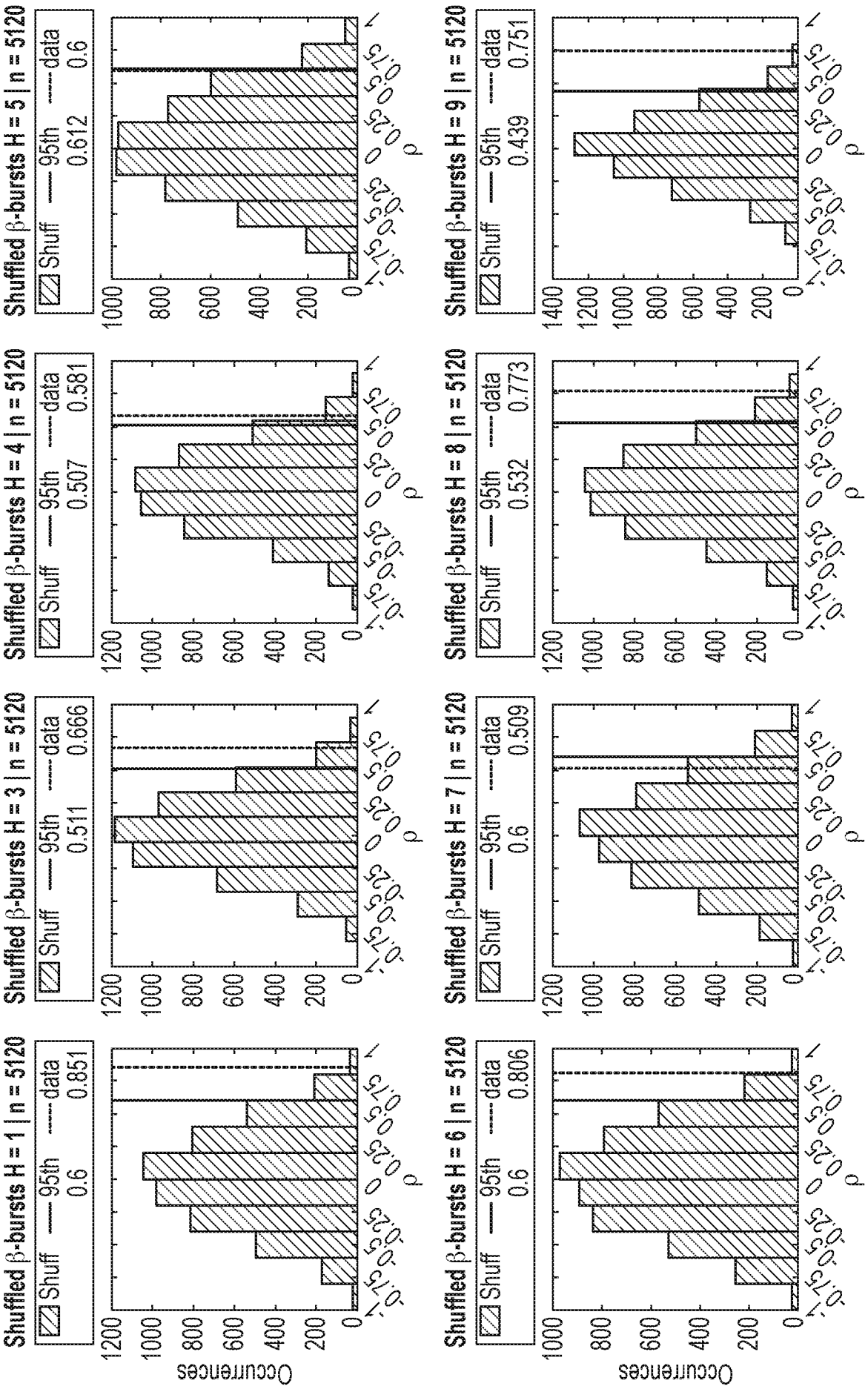
Shuffled β-bursts H = 1 | n = 5120
Shuffled β-bursts H = 3 | n = 5120
Shuffled β-bursts H = 4 | n = 5120
Shuffled β-bursts H = 5 | n = 5120
Shuffled β-bursts H = 6 | n = 5120
Shuffled β-bursts H = 7 | n = 5120
Shuffled β-bursts H = 8 | n = 5120
Shuffled β-bursts H = 9 | n = 5120
Shuff
95th
data
0.6
0.851
0.511
0.666
0.507
0.581
0.612
0.6
0.6
0.806
0.6
0.509
0.532
0.773
0.439
0.751
Occurrences
ρ

Fig. 21 (Cont. I)

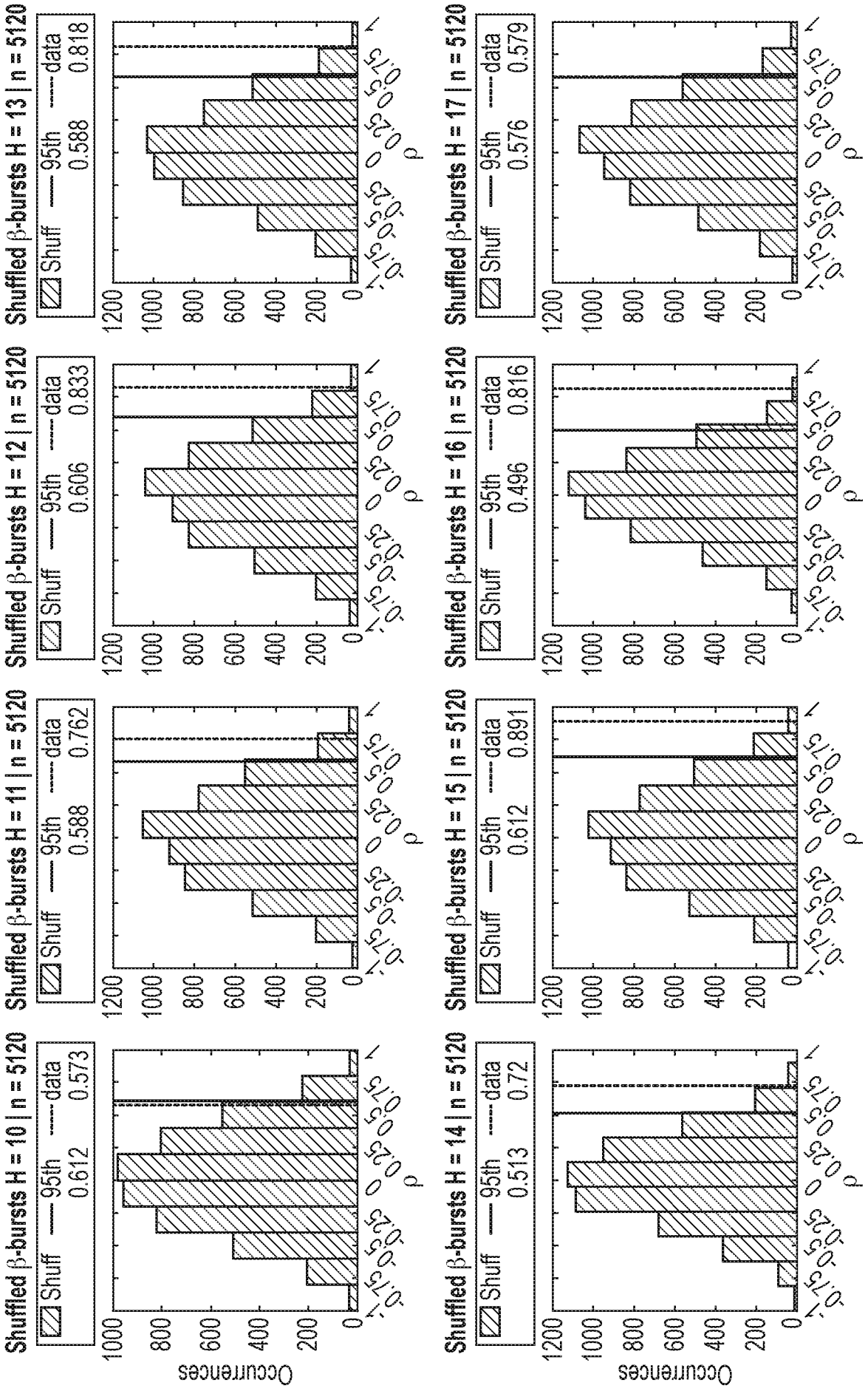
Shuffled β-bursts H = 10 | n = 5120
Shuffled β-bursts H = 11 | n = 5120
Shuffled β-bursts H = 12 | n = 5120
Shuffled β-bursts H = 13 | n = 5120
Shuffled β-bursts H = 14 | n = 5120
Shuffled β-bursts H = 15 | n = 5120
Shuffled β-bursts H = 16 | n = 5120
Shuffled β-bursts H = 17 | n = 5120
Shuff
95th
data
0.612
0.573
0.588
0.762
0.606
0.833
0.588
0.818
0.513
0.72
0.612
0.891
0.496
0.816
0.576
0.579
Occurrences
ρ

Fig. 21 (Cont. II)

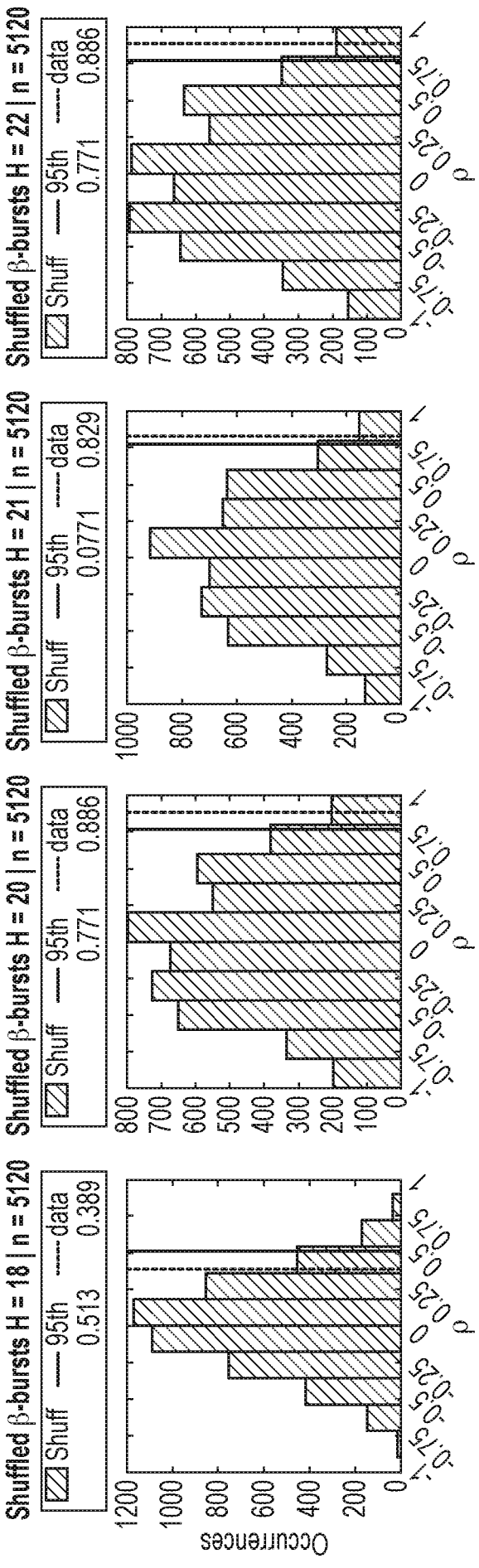

Fig. 22

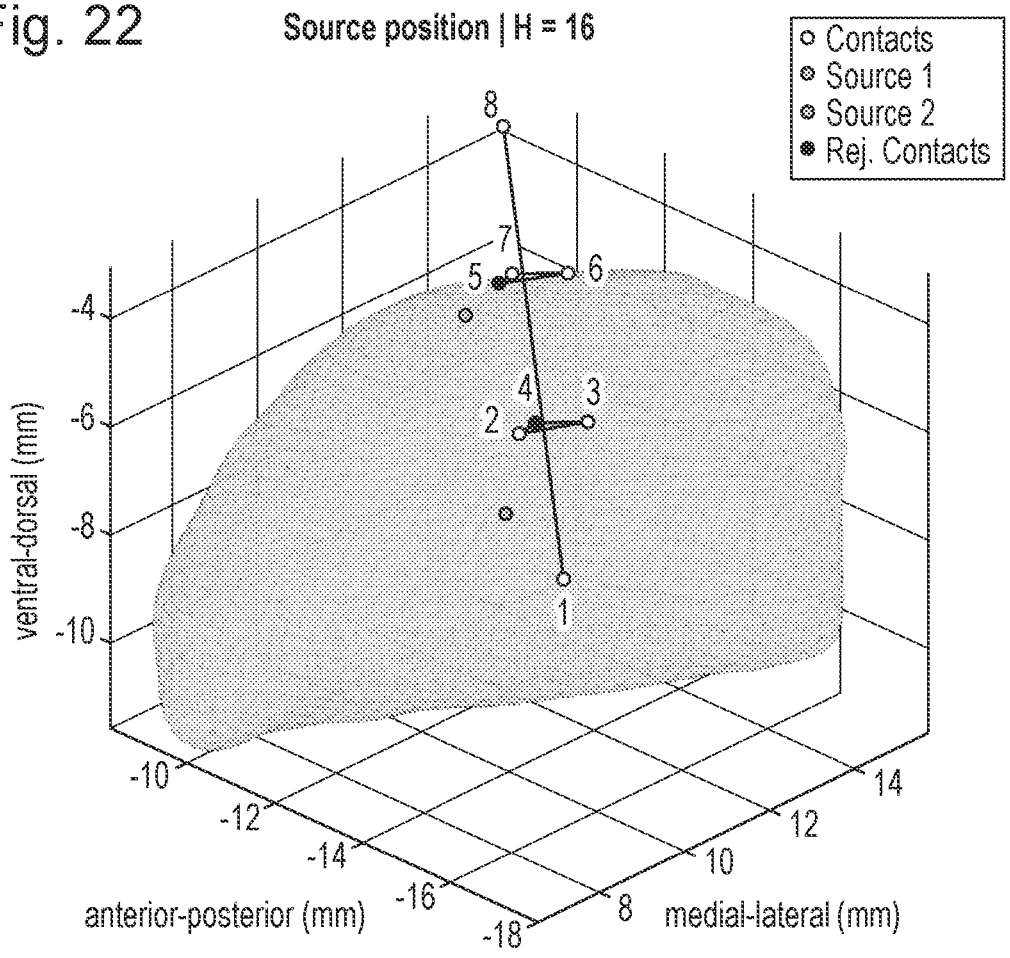
Source position | H = 16
Contacts
Source 1
Source 2
Rej. Contacts
ventral-dorsal (mm)
-4
-6
-8
-10
anterior-posterior (mm)
-10
-12
-14
-16
-18
medial-lateral (mm)
8
10
12
14
1
2
3
4
5
6
7
8

Fig. 23

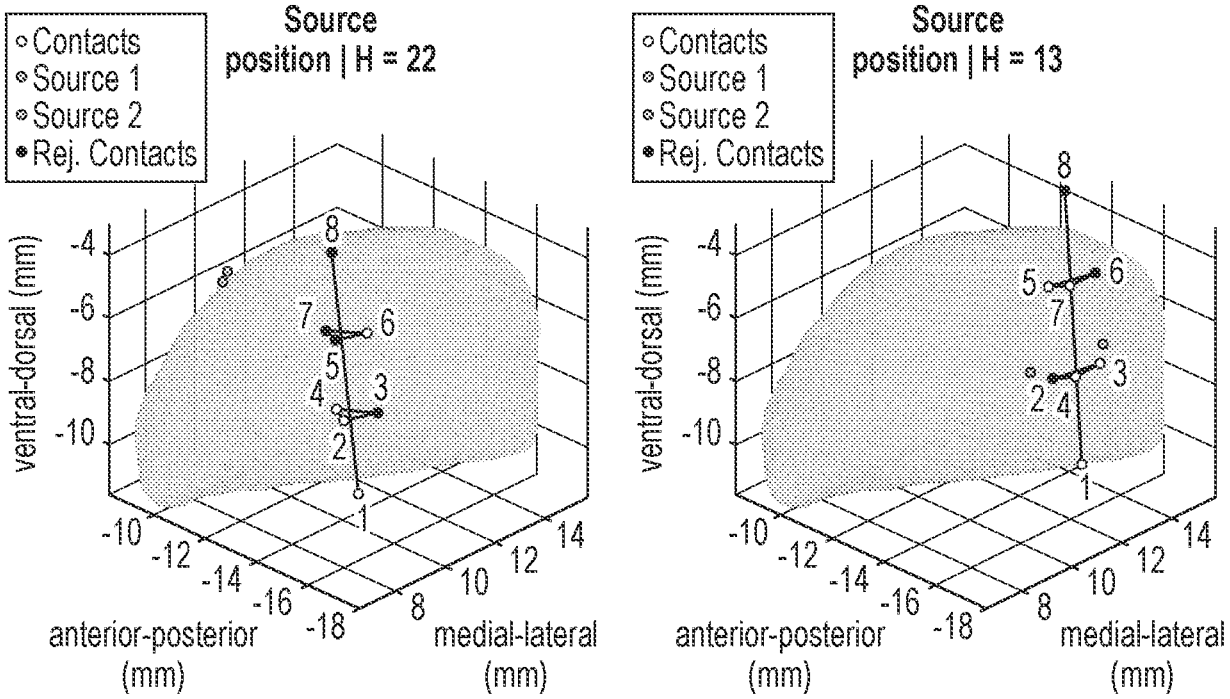
Source position | H = 22
Contacts
Source 1
Source 2
Rej. Contacts
ventral-dorsal (mm)
anterior-posterior (mm)
medial-lateral (mm)
Source position | H = 13
Contacts
Source 1
Source 2
Rej. Contacts
ventral-dorsal (mm)
anterior-posterior (mm)
medial-lateral (mm)

Fig. 24

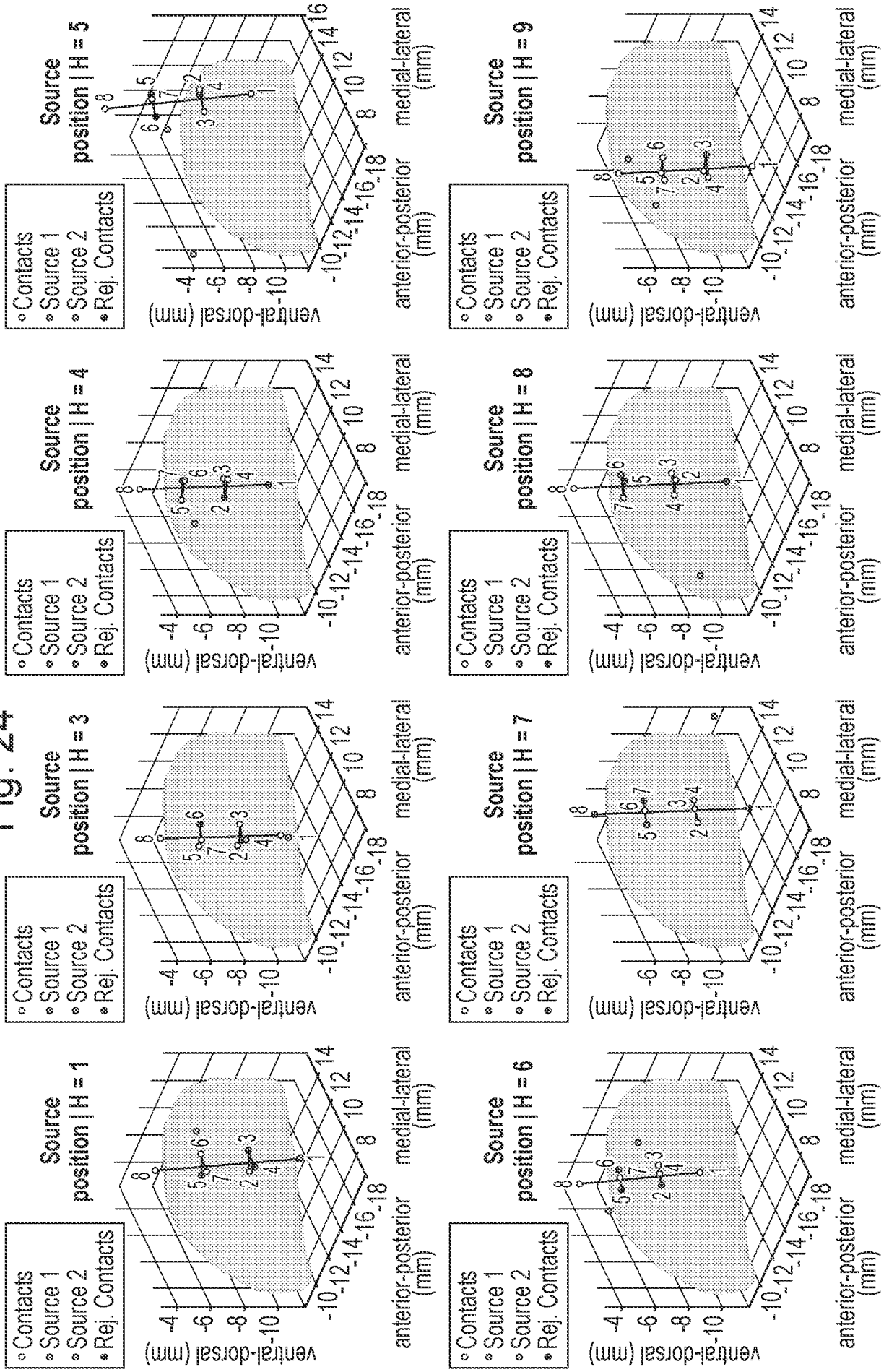
Source position | H = 1
Source position | H = 2
Source position | H = 3
Source position | H = 4
Source position | H = 5
Source position | H = 6
Source position | H = 7
Source position | H = 8
Source position | H = 9
Contacts
Source 1
Source 2
Rej. Contacts
ventral-dorsal (mm)
anterior-posterior (mm)
medial-lateral (mm)

Fig. 24 (Cont. I)

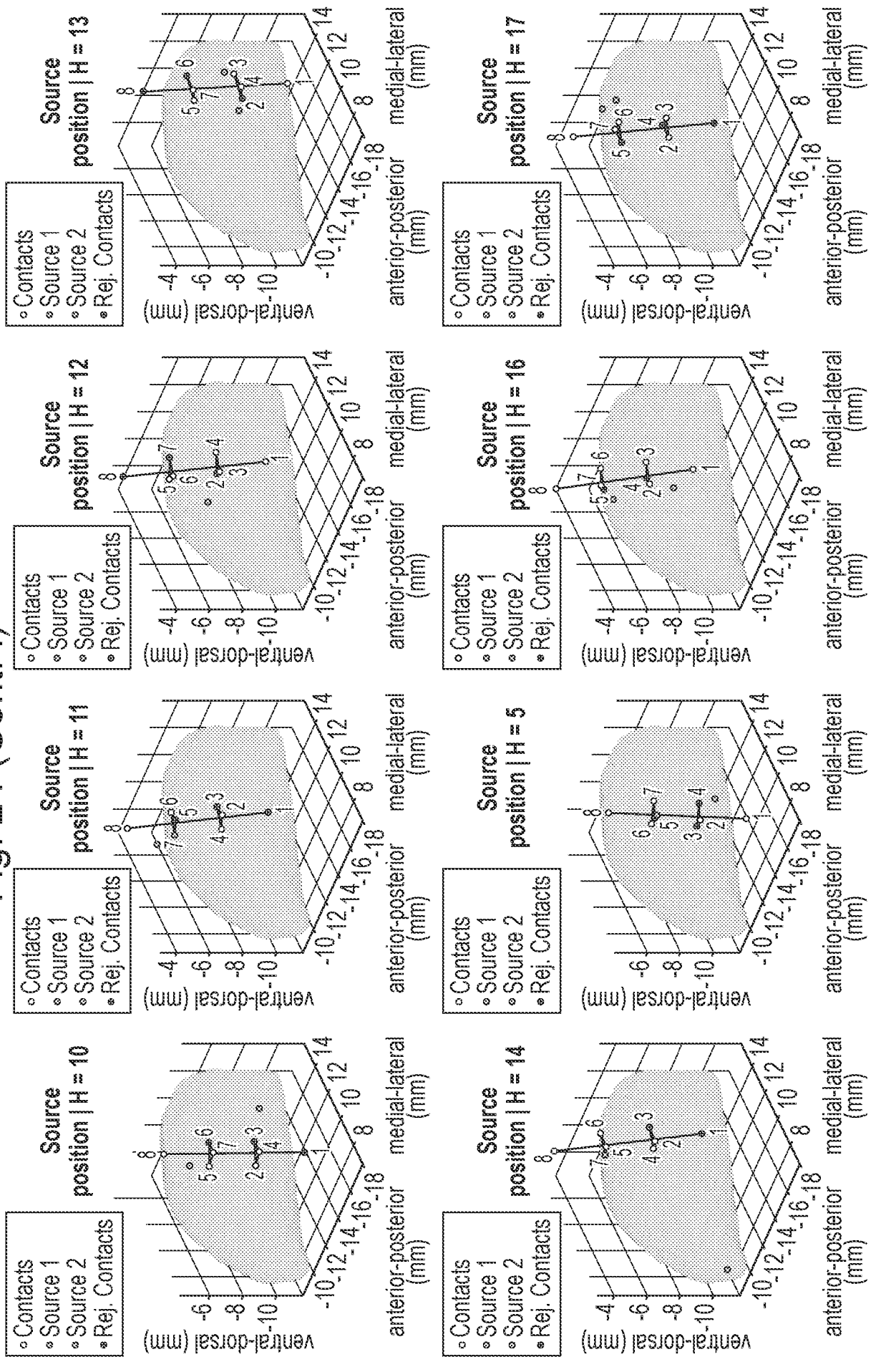
Contacts
Source 1
Source 2
Rej. Contacts
Source position | H = 10
Source position | H = 11
Source position | H = 12
Source position | H = 13
Source position | H = 14
Source position | H = 5
Source position | H = 16
Source position | H = 17
ventral-dorsal (mm)
anterior-posterior (mm)
medial-lateral (mm)

Fig. 24 (Cont. II)

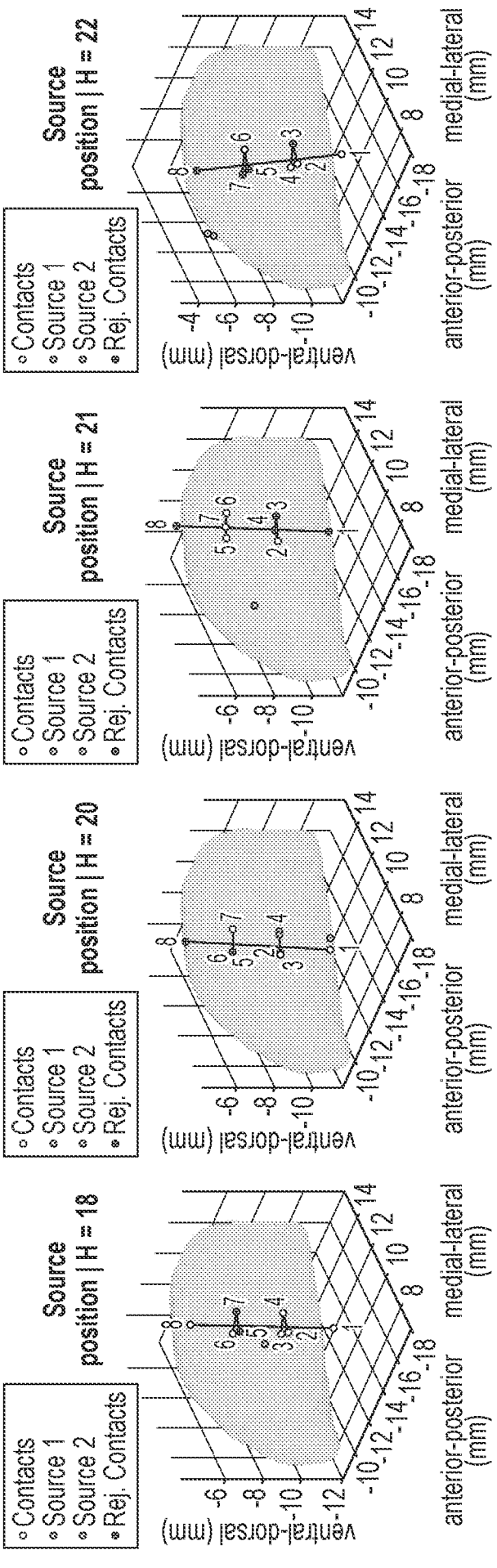

Fig. 25A

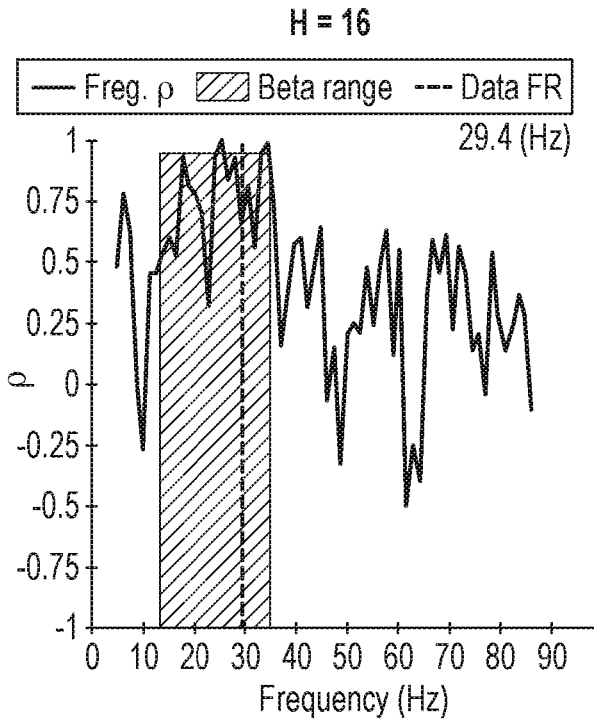


Fig. 25B

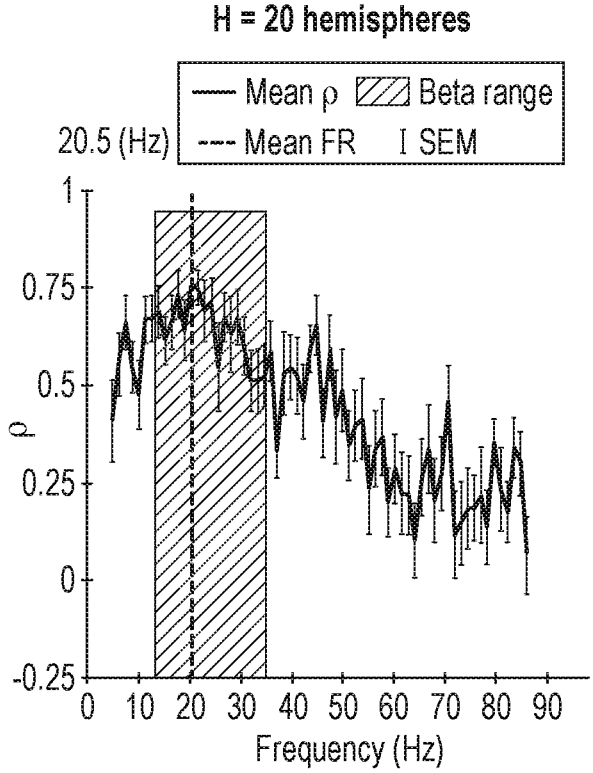


Fig. 25C

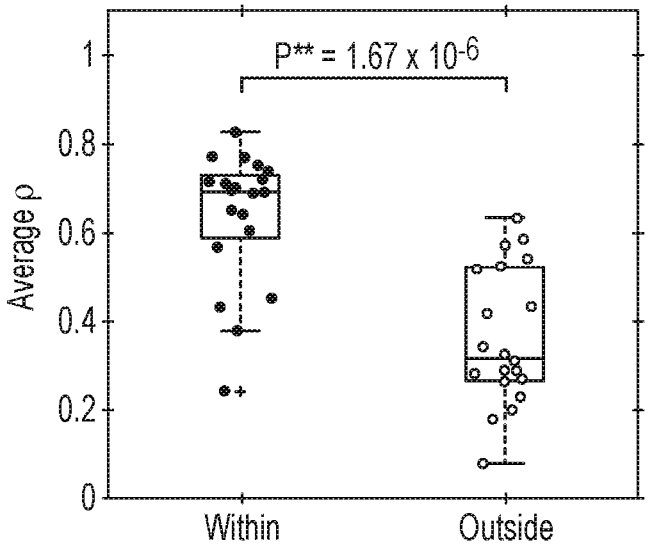

Fig. 26A

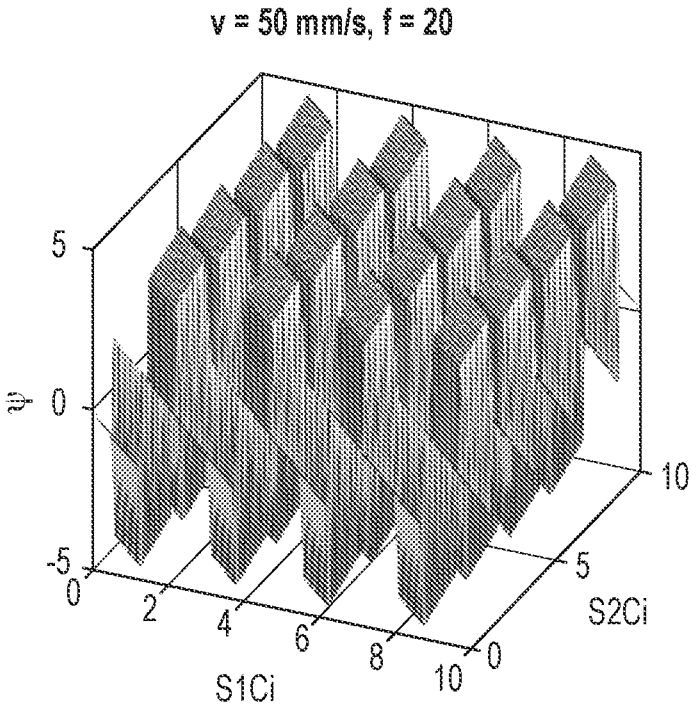


Fig. 26B

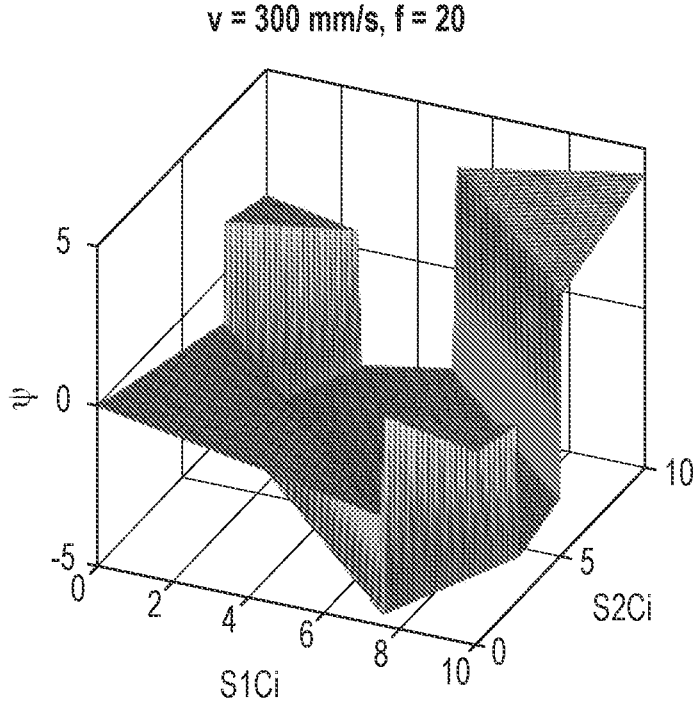

Fig. 27

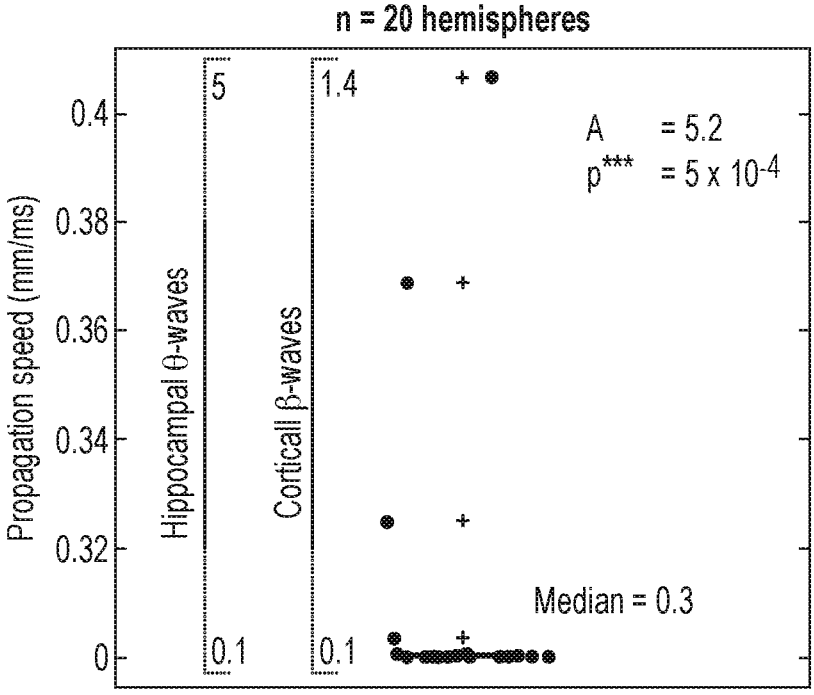
n = 20 hemispheres
Propagation speed (mm/ms)
0.4
0.38
0.36
0.34
0.32
0
Hippocampal θ-waves
5
0.1
Corticall β-waves
1.4
0.1
A = 5.2
p*** = 5 x 10-4
Median = 0.3

Fig. 28A

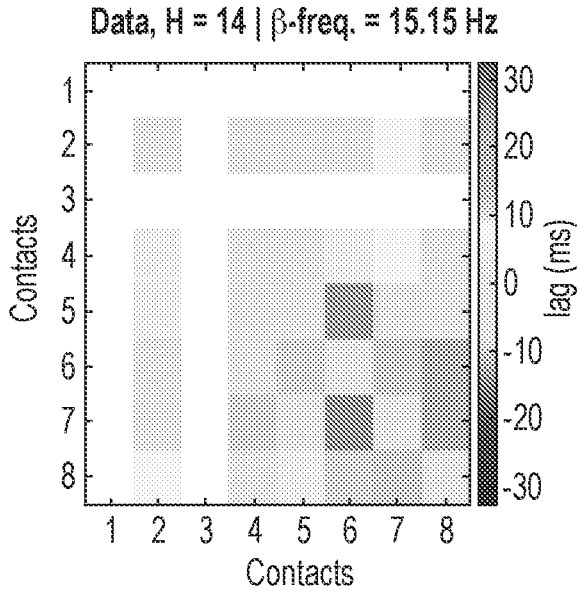


Fig. 28B

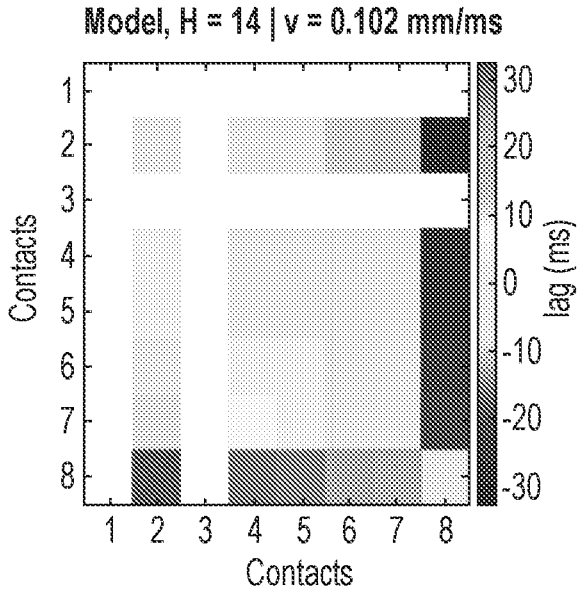


Fig. 28C

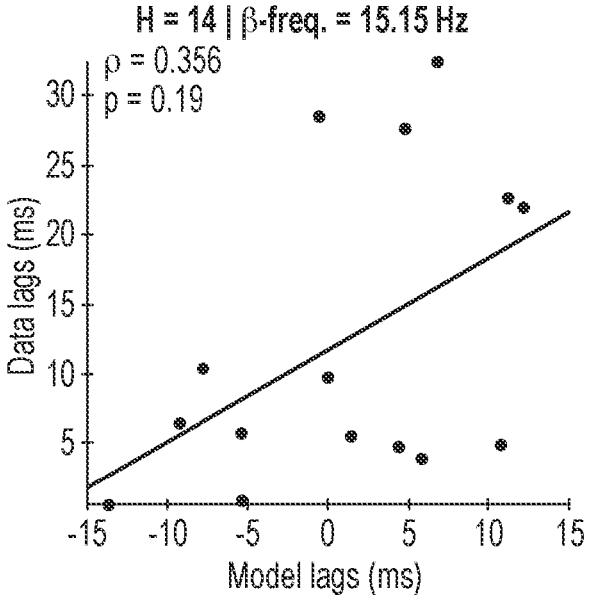


Fig. 28D

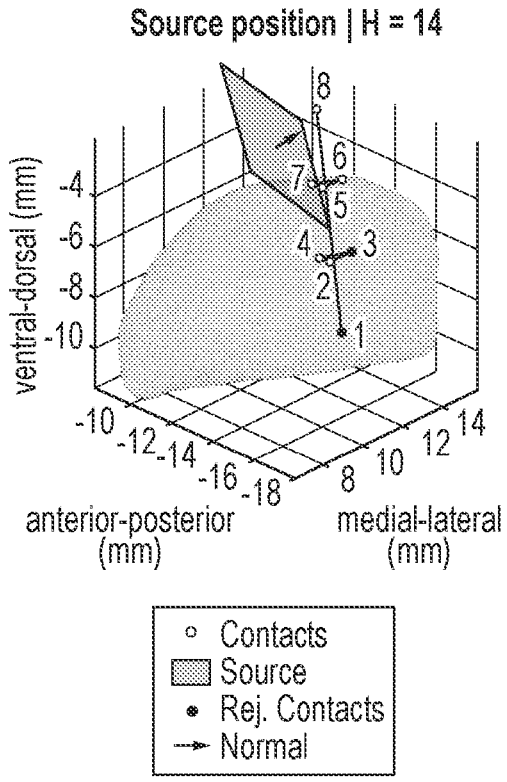

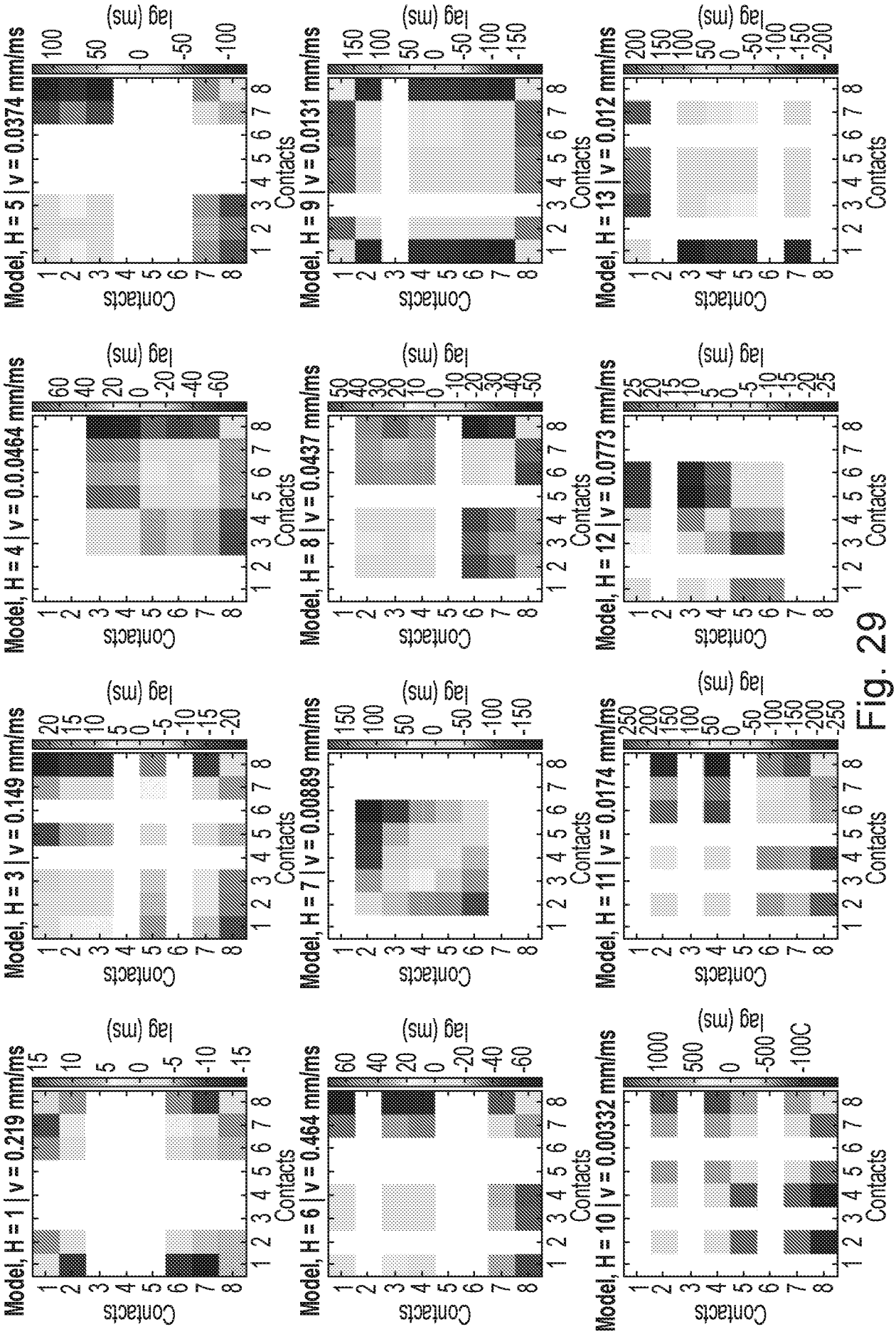
Model, H = 1 | v = 0.219 mm/ms
Model, H = 6 | v = 0.464 mm/ms
Model, H = 10 | v = 0.00332 mm/ms
Model, H = 3 | v = 0.149 mm/ms
Model, H = 7 | v = 0.00889 mm/ms
Model, H = 11 | v = 0.0174 mm/ms
Model, H = 4 | v = 0.0464 mm/ms
Model, H = 8 | v = 0.0437 mm/ms
Model, H = 12 | v = 0.0773 mm/ms
Model, H = 5 | v = 0.0374 mm/ms
Model, H = 9 | v = 0.0131 mm/ms
Model, H = 13 | v = 0.012 mm/ms
Contacts
Contacts
lag (ms)

Fig. 29

Fig. 29 (Cont.)

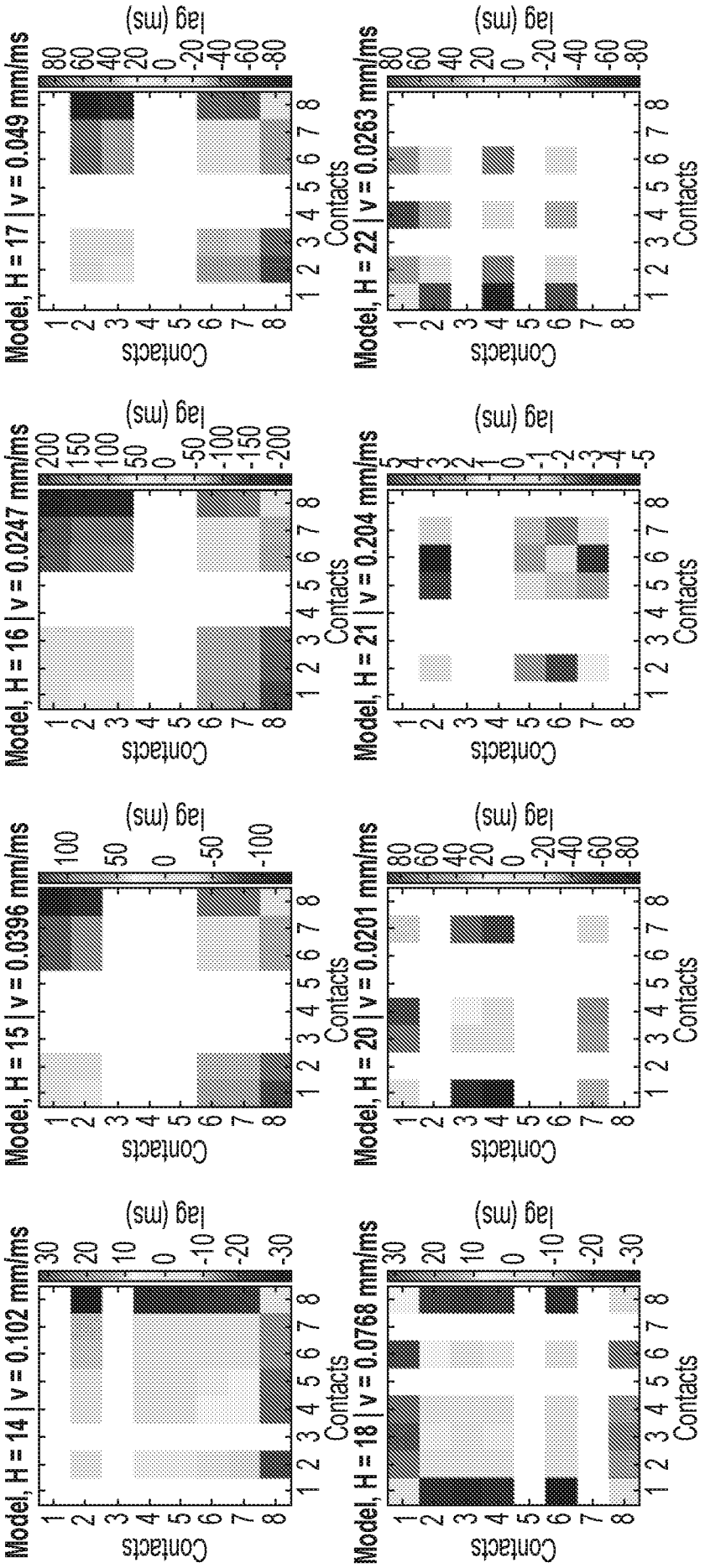
Model, H = 17 | v = 0.049 mm/ms
Model, H = 22 | v = 0.0263 mm/ms
Model, H = 16 | v = 0.0247 mm/ms
Model, H = 21 | v = 0.204 mm/ms
Model, H = 15 | v = 0.0396 mm/ms
Model, H = 20 | v = 0.0201 mm/ms
Model, H = 14 | v = 0.102 mm/ms
Model, H = 18 | v = 0.0768 mm/ms
Contacts
Lag (ms)

Fig. 30

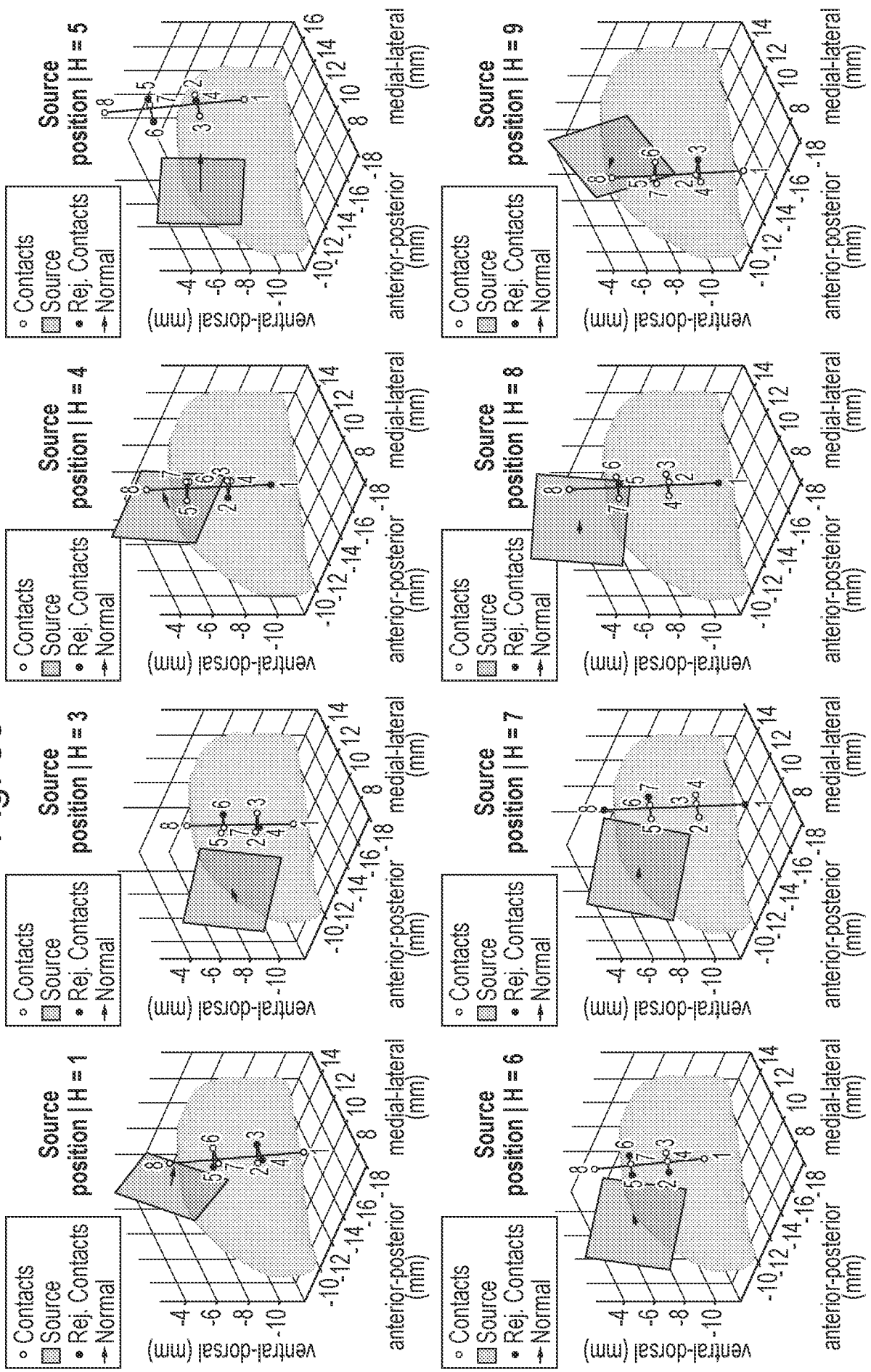
Contacts
Source
Rej. Contacts
Normal
Source position | H = 1
Source position | H = 2
Source position | H = 3
Source position | H = 4
Source position | H = 5
Source position | H = 6
Source position | H = 7
Source position | H = 8
Source position | H = 9
ventral-dorsal (mm)
anterior-posterior (mm)
medial-lateral (mm)

Fig. 30 (Cont. I)

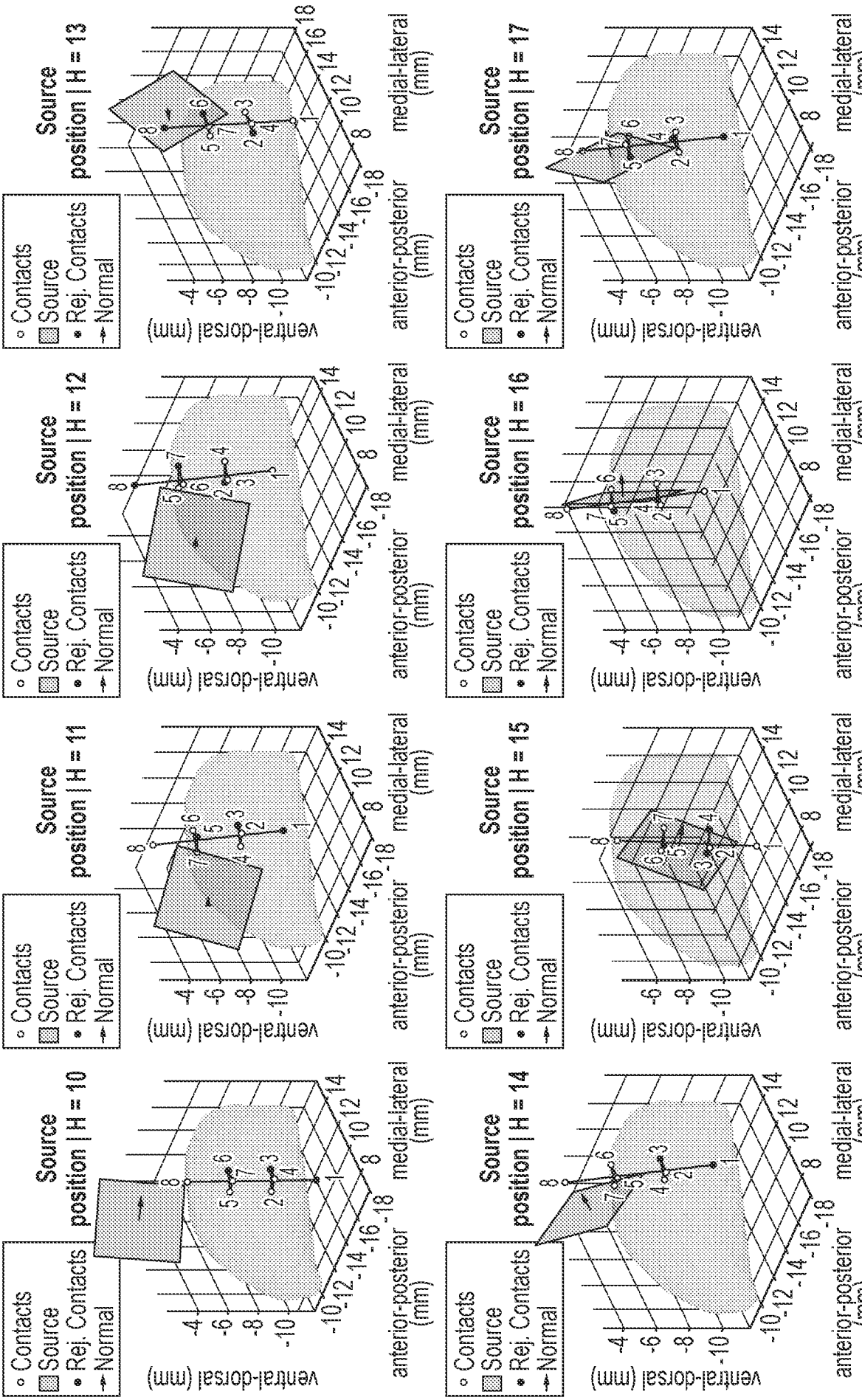
Contacts
Source
Rej. Contacts
Normal
Source position | H = 10
Source position | H = 11
Source position | H = 12
Source position | H = 13
Source position | H = 14
Source position | H = 15
Source position | H = 16
Source position | H = 17
ventral-dorsal (mm)
anterior-posterior (mm)
medial-lateral (mm)

Fig. 30 (Cont. II)

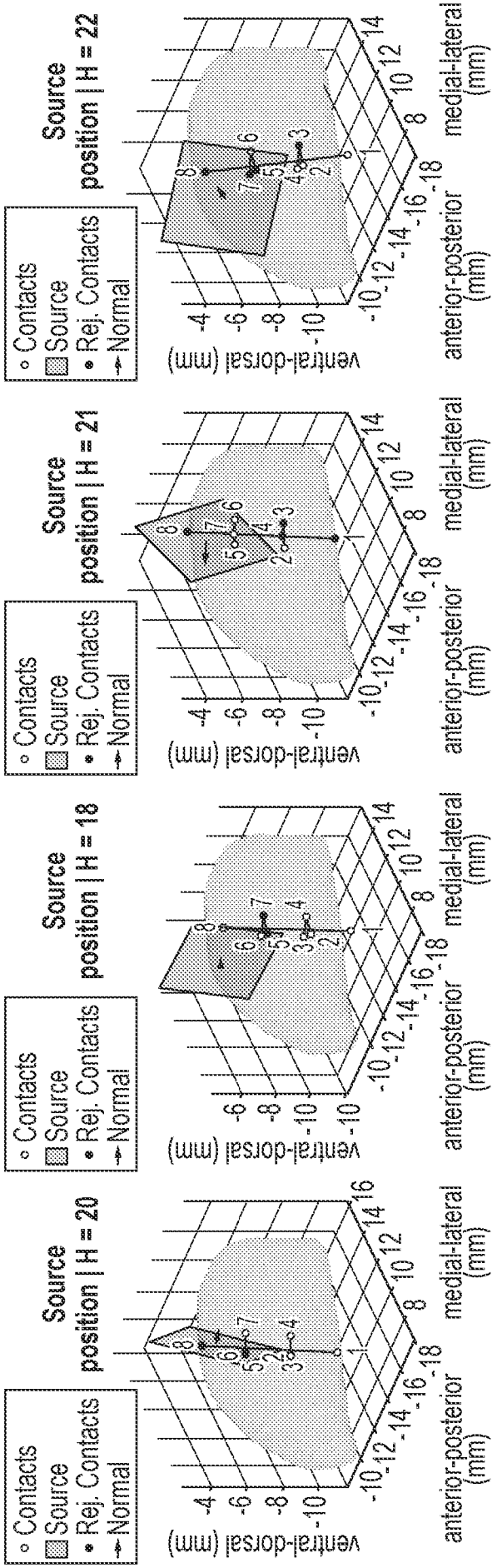

Fig. 31

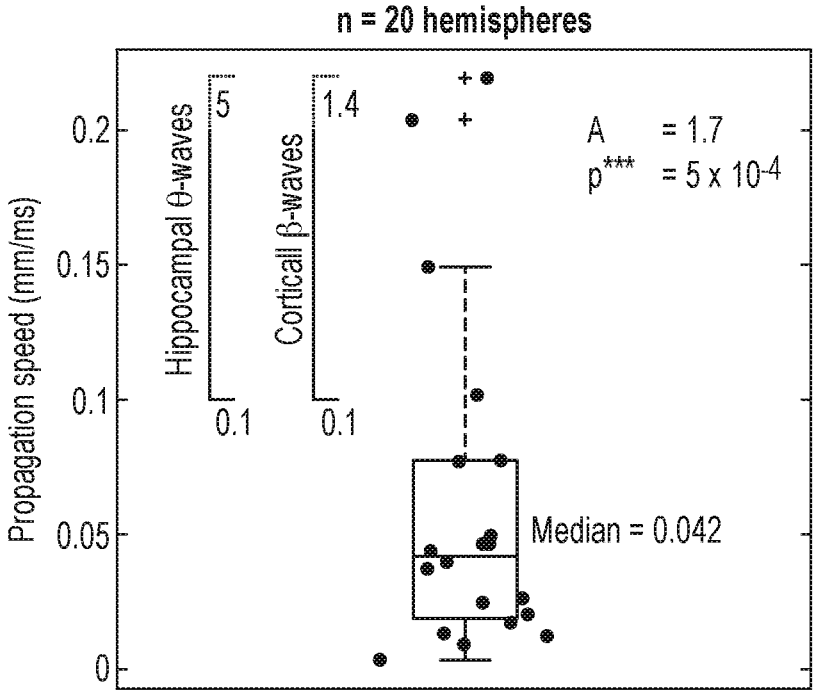
n = 20 hemispheres
Propagation speed (mm/ms)
0.2
0.15
0.1
0.05
0
Hippocampal θ-waves
5
0.1
Corticall β-waves
1.4
0.1
A = 1.7
p*** = 5 x 10-4
Median = 0.042

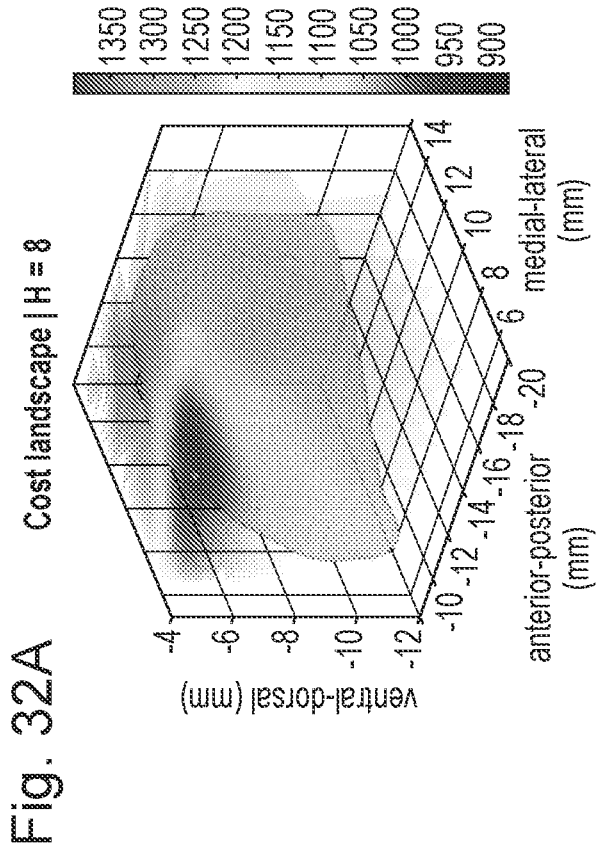


Fig. 32A

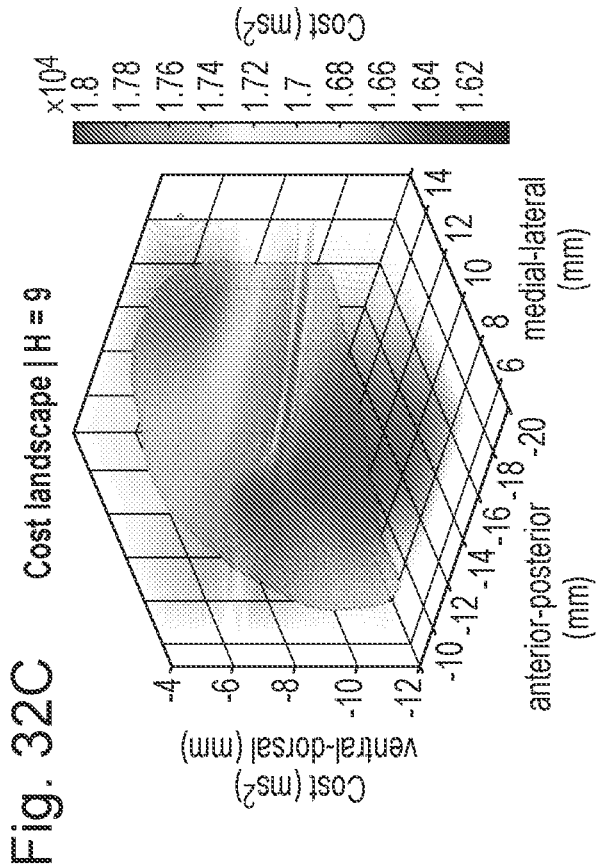


Fig. 32C

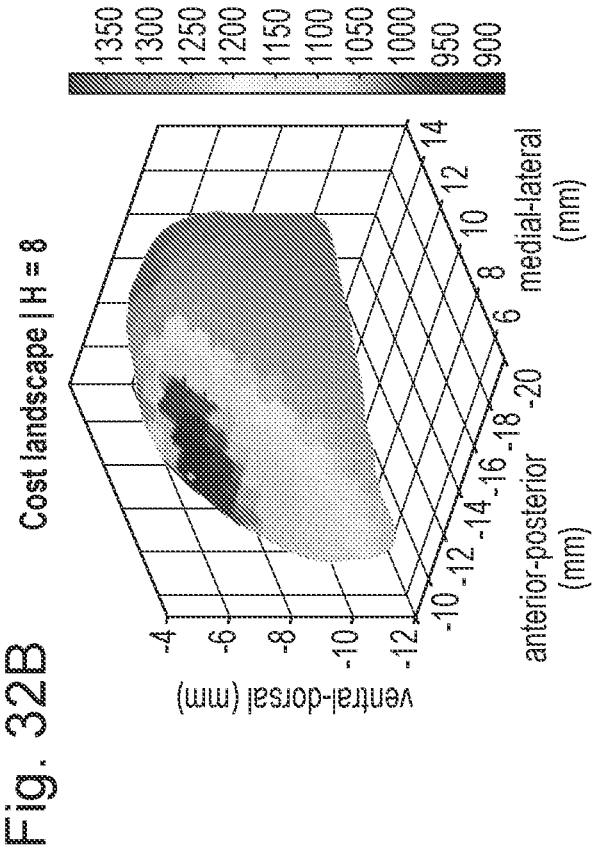


Fig. 32B

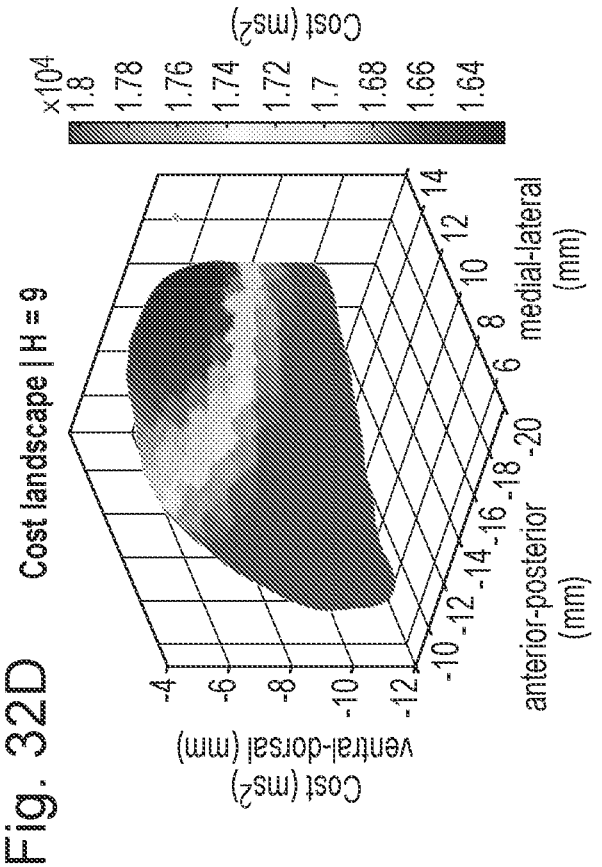


Fig. 32D

Fig. 33

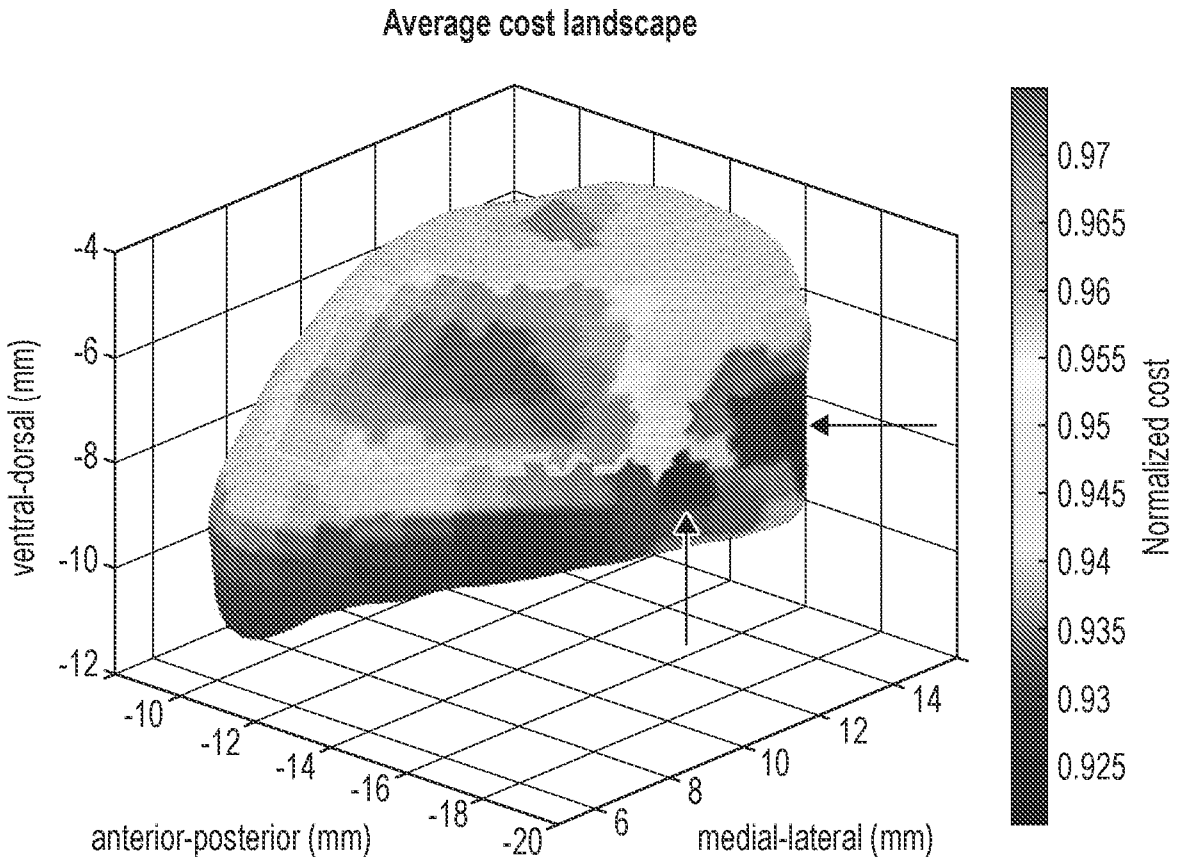
Average cost landscape
ventral-dorsal (mm)
-4
-6
-8
-10
-12
anterior-posterior (mm)
-10
-12
-14
-16
-18
-20
medial-lateral (mm)
6
8
10
12
14
Normalized cost
0.97
0.965
0.96
0.955
0.95
0.945
0.94
0.935
0.93
0.925

# INTERNATIONAL SEARCH REPORT

International application No
PCT/GB2024/050182

A. CLASSIFICATION OF SUBJECT MATTER
INV. A61B5/31 A61B5/37 A61B5/374 A61B5/00 A61N1/36
ADD.

According to International Patent Classification (IPC) or to both national classification and IPC

B. FIELDS SEARCHED

Minimum documentation searched (classification system followed by classification symbols)
A61B A61N

Documentation searched other than minimum documentation to the extent that such documents are included in the fields searched

Electronic data base consulted during the international search (name of data base and, where practicable, search terms used)
EPO-Internal, WPI Data

C. DOCUMENTS CONSIDERED TO BE RELEVANT

| Category* | Citation of document, with indication, where appropriate, of the relevant passages | Relevant to claim No. |
|---|---|---|
| X<br>A | US 2021/059549 A1 (URMAN ROY [US] ET AL)<br>4 March 2021 (2021-03-04)<br>paragraphs [0002], [0039], [0051] - [0126], [0141]; figures 1-4B,7A-7C, 8B | 1,5,7, 15-32<br>2-4,6, 8-14 |
| X | CN 114 938 946 A (UNIV ZHEJIANG)<br>26 August 2022 (2022-08-26)<br>paragraphs [0029] - [0052] | 1,28,32 |
| A | US 2006/251303 A1 (HE BIN [US] ET AL)<br>9 November 2006 (2006-11-09)<br>the whole document | 1-32 |
| A | US 2010/049482 A1 (HE BIN [US] ET AL)<br>25 February 2010 (2010-02-25)<br>the whole document | 1-32 |

☐ Further documents are listed in the continuation of Box C.

☒ See patent family annex.

* Special categories of cited documents :

"A" document defining the general state of the art which is not considered to be of particular relevance

"E" earlier application or patent but published on or after the international filing date

"L" document which may throw doubts on priority claim(s) or which is cited to establish the publication date of another citation or other special reason (as specified)

"O" document referring to an oral disclosure, use, exhibition or other means

"P" document published prior to the international filing date but later than the priority date claimed

"T" later document published after the international filing date or priority date and not in conflict with the application but cited to understand the principle or theory underlying the invention

"X" document of particular relevance;; the claimed invention cannot be considered novel or cannot be considered to involve an inventive step when the document is taken alone

"Y" document of particular relevance;; the claimed invention cannot be considered to involve an inventive step when the document is combined with one or more other such documents, such combination being obvious to a person skilled in the art

"&" document member of the same patent family

| Date of the actual completion of the international search | Date of mailing of the international search report |
|---|---|
| 2 April 2024 | 17/04/2024 |

| Name and mailing address of the ISA/ | Authorized officer |
|---|---|
| European Patent Office, P.B. 5818 Patentlaan 2<br>NL - 2280 HV Rijswijk<br>Tel. (+31-70) 340-2040,<br>Fax: (+31-70) 340-3016 | Lommel, André |

1

# INTERNATIONAL SEARCH REPORT

Information on patent family members

International application No
PCT/GB2024/050182

| Patent document cited in search report | Publication date | Patent family member(s) | Publication date |
|---|---|---|---|
| US 2021059549 A1 | 04-03-2021 | CN 112494050 A | 16-03-2021 |
| | | EP 3785609 A1 | 03-03-2021 |
| | | IL 276306 A | 01-03-2021 |
| | | JP 2021030085 A | 01-03-2021 |
| | | KR 20210027077 A | 10-03-2021 |
| | | RU 2756366 C1 | 29-09-2021 |
| | | US 2021059549 A1 | 04-03-2021 |
| CN 114938946 A | 26-08-2022 | NONE | |
| US 2006251303 A1 | 09-11-2006 | US 2006251303 A1 | 09-11-2006 |
| | | WO 2005025416 A2 | 24-03-2005 |
| US 2010049482 A1 | 25-02-2010 | AU 2007240690 A1 | 01-11-2007 |
| | | CA 2649906 A1 | 01-11-2007 |
| | | EP 2011032 A2 | 07-01-2009 |
| | | JP 2009534103 A | 24-09-2009 |
| | | US 2010049482 A1 | 25-02-2010 |
| | | WO 2007124040 A2 | 01-11-2007 |